ENHANCED PERFORMANCE AND FUNCTIONALITY OF TITANIUM DIOXIDE PAPERMAKING PIGMENTS WITH CONTROLLED MORPHOLOGY AND SURFACE COATING

A Dissertation
Presented to
The Academic Faculty

by

Kimberly L. Nelson

In Partial Fulfillment
of the Requirements for the Degree
Doctor of Philosophy in the
School of Chemical and Biomolecular Engineering

Georgia Institute of Technology
August 2007

ENHANCED PERFORMANCE AND FUNCTIONALITY OF TITANIUM DIOXIDE PAPERMAKING PIGMENTS WITH CONTROLLED MORPHOLOGY AND SURFACE COATING

Approved by:

Dr. Yulin Deng, Advisor
School of Chemical and
Biomolecular Engineering
Georgia Institute of Technology

Dr. Arthur Ragauskas
School of Chemistry and Biochemistry
Georgia Institute of Technology

Dr. Jeffery Hsieh
School of Chemical and
Biomolecular Engineering
Georgia Institute of Technology

Dr. Preet Singh
School of Materials Science and
Engineering
Georgia Institute of Technology

Dr. Jeff Empie
School of Chemical and
Biomolecular Engineering
Georgia Institute of Technology

Date Approved: June 28, 2007

A jug fills drop by drop.

-Siddhartha Buddha

Dedicated to John A. Nelson Sr. and Holly Cater.

ACKNOWLEDGEMENTS

I wish to express my gratitude to my advisor, Dr. Yulin Deng, for training me as a scientist, for fostering creativity and independence, and for his friendliness and approachability. I would like to thank my dissertation committee particularly for their scrutiny of my proposal, which stretched me to produce a more superior, scientifically relevant body of work. Particularly, I would like to thank Dr. Art Ragauskas and Dr. Preet Singh for allowing me to use their equipment and borrow supplies from time to time. I would also like to thank Yolande Berta in the Georgia Tech Electron Microscopy Center for training and advisement and the Georgia Tech X-ray Analysis Group for training and use of their facility. I am indebted to our group's research scientists, Dr. Qunhui Sun, Dr. Yulin Zhao, and Dr. Zegui Yan, who gave much assistance and training throughout my experiments. I would also like to thank the other members of our group, Zhaohui Tong, Brett Brotherson, Ying Wang, Zhengzhi Zhou, and Se-Young Yoon for being amazingly friendly and helpful. I would like to thank IPST for funding and for providing a supportive environment and good facilities. I am grateful for Major White who encouraged me with a simple phrase many years ago that has, unbeknownst to him, become my mantra: "No doubt, throw it out." I would like to thank all my former teachers and mentors who taught me to love scholarship and creativity including Dr. Lachelle Foley, Dr. Myrtle Lewin, Margaret Tenney, Dana Mobley, and Meyriel Edge. I would also like to thank Dr. Micky O'Leary for her support and encouragement. Finally, I would like to thank my family for providing me with love, support, and a wonderful education.

TABLE OF CONTENTS

LIST OF TABLES

LIST OF FIGURES

LIST OF EQUATIONS

NOMENCLATURE

AFM	=	Atomic Force Microscopy
C_{sca}	=	Scattering cross section
$CaCO_3$	=	Calcium carbonate
GCC	=	Ground calcium carbonate
CPAM	=	Cationic polyacrylamide
cpvc	=	Critical pigment volume concentration
Fg	=	Flocculation gradient
g	=	Asymmetry parameter
GSD	=	Geometric size distribution
K	=	Kubelka-Munk absorption coefficient
KM	=	Kubelka-Munk
LBL	=	Layer-by-layer
MWCO	=	Molecular weight cut-off
n	=	Refractive index
n_o	=	Ordinary refractive index
n_e	=	Extraordinary refractive index
NMMO	=	N-methylmorpholine-N-oxide
PAA	=	Poly(acrylic acid, sodium salt)
PCC	=	Precipitated calcium carbonate
PDADMAC	=	Poly(diallyldimethylammonium chloride)
PEG	=	Polyethylene glycol

pvc	=	Pigment volume concentration
PVP	=	Poly(vinylpyrrolidone)
Q_{sca}	=	Light scattering efficiency
R	=	Intensity of incident light reflected from an interface
R_0	=	Reflectance of single sheet with black backing
R_∞	=	Reflectance of thick pad of paper
$R_{0.89}$	=	Reflectance of single sheet with white backing having R=89%
R_g	=	Radius of gyration
RC	=	Regenerated cellulose
RCF	=	Relative centrifugal force
S	=	Kubelka-Munk scattering coefficient
SCPM	=	Light scattering coefficient per micron
SEM	=	Scanning Electron Microscopy
TALH	=	Titanium(IV) bis(ammonium lactate) dihydroxide
TBT	=	Titanium(IV) butoxide
TEM	=	Transmission Electron Microscopy
TEOS	=	Tetraethyl orthosilicate
$TiCl_4$	=	Titanium tetrachloride
TiO_2	=	Titanium dioxide
XRD	=	X-ray diffraction spectroscopy
δ	=	Shell thickness for core-shell particles
λ	=	Wavelength of light
σ	=	Light scattering parameter

SUMMARY

Pigments are used in papermaking to provide desired functional end-use properties such as opacity, brightness, color, gloss, smoothness, porosity, bulk, printability and/or to reduce paper cost. Of all papermaking pigments, titanium dioxide has the highest brightness, opacifying power, and cost. Several papermaking trends necessitate more use of TiO_2 including reduction in basis weight and the increasing use of cheap, discolored fibers. Also, because TiO_2 is used in a large variety of products, its global demand growth is increasing rapidly along with its exceptionally high price. The introduction of novel, even more efficient light scattering TiO_2-based pigments is necessary to help manufactures limit costs while maintaining the required optical properties of their product. One approach to increasing the efficiency of TiO_2 is to create unique pigment morphologies designed to scatter light more effectively than conventional TiO_2 pigments. The achievement of this goal requires quantitatively identifying and controlling the factors which impact the light-scattering efficiency of TiO_2. However, little is known about the effects of TiO_2 particle morphology on light scattering efficiency. A well known disadvantage of adding fillers like TiO_2 to paper is the reduction of interfiber bonding, and therefore paper strength. From a papermaking perspective, it is necessary to develop novel TiO_2 pigments with enhanced opacifying power and bondability. This thesis shows that novel, tailored titanium dioxide pigments with controllable nanoscale morphological features can significantly enhance the optical and strength properties of paper.

The opacifying power of synthesized polycrystalline TiO_2 particles in a cellulose matrix was found experimentally to be superior to that of a commercial rutile pigment, depending on the crystal structure of the synthesized particles. Polycrystalline anatase pigments had less opacifying power than commercial rutile, while polycrystalline pigments containing a one-to-one mixture of anatase and rutile had similar opacifying power as the commercial pigment. High aspect ratio polycrystalline rutile pigments composed of a linear linkage of several individual rutile crystals gave 6% more opacity than the commercial rutile pigment. Theoretical light scattering calculations using the T-Matrix Method showed the light scattering efficiency of linearly arranged polycrystalline rutile particles to depend on number and size of crystals composing the particle and confirmed the higher efficiency of the synthesized polycrystalline rutile pigments over commercial rutile. It is believed that the greater than expected light scattering efficiency of the biphasic pigment results from light scattering at the grain boundaries between crystals of different phase with different refractive indices.

The opacifying power of hollow polycrystalline rutile particles was found experimentally to be superior to that of a commercial rutile pigment in a highly pressed bleached fiber matrix, depending on cavity size, while the opacifying power of silica-rutile titania core-shell particles was found comparable to commercial rutile at constant *titania* loading. The light scattering efficiency of titania core-shell particles was also shown to be dependant on the light scattering efficiency of the core material. The light scattering efficiency of the polycrystalline silica cores was found to depend on crystal structure.

Titania core-shell and hollow nanoparticles with different aspect ratios were synthesized using layer-by-layer assembly and sol-gel nanocoating methods with cellulose nanowhiskers as the template. During coating layer growth, the shape of the nanoparticles did not maintain the shape of the high aspect ratio template, as previously assumed. The shape of the coated particles is a function of the coating thickness. It is suggested that the overall particle shape and aspect ratio of the nanoparticles are tunable by choosing an appropriate template and coating thickness in layer-by-layer or sol-gel templating synthesis.

Inorganic-cellulose core-shell and hollow cellulose nanoparticles were prepared by self-encapsulation with regenerated cellulose via precipitation of cellulose in a polyacrylic acid hydrogel layer surrounding inorganic particle templates in 4-Methylmorpholine N-oxide (NMMO) monohydrate solution. It was found that the hydrogel layer surrounding the inorganic particle surface played an important role in core-shell structure formation. The effects of addition rate of water (a non-solvent of cellulose) on the nanostructure, morphology and crystallinity of regenerated cellulose from NMMO solution under agitation were studied. The mechanism of different crystal phase formations via controlled addition rate of non-solvent was discussed.

The discrete encapsulation of inorganic pigments with a thin, uniform cellulose shell was found to increase the bondability improvement between the particles and a polysaccharide substrate. The crystallinity of several carbohydrate polymers was shown to significantly affect the bondability of encapsulated core-shell particles. The impact of

the coating layer on light scattering efficiency was also studied using theoretical Mie scattering calculations.

CHAPTER 1

INTRODUCTION

Pigments are used in papermaking both as fillers within the sheet and as the major component of paper coatings to provide desired functional end-use properties such as opacity, brightness, color, gloss, smoothness, porosity, bulk, printability and/or to reduce paper cost. Approximately $2.50/ton can be saved for each 1% increase in filler content as a result of reduced raw material and energy costs. However, principle disadvantages of increased filler loadings include reduced paper strength and the requirement of increasing amounts of expensive dry strength aids. Inorganic fillers reduce paper strength by interfering with interfiber bonding, since they have no ability to form similar strong bonds with the fibers. Despite these disadvantages, several global trends are requiring the papermaker to increase filler levels. One trend, based on rising consumer expectations, is the shift in focus of papermaking from productivity and cost reduction, to production of differentiated, functional products. Other changes include the continual shift to lighter basis weights as raw material prices and postage rates increase and the increasing use of cheap, dark-colored fibers from recycled, mechanical, and high kappa number pulps and the use of low density, high brightness, porous fillers for improved print quality.

These challenges require increasing levels of performance and functionality from pigments. Fundamental next generation pigment desirables include enhanced opacifying power, bulking capability, and bondability. Sophisticated techniques borrowed from the fields of nanotechnology and interfacial science offer countless opportunities for the

synthesis of novel, high performance pigments whose functionality and performance are defined by tailored morphology, optical properties, and surface chemistry. As exemplified by the 2001 article "Paper Innovation Ramps Up with Nano-Chemistry", many anticipate nanotechnology developments in the areas of fiber and composite science and inorganic synthesis to help revolutionize papermaking (1). Other examples of this anticipation include development of the *Nanotechnology for the Forest Products Industry Vision and Technology Roadmap* (2) and TAPPI's upcoming Second Annual *International Conference on Nanotechnology for the Forest Products Industry*.

Despite the industry's enthusiasm over many years for "bottom-up" synthesis approaches to enhance papermaking, few solutions have been presented in the literature to date. This thesis focuses on two important issues in filler development: a) the effects of crystal nanostructure and crystal aggregation on polycrystalline filler performance and b) filler bondability improvement by encapsulation with cellulose polymer. Results indicate that synthesis of novel, tailored inorganic and inorganic-organic core-shell pigments with controllable nanoscale morphological features offer the potential to significantly enhance the optical and strength properties of paper. Because of its exceptional opacifying performance and high cost, a majority of this thesis is focused on titanium dioxide. Chapter 2 presents the properties and performance of traditional papermaking pigments and reviews the recently developing field of novel inorganic particles synthesis. The fundamentals underlying the opacifying power of TiO_2 are reviewed along with light scattering theory. The developing debate in the literature regarding the influence of TiO_2 pigment morphology on light scattering is also discussed. The impact of inorganic

pigments on paper strength is reviewed along with recent attempts to overcome this disadvantage via particle modification. This thesis also discussed the effect of encapsulating natural polymer structures on filler-fiber bonding strength. Novel regenerated cellulose coated fillers are presented and the scientific and technologically relevant aspects of the dissolution and regeneration of cellulose by the NMMO (4-Methylmorpholine N-oxide) monohydrate solvent system is discussed. As such, a thorough presentation of the relevant literature is provided as background for the topics and issues addressed in the subsequent chapters.

Chapter 3 provides an analysis of the problem and outlines the objectives of this research. The thesis is organized to first show that synthesis of unique and controllable TiO_2 particle structures can offer significant improvement over the opacifying performance of conventional TiO_2 pigments. Chapter 4 presents experimental and theoretical solutions to the problem of light scattering by small, well dispersed polycrystalline aggregates of TiO_2 in a cellulose medium. A sensitive and reproducible laboratory experiment was designed to study the effects of phase composition, crystallite size, and crystallite arrangement on the opacifying power of synthesized and commercial TiO_2 pigments. The synthesized pigments were characterized using SEM, TEM, XRD, and light scattering. Using the same laboratory method and particle characterization techniques, Chapter 5 presents the light scattering properties of core-shell and hollow polycrystalline TiO_2 pigments. Chapter 6 shows how the shape and cavity size of hollow, polycrystalline TiO_2 pigments can be controlled to produce novel pigments with potentially dramatic light scattering capabilities. The remaining chapters of this thesis are devoted to synthesizing

discrete core-shell inorganic pigments with a well defined cellulose coating to improve bondability with a cellulose fiber matrix. Chapter 7 presents the synthesis of inorganic-cellulose core-shell and hollow cellulose nanoparticles by self-encapsulation with regenerated cellulose in NMMO monohydrate solution via cellulose precipitation in a polyacrylic acid hydrogel layer surrounding the inorganic particle templates. Chapter 8 shows the bondability improvement offered by these cellulose encapsulated and hollow nanoparticles with a wood fiber substrate.

CHAPTER 2

LITERATURE REVIEW

2.1 Conventional Papermaking Pigments

2.1.1 Pigment Uses

Pigments are used in papermaking both as fillers within the sheet and as the major component of paper coatings to provide desired functional end-use properties such as opacity, brightness, color, gloss, smoothness, porosity, bulk, printability and/or to reduce paper cost. Approximately $2.50/ton can be saved for each 1% increase in filler content as a result of reduced raw material and energy costs. Mineral fillers are much less expensive than wood fibers and increased filler allows for improved draining and drying, leading to less energy consumption in the driers (3). Additionally, increasing the level of filler in paper offers other advantages like increasing paper production capacity without the addition of extra pulping capacity and allowing the use of lower quality, discolored pulp such as mechanical pulp, recycled pulp, and high kappa number pulp (4). When bulking filler pigments are added to the wet end, basis weight is maintained while reducing the fiber content of the furnish. For some grades this ability to maintain bulk is the principle reason for adding filler and is termed fiber extension. The value of fiber extension is related to the availability and cost of fiber at the mill site. With projected fiber price increases and regional fiber shortages, it is anticipated that significantly more filler pigments will be used in the future, citing fiber extension as the main reason. When fiber extension is the primary reason for using filler, the most economical and sometimes

least optically efficient fillers are used. However, the most frequently cited reason for using fillers is the optical improvements they can offer a sheet. At very low basis weights, a filler's opacifying performance is maximized, at high basis weights it is minimized (5). The principle reasons for applying a pigment coating to paper and paperboard are to improve printability and appearance. In its simplest form the coating consists of a pigment plus an adhesive to bind the pigment particles both to one another and to the base paper. Pigments are the main constituent of coatings with binders and various additives normally comprising less than 20 % by weight. Properly chosen and formulated, the pigments provide a coating with surface smoothness, brightness, opacity, and a balance of ink holdout and ink receptivity upon which to print (6). Figure 1 shows that increasing the mineral content of paper and paperboard increases its value and selling price (7).

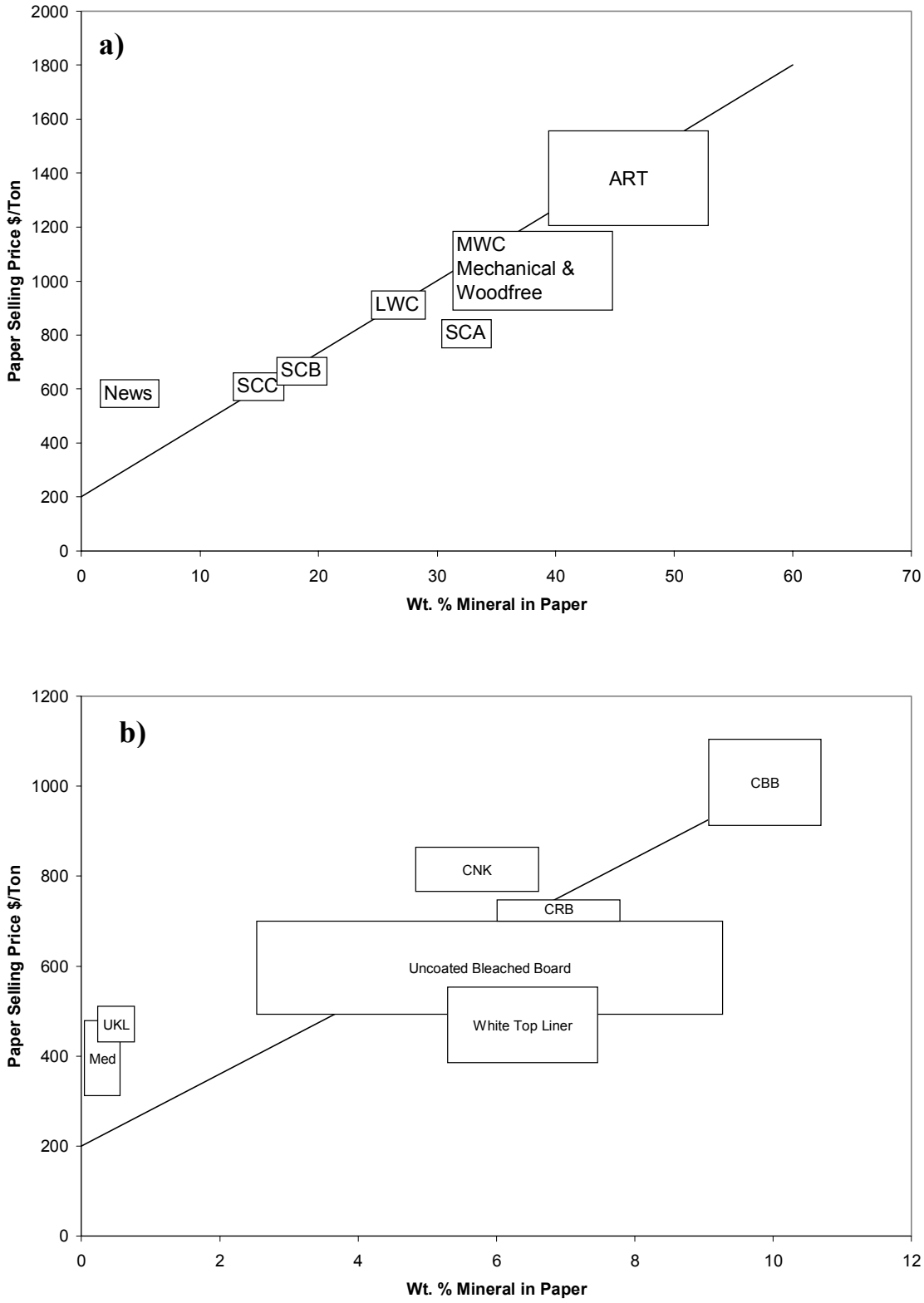

Figure 1: Increase in (a) paper and (b) paperboard value with increasing pigment content (adapted from Bakshi and Walrond, 2006).

2.1.2 Common Pigments

There are two classes of calcium carbonate used in paper: natural ground calcium carbonate (GCC) and chemically synthesized precipitated calcium carbonate (PCC). Kaolin clay is a naturally occurring, white, hydrated alumina-silicate mineral that has little value in raw form and must be processed extensively to become a value added product. Calcined clay, in particular gives high brightness by removing impurities and improved light scattering because of its agglomerated "popcorn" structure (8). TiO_2 is a very white, bright pigment with the greatest specific opacifying power and highest cost. As shown in Figure 2, calcium carbonates account for the largest global demand in the papermaking pigment market (64%) followed by kaolin clay (29%) and the more specialty pigment TiO2 (1%) (7).

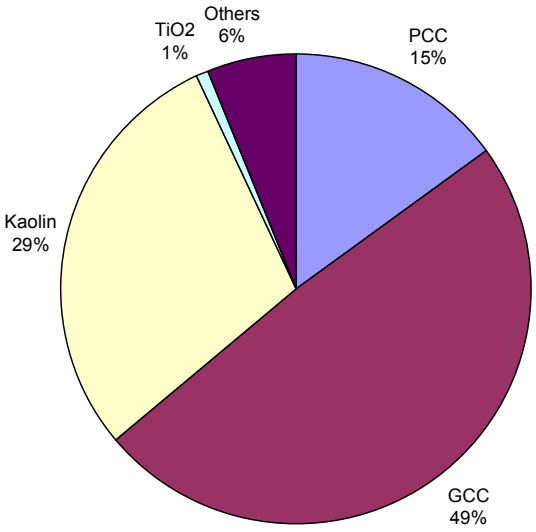

Figure 2: Global papermaking pigment demand (Bakshi and Walrond, 2006).

The SEM images in Figure 3 show the morphologies of clay, GCC, and TiO_2.

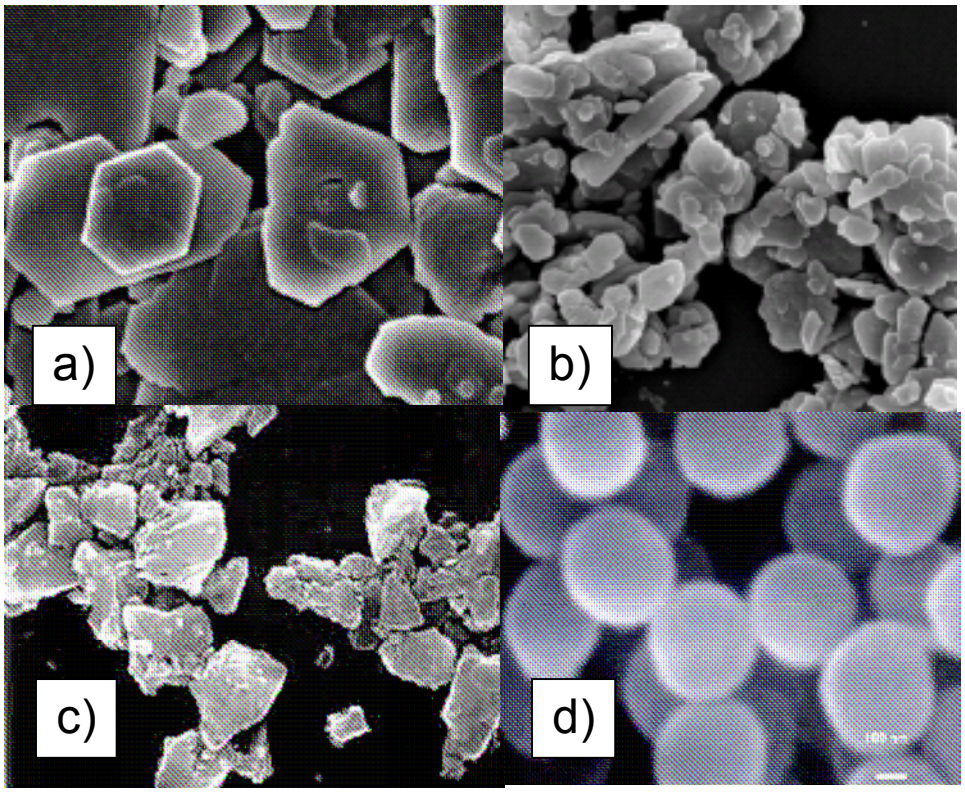

Figure 3: SEM images of commercial (a) kaolin clay, (b) calcined clay, (c) GCC, and (d) TiO_2.

PCC is offered in a variety of particle morphologies including cubic, acicular, and schalenohedral as shown in Figure 3. These morphologies are chosen to impart specific end-use properties such as smoothness, bulk, and enhanced opacity.

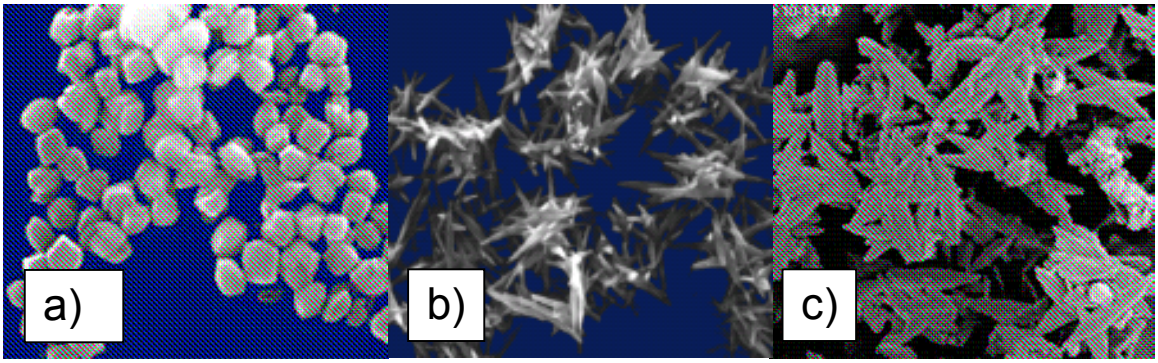

Figure 4: SEM images of (a) cubic, (b) acicular, and (c) scalenohedral PCC.

2.1.3 Pigment Properties

The most important characteristics of mineral pigments from a papermaker's perspective are cost, color, brightness, and opacifying power (or ability to impart opacity) as suggested by the size of their scattering coefficient. Typically, the highest optically performing pigments have the smallest particle size, and highest refractive index, brightness, and scattering coefficient. Table 1 lists these values for the most common mineral pigments used in papermaking (9).

Table 1: Pigment parameters that influence opacifying power (Scott, 1996).

	Avg. Size, µm	Refractive Index	Scattering Coeff., cm^2/g	Brightness, %
Clay	0.2-2.0	1.57	1100-1200	78-90
Calcined Clay	0.7-1.5	1.60	2600-3000	90-95
GCC	0.7-3.0	1.59	1400-1700	80-95
PCC	0.3-3.0	1.59	2200-2700	96-100
TiO_2	0.2-0.4	2.55 (anatase)	4500-6000	98-100
		2.76 (rutile)		

2.2 Innovative Papermaking Pigments

2.2.1 New Inorganic Pigments

A recently developing field of practical and scientific interest is the synthesis of novel inorganic pigment structures often using sophisticated techniques borrowed from the fields of nanotechnology and interfacial science. While such particles have wide applicability across many fields, for papermaking they are designed to offer enhanced optical and physical performance. Ideally these particles should be much less expensive than TiO_2 but have similar brightness and opacity. In addition, they should provide high

bulk and have minimal impact on paper strength. Most of the novel fillers have a highly porous or hollow structure, designed to minimize material usage and enhance bulk and light scattering. These fillers are largely based on traditional inorganic papermaking pigments like clay, calcium carbonate, and TiO_2. However, Mathur has synthesized a promising, economically viable, high performance filler composed of crystalline calcium silicate hydrate (10). The particles are highly porous haystack-like particles containing complex multi-phase crystalline fibers. While the particles are fairly large (d = 0.1-0.2 μm, l = 1–4 μm) and irregular in shape, they scatter light better than PCC, GCC, clay, and calcined clay. The particles offer higher brightness and opacity than schalenohedral PCC, low bulk density, good chemical stability in aqueous solution, and high ink adsorptive capability. Several research groups have synthesized hollow calcium carbonate particles ranging in diameter from 0.5 to 300 μm (11-19). Enome and Tsujino prepared spherical hollow particles of calcium carbonate between 0.5 and 2 μm in diameter using interfacial reaction in a water-in-oil emulsion (14). The shell is composed of aggregated crystals with diameters between 50 and 300 μm in mixed crystal forms of calcite and vaterite. These particles give higher opacity than conventional ground calcium carbonate, but lower than scalenohedral particles. Researchers have also synthesized hollow silica (20, 21) and hollow clay particles (21, 22). Finally, as a result of TiO_2's very high cost as a pigment and large number of industrial, technological, and commercial applications, there has been much interest in the design and fabrication of spherical core-shell (23, 24) and hollow (25-44) titania materials in recent years. Typical methods include the layer-by-layer coating of nanosized templates (25, 26) and the sol-gel coating of templates (28, 32, 34, 36, 39-41). In addition to hollow titania spheres,

titania micro (45-48) and nanotubes (49-54) have been prepared. These unique structures have been studied with great interest because they provide higher specific surface area than titania spheres. Synthesis of titania tubes typically involves coating high aspect ratio templates using sol-gel chemistry (46-48, 51) or layer-by-layer self-assembly (55-57). Previously utilized templates include the tobacco mosaic virus (57), nickel nanorods (56), and carbon nanotubes (55). Nanosized polycrystalline titania tubes may make suitable and superior papermaking fillers. Their elongated fiber shape is expected to particularly enhance TiO_2 retention in the paper sheet, a particular problem for conventional TiO_2.

2.2.2 Sol-Gel Synthesis

The most widely used method to prepare hollow nanostructured titanium dioxide particles is sol-gel synthesis. In general, the sol-gel process involves inorganic precursors (a metal salt or organometallic molecule) that undergo various reactions resulting in the formation of a three-dimensional molecular network. A common example is the hydrolysis and condensation reaction of metal alkoxides to form larger metal oxide molecules (26):

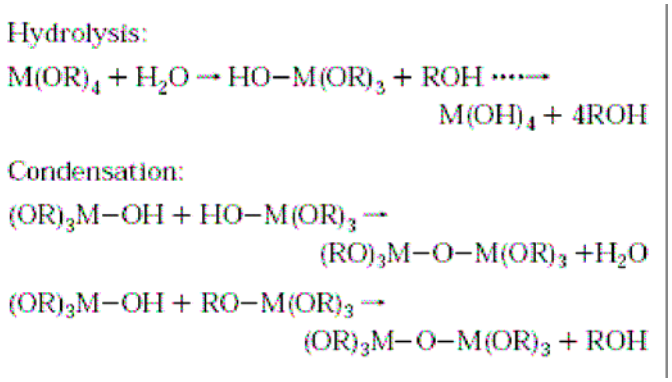

Figure 5: Sol-gel reaction of metal alkoxides (Collins et al. 2003).

where M represents the metal and R the alkyl group. Titanium alkoxide precursors rapidly undergo hydrolysis and condensation in the presence of water. Thus, coating in nonaqueous solvents is required. Hollow submicrometer sized titania spheres have been formed by coating colloidal templates through the hydrolysis and condensation of titanium alkoxides on the particle surface to produce amorphous titania shells followed by calcination at high temperature to remove the core and to crystallize the titania. A principle disadvantage of the sol-gel method is the high reactivity of the titania precursors. This reactivity makes it difficult to control precipitation and can lead to particle aggregation and formation of separate titania particles (32). Other disadvantages of the sol-gel process include the formation of irregular coatings, little control over coating thickness, and the need for precise control over reaction conditions to maximize coating uniformity (e.g. concentration of reagents, pH, temperature, mixing conditions) (58).

2.2.3 Layer-by-Layer Self-Assembly Synthesis

The Layer-by-Layer (LBL) Self-Assembly method was developed to overcome the disadvantages of the sol-gel method mentioned above for coating metal oxides onto templates. The Layer-by-Layer method for obtaining hollow metal oxide submicrometer particles is based on the electrostatic association between alternately deposited, oppositely charged species on a colloidal sacrificial template followed by removal of the template upon heating. As illustrated in Figure 6, LBL can be used to obtain core-shell and hollow titania by the sequential adsorption of a cationic polymer and the negatively charged titanium dioxide precursor titanium (IV) bis(ammonium lactate) dihydroxide

(TALH) (25, 58, 59). Crystalline core-shell particles are obtained by refluxing the coated particles in water, while hollow particles are obtained by calcination.

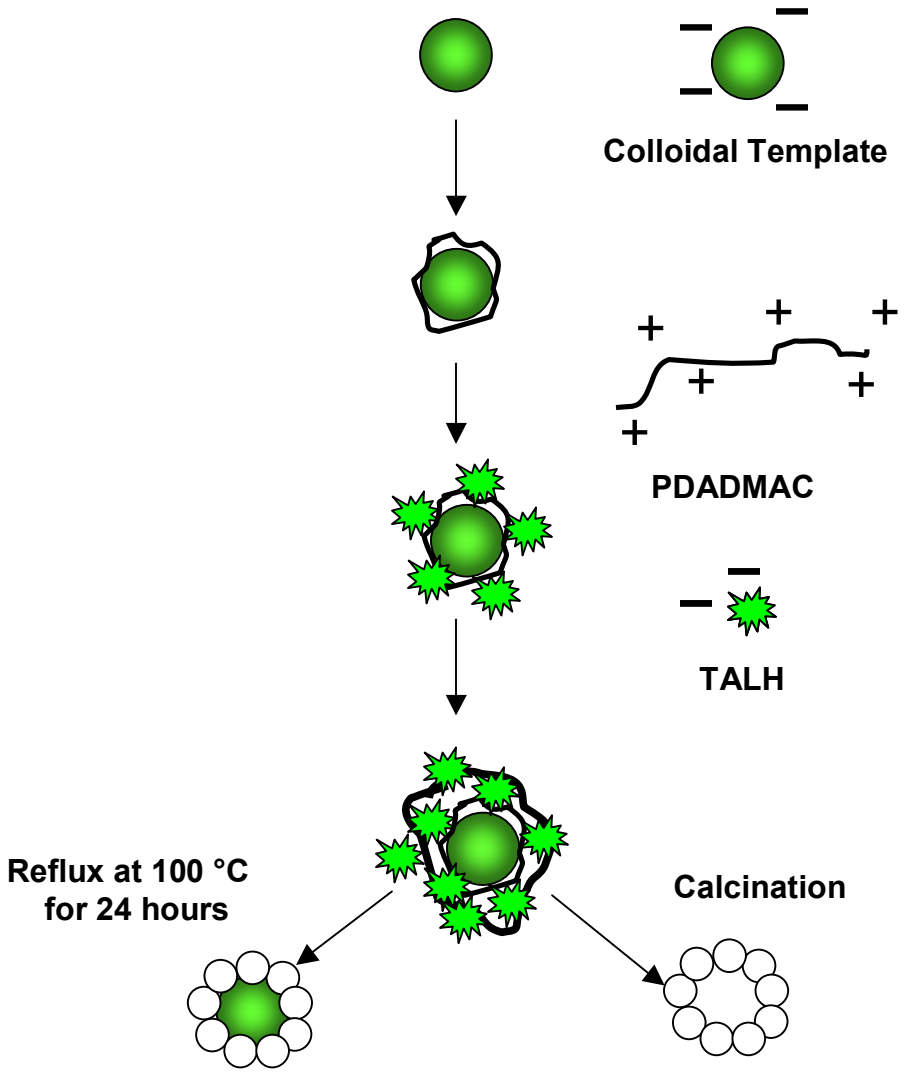

Figure 6: Schematic of Layer-by-Layer synthesis.

Unlike other titanium alkoxide precursors that rapidly hydrolyze in water, TALH is stable in aqueous solutions at room temperature and neutral pH. Therefore, it can be selectively hydrolyzed and condensed during refluxing in water or calcination. Advantages of the

LBL method are the nanoscale control of the wall thickness by varying the number of deposition cycles, careful optimization of solution conditions is not required, and layer deposition is conducted in aqueous solution which eliminates the need for expensive solvents. The principal disadvantages of the LBL method are the extensive and time consuming centrifugation and washing steps required between each layer and the large amount of sacrificial polymer incorporated into the shell.

2.3 Titanium Dioxide Pigments

2.3.1 TiO_2 Uses

Titanium dioxide is used to impart whiteness, brightness, and opacity to a wide range of products including paper, coatings, paint, plastics, rubber, printing inks, synthetic fibers, ceramics and cosmetics (60). As shown in Figure 7, the majority of TiO_2 pigment demand is for paints and coatings (57%), followed by plastics (22%), and paper (12%).

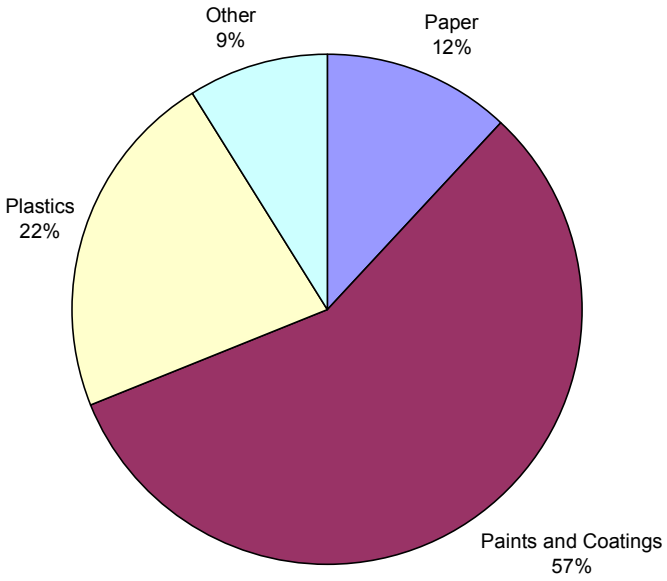

Figure 7: Global TiO_2 pigment demand by market.

Titanium dioxide is used in papermaking both as a filler pigment and in coating applications. In North America coated paper accounts for about half of TiO_2 pigment usage, uncoated printing and writing accounts for nearly a quarter, and others, in order of TiO_2 usage, are coated paperboard, decorative laminates, and specialty papers. While papermakers have traditionally used much cheaper fillers than TiO_2 to achieve brightness and opacity, there are many grades that require TiO_2 to reach stringent opacity targets. In addition, papermakers are continually shifting to lighter basis weights as raw material prices increase. The rise of postage rates is also forcing printers of catalogs and magazines to shift to lighter basis weights. TiO_2 is particularly suitable for these low basis weight applications since it allows reduced grammage while maintaining opacity.

With the rise in cost of other papermaking raw materials such as fiber, TiO_2 usage is becoming more economically viable for the papermaker. Papermakers are increasing the use of cheap fibers from recycled, mechanical, and high kappa number pulps, which requires a more superior opacifying pigment like TiO_2. Titanium dioxide pigment can allow the papermaker to be more flexible about selecting pulp while ensuring high quality. The pigment industry expects a 3.1% per year demand growth for TiO_2 over the next several years with about 60% of this growth coming from China. While TiO_2 markets are fairly mature and GDP driven in traditional North American and European markets, per-capita consumption increases as quality of life improves. This phenomenon is now occurring in Asia and China in particular.

2.3.2 TiO_2 Properties

Titanium dioxide occurs in three crystalline phases, the two tetragonal forms anatase and rutile and a less common orthorhombic form brookite. However, only rutile and anatase are used for pigments. The crystal structures of anatase and rutile are illustrated in Figure 8.

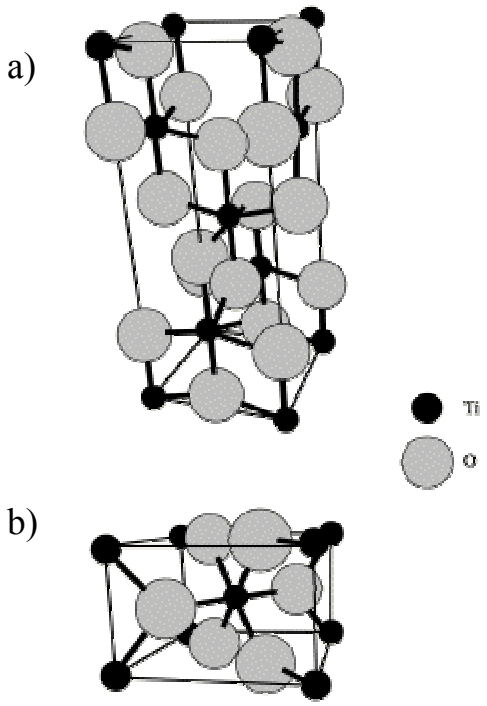

Figure 8: Crystal structures of the (a) anatase and (b) rutile phases of TiO_2.

The whiteness of TiO_2 pigments depends primarily on the crystalline phase, the purity, and the particle size. Any transition elements present in the crystal structure have an adverse effect on whiteness, so manufacturing conditions are of greatest importance. Anatase pigments have a less yellow undertone compared with rutile (60). However, slight difference in TiO_2 pigment brightness will have no affect on opacifying efficiency and very little affect on its paper brightening capability (61). Since the rutile crystalline phase has a higher index of refraction than anatase (2.73 compared to 2.55 at λ=572 nm) and thus more opacifying power, rutile pigment is most often used especially for higher basis weight grades that typically have a dark, unbleached base like coated groundwoods and board. In addition, anatase is more photoreactive than rutile and can catalyze the

oxidative degradation of organic materials when they are exposed to sunlight or other sources of near-ultraviolet radiation. Thus, even though rutile is more expensive to produce, it is more desirable because of its greater opacifying power and less degradation of the paper and surface coating when exposed to sunlight (62). However, since anatase adsorbs less UV light than rutile, it is used in all grades that require fluorescent whiteners.

The reduction in paper strength upon addition of filler pigments like TiO_2 is a well-known and undesirable phenomenon. Strength loss is increased as particle size of the filler decreases since there are more particles on a mass basis to disrupt interfiber hydrogen bonds. However, despite its small particle size, TiO_2 causes about the same degree of strength loss as other filler pigments because lower concentrations are required to achieve desired levels of opacity and brightness (61).

2.3.3 Manufacture of TiO_2 Pigments

Titanium derivatives occur in nature as minor components in many rocks. However, the only commercial sources are rutile ore, obtained from heavy sands, and ilmenite, an iron titanate, which is the major source for pigment production. There are two processes for the commercial production of TiO_2 pigments: the hydrolysis of titanyl sulfate solutions (the long-established sulfate process), and the high-temperature oxidation or hydrolysis of gaseous titanium tetrachloride (the more recent chloride process). Traditionally, the choice of process has been partly dictated by available raw materials. The sulfate process

uses only ilmenite, while the chloride process uses rutile or beneficiated (reduced iron content) ilmenites (62).

2.3.3.1 The Sulfate Process

The production of titania by the sulfate process involves several stages, namely, dissolution of the ilmenite ore in hot, concentrated sulfuric acid to form a solution of ferrous and titanyl sulfates, reduction of any ferric ions present, clarification to remove insoluble residues, cooling and removal of the bulk of the iron as crystalline, hydrated ferrous sulfate, boiling and hydrolysis of the mother liquors to yield a titania precipitate, washing the precipitated hydrous titania to remove residual ferrous sulfate, and calcination to produce anatase or rutile pigments. Hydrolysis and precipitation of the hydrous titania into anatase particles is hastened by the addition of anatase seed nuclei followed by calcination at 800 °C to 1000 °C, which allows crystallization and growth of the particles to a uniform and optimum size. Production of rutile is achieved by the addition of rutile seed nuclei during hydrolysis of the titanyl sulfate solution followed by calcination at 900 °C to 1200 °C. Formation of rutile pigments is also assisted by doping of the hydrous titania with Zn^{2+} or Al^{3+} ions, which act as rutilization catalysts and able rutilization to occur rapidly at lower calcination temperatures and thus to avoid excessive particle growth and pigment discoloration which can occur on prolonged heating at higher temperatures. The calcined particles are then ground in water containing dispersants to break up the sintered particle aggregates and dried. The sulfate process is the technically simpler of the two methods and the process conditions for optimal properties are well established. However significant disadvantages of the sulfate process

are the difficulty in recycling the sulfuric acid, limited market for the byproduct ferrous sulfate, and the environmental consequences of the disposal of large volumes of strongly acidic liquid waste (62).

2.3.3.2 The Chloride Process

The chloride process was developed relatively recently, is more environmentally sound, and yields only rutile pigments. Titanium tetrachloride, $TiCl_4$, is the raw material for the process and is prepared by heating rutile ore or beneficiated ilmenites with carbon in a stream of chlorine at 900 °C. After purification to remove residual ferric chloride and other volatile contaminates, the $TiCl_4$ is mixed with rutilization catalyst and the mixture vaporized and burned in a stream of oxygen at approximately 1000 °C to 1500 °C. The chlorine byproduct is recycled. The pigment is then neutralized to remove surface chloride ions by treatment with steam, milled, and classified to remove particles outside the optimum range. While the chloride process is superficially simple, proper design of the burners and careful control of the reaction conditions are necessary to reduce aggregates and oversized particles (62). Chloride lines have lower manufacturing costs while producing pigments of higher quality compared to sulfate lines. Therefore a major continuing trend is to shut down sulfate lines and construct or expand upon chloride lines. The last anatase sulfate plant in the US was shut down in 2004 and anatase pigments are now entirely imported (63).

2.4 Light Scattering by Titanium Dioxide Pigments

2.4.1 Light Scattering Theory

The opacifying power of TiO_2 pigments embedded in a medium results from their ability to scatter light. Scattering is a general physical process whereby electromagnetic radiation, such as light, is forced to deviate from a straight trajectory by one or more localized non-uniformities in the medium through which it passes. The types of non-uniformities that can cause scattering within the medium include pigments, bubbles or air pores, and defects in crystalline solids. Electromagnetic radiation is a self-propagating wave in space with electric and magnetic components that are in phase with each other and that oscillate at right angles to one another and to the direction of propagation. In physics, electromagnetic waves are visualized as infinite, constant-frequency waves, or plane waves, whose wavefronts are infinite parallel planes of constant amplitude as illustrated in Figure 9.

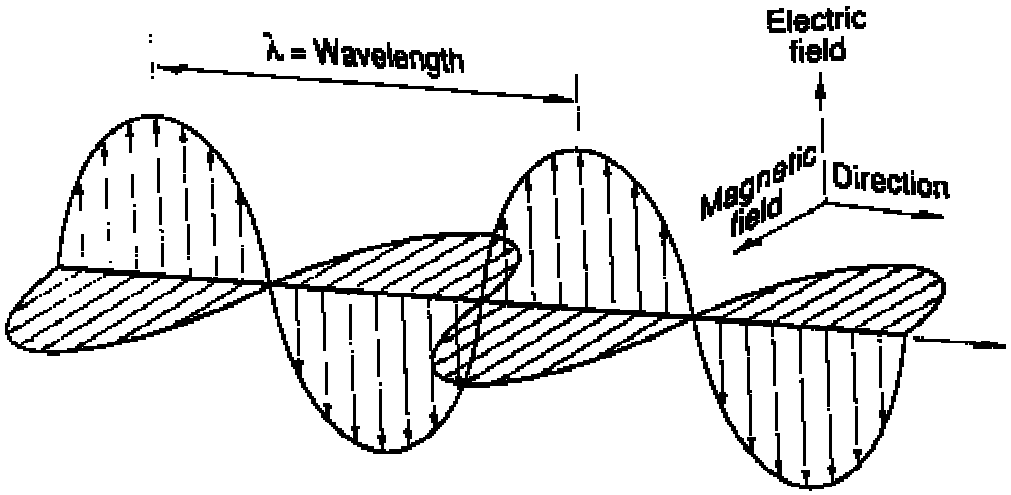

Figure 9: The electric and magnetic fields of an infinite plane wave.

Electromagnetic radiation is classified into categories according to the frequency of the wave with visible light having a wavelength, λ, ranging from about 400 to 700 nm, as depicted in Figure 10.

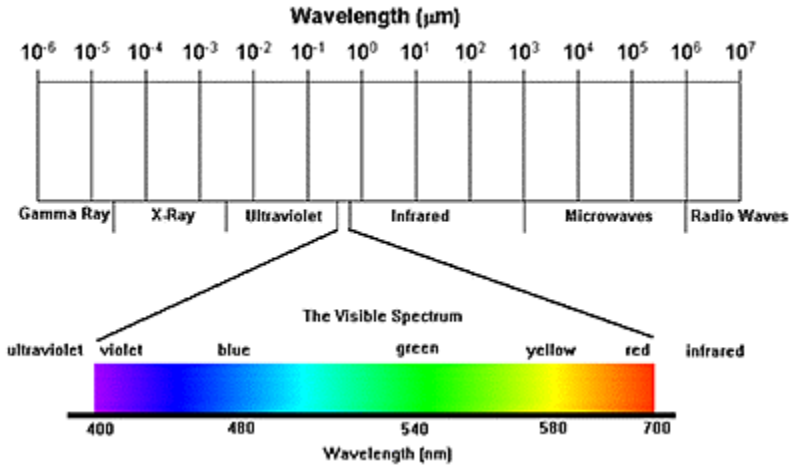

Figure 10: The electromagnetic spectrum.

Mechanistically, electromagnetic scattering results from the fact that matter is composed of discrete electric charges, electrons and protons. As explained by Bohren and Huffman (64), if an object, which could be a single electron, an atom or molecule, or a solid or liquid particle, is illuminated by an electromagnetic wave, electric charges in the object are set into oscillatory motion by the electric field of the incident wave. These accelerated electric charges radiate electromagnetic energy in all directions. This secondary radiation is the radiation scattered by the object. In addition to reradiating electromagnetic energy, the excited elementary charges may transform part of the incident electromagnetic energy into other forms (thermal energy, for example), a process called absorption. Mie theory describes the scattering of electromagnetic radiation of arbitrary wavelength (considered to be an infinite plane wave) by an isolated, optically isotropic sphere of arbitrary diameter embedded in a homogeneous medium. The theory provides complete analytical solutions of Maxwell's equations, which describe the behavior of electric and magnetic fields through media, for a sphere, a concentric sphere, and several other simple geometries. These solutions provide the intensities, phases, and scattering angle of the scattered light. At a particular point from the scattering object, the total scattered field is obtained by superposing the scattered wavelets where account is taken for their phase differences, which depend on scattering direction. Thus the scattering field changes with scattering direction. Mie theory assumes single scattering where the number of particles is sufficiently small and their separation sufficiently large so that, in the neighborhood of any particle, the total field scattered by all the particles is small compared with the external field. With this assumption, the total scattered field is the sum of the fields

scattered by individual particles, each of which is acted on by the external field in isolation from the other particles. In other words, the total irradiance scattered by a collection of dilute individual particles is the sum of the irradiances scattered by the individual particles (64). An advantage of Mie theory is that it is easily implemented computationally. A disadvantage is that it is limited to certain particle shapes and is not applicable to the myriad systems in which the scattering features are irregularly shaped and/or optically anisotropic (65).

2.4.2 Relationship between Light Scattering by TiO_2 and Film Opacity

Pigments impart opacity to the medium in which they are embedded by preventing light from passing through the material by either reflecting it backwards or absorbing it. Figure 11 depicts an optically uniform film that has virtually no opacity because it contains no pigments. Light strikes the surface where some is reflected but most travels through the film where more is reflected at the bottom surface. The reflected parts impart only a small amount of opacity to the film. The quantity reflected depends on the angle of the incident light, the refractive index of the film and the substrate to which the film is attached (66).

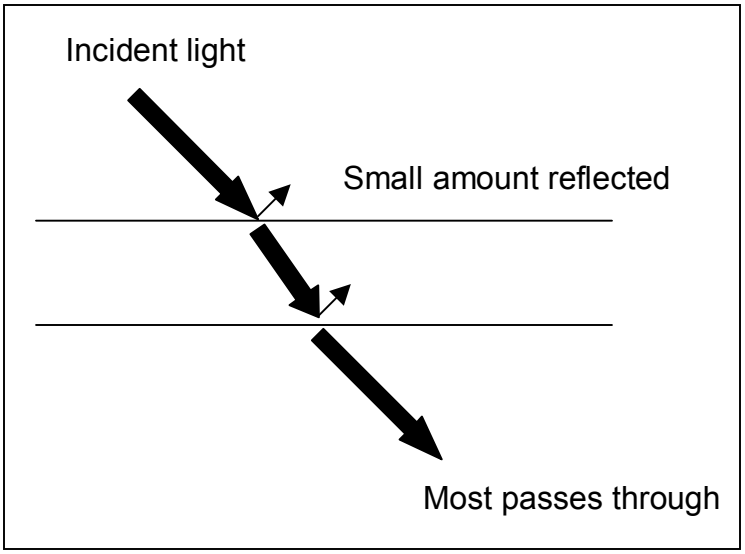

Figure 11: Optically uniform film with no pigments having low opacity because of minimal light scattering (adapted from Balfour 1990).

For films containing pigments, opacity is generated from light scattering by the pigments upon interaction with incident light via the mechanisms of refraction, diffraction and reflection (67). These mechanisms are illustrated in Figure 12.

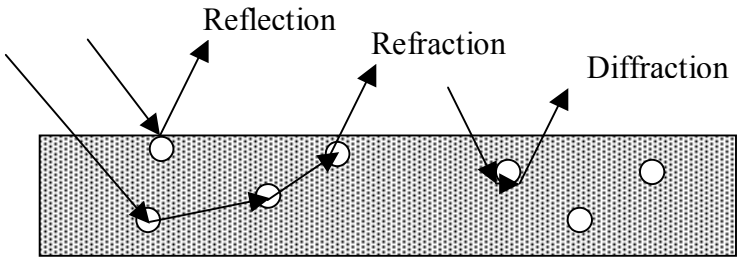

Figure 12: Mechanisms of light scattering by pigments embedded in an optically uniform film (adapted from Logan 1995).

Diffraction is the bending of light as it passes a small particle and depends only on particle size. As a particle becomes smaller, the mass of the particle decreases and the charges in the particle oscillate in concert with the electromagnetic wave of the passing

light. These oscillating charges then produce a change in the electromagnetic field and change the direction of the light (68). The size of the particle giving the most light scattering depends on the wavelength of the incident light and the refractive indices of the particle and the medium. Reflection and refraction result from the difference in refractive index between the pigment and the medium in which the pigment is dispersed. The fraction of the intensity of incident light that is reflected from the interface, R, is given by Fresnel's equation:

$$R = \left(\frac{n_1 - n_2}{n_1 + n_2} \right)^2 .$$

Equation 1: Fresnel's equation for the reflection of light.

where n_1 and n_2 are the refractive indices of the pigment and the medium, respectively. Refraction is the change in direction of light due to a change in its speed as it passes between two materials with different refractive indices. Increasing the difference between n_1 and n_2 will give higher refraction.

Reflection defines the brightness and color the pigment will contribute to the film. White pigments, such as TiO_2 reflect all wavelengths of light and are assumed to have negligible absorption, while black pigments absorb all light, and colored pigments absorb some wavelengths and reflect others. Ambient white light is composed of all colors of the spectrum but can be simplified to be made up of red, green, and blue. When a film contains a red pigment for example, the green and blue parts of incident light are

absorbed while the red is reflected. The reflected light is what the observer sees and so the pigment and film are red. If enough black or colored pigment is present, high opacity can be achieved through absorption alone. White pigments, however, impart opacity only through the multiple reflections, refractions, and diffractions discussed above. Figure 13a illustrates how light can be reflected and refracted at the surface of a white pigment yielding light scattering in many directions, and Figure 13b suggests how complicated the scattering becomes for multiple pigments embedded in a film (66). Figure 13c illustrates that for typical white pigments, light is mainly scattered in the forward direction and therefore must have a sufficient number of encounters with different pigments to be turned around. Thus, in practical applications the opacity of a film depends on the predominant direction in which the pigment scatters light and the number of times the light is scattered by other particles (69).

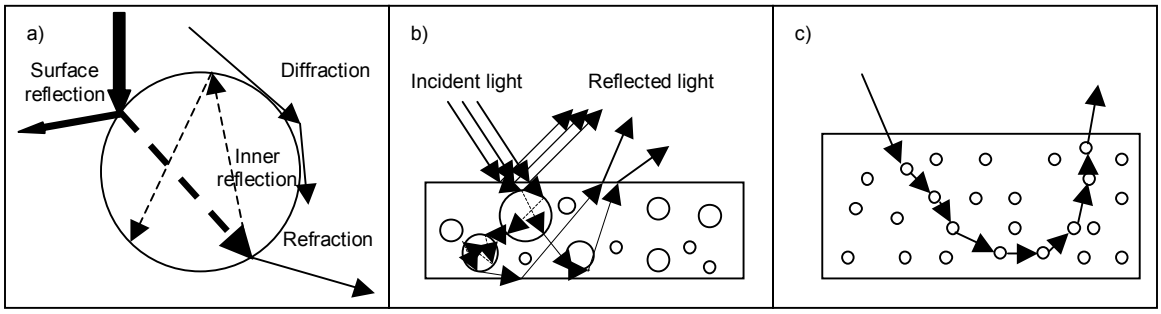

Figure 13: Complexity of light scattering from (a) a single pigment, (b) multiple pigments, and (c) multiple forward scattering pigments (adapted from Balfour 1990 and Bruehlman et al. 1961)

Film opacity is also affected by the surface roughness of the film. Since a rough surface has a greater surface area and can reflect the light at a variety of angles, less light goes

into the film and, consequently, the opacity is greater than for a smooth film. This phenomenon is illustrated in Figure 14 (66).

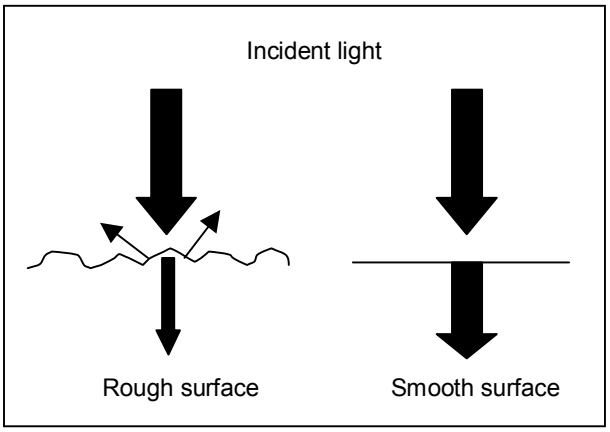

Figure 14: Dependence of light scattering on film surface roughness (adapted from Balfour 1990).

Air pockets, or pores, within the film also greatly impact opacity. For polymeric films like paint, air gets incorporated into the film as the concentration of pigment becomes so great that there is insufficient medium to completely surround the particles. For lightly or moderately pressed paper, the pore structure of the sheet is determined by pigment and fiber packing. For highly pressed sheets, the air pores are almost completely removed as the fibers are pressed into intimate contact. Since air has a lower refractive index (1) than resin (1.51) and cellulose (1.53), light scattering due to refraction upon incorporation of air increases for paints and papermaking applications, respectively, and opacity increases (70). Highly pressed papers, like vellum, have very little air and are translucent. The importance of pores in maintaining opacity targets in paper is illustrated by a DuPont customer whose poor paper machine runnability required a 25% increase in TiO_2 loading to make-up for the opacity lost from only a 5% drop in sheet pore structure (63). Finally,

the opacity of a film is also dependent on film thickness. As film thickness increases, opacity asymptotically approaches 100%.

2.4.3 Variables Affecting Light Scattering by TiO_2

The light scattering efficiency of TiO_2 in pigment applications depends on its refractive index, its particle shape and size, particle size distribution, the degree of particle agglomeration, the refractive index of the medium in which it is dispersed, the concentration of the dispersion, and the wavelength and angle of incident light (71).

2.4.3.1 Refractive Index

Transparent media such as glasses are optically isotropic which means that light behaves the same way no matter which direction it is traveling in the medium. These materials have only one index of refraction. However, many crystals like TiO_2 are optically anisotropic and the behavior of light traveling through the medium depends on the direction of propagation and polarization of the light with respect to the crystal structure. Both anatase and rutile exhibit tetragonal crystal structures with a single optic axis (parallel to the z-axis). Therefore both crystals are optically anisotropic and have two different refractive indices at a given wavelength: the ordinary n_o (for radiation polarized in the x or y direction; perpendicular to the z-axis) and the extraordinary n_e (for radiation polarized in the z-axes). Light waves from sunlight and almost every other form of natural and artificial illumination have different polarizations, or electric field vectors that vibrate in all the planes perpendicular to the direction of propagation. Thus, the birefringence phenomenon, or double refraction, decomposes this light into two rays. The

ordinary ray passes straight through the material which is plane polarized with the E vector perpendicular to the optic axis, while the extraordinary ray which is plane polarized with the E vector parallel to the optical axis is refracted. This phenomenon is illustrated in Figure 15.

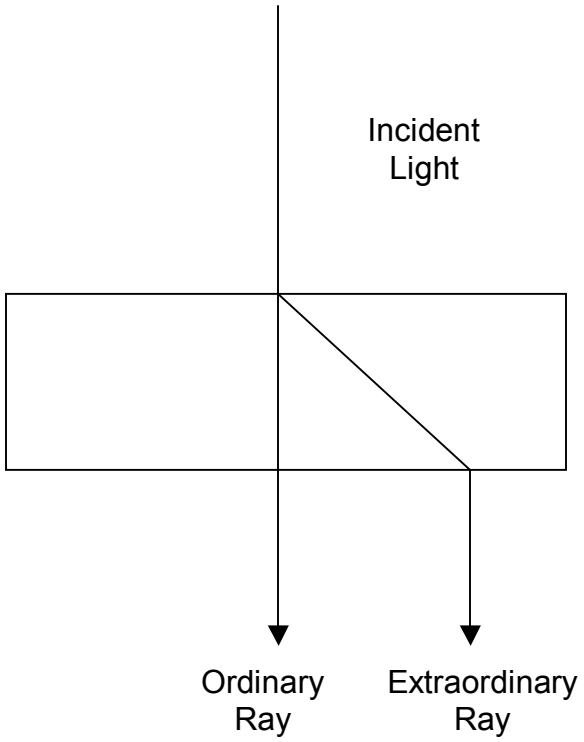

Figure 15: The double refraction of light by a birefringent crystal.

Both refractive indices for rutile have been determined by multiple researchers over a wide range of wavelengths. However, experimental investigations of anatase have been comparatively limited, apparently due to the scarcity of large, defect free crystals. The

opacity of paper is, by definition, evaluated at 572 nm. For rutile illuminated at this wavelength, $n_o = 2.63$ and $n_e = 2.93$, while for anatase $n_o = 2.58$ and $n_e = 2.50$ (65, 72). Traditionally, computational investigations of the light scattering properties of rutile titania are based on Mie Theory, which is theoretically limited to the case of optically isotropic spheres. Thus Mie theory should be invalid for evaluating optically anisotropic titania particles. However, Palmer et al. have shown that serious errors are not encountered for rutile when using an average index approximation (73). For this method, the refractive indices encountered by light polarized parallel to each of the three principle axes (a, b, and c) of the rutile crystal are averaged. This average refractive index n_{ave} is then used in Mie Theory calculations. Since the ordinary refractive index n_o is encountered by light polarized parallel to both a and b and the extraordinary refractive index n_e is encountered by light polarized parallel to c only, the expression for n_{ave} is (65):

$$n_{ave} = \frac{2n_o + n_e}{3}$$

Equation 2: Average refractive index approximation.

At 572 nm n_{ave} is 2.73 nm for rutile and 2.55 for anatase. The higher index of refraction of rutile pigments accounts for about a 15% increase in opacity over anatase pigments in papermaking applications (63).

2.4.3.2 Particle Size

For commercial TiO_2 pigments, the major hiding power variables controllable by the manufacturer are particle size, or median diameter, and width of the size distribution. Figure 16 shows the effect of monodisperse rutile particle size on scattering efficiency in a polymer film irradiated at 550 nm as determined from Mie scattering calculations that take into account multiple scattering, a term discussed below (74). As shown, an optimum size exists, approximately 210 nm, for maximum hiding power. This size changes slightly depending on the wavelength of incident light and the refractive index of the medium.

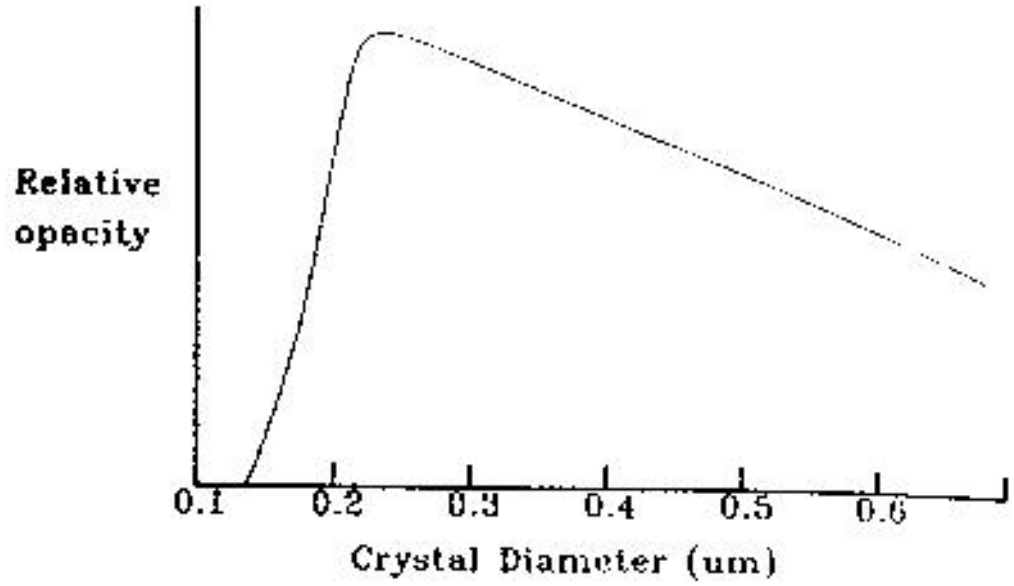

Figure 16: Effect of monodisperse rutile particle size on hiding power in a polymer film irradiated at 550 nm as determined from Mie scattering calculations (Balfour 1990).

However, commercial TiO_2 is not monodispersed. Mie scattering calculations and experimental data show that monodistributed TiO_2 gives an approximately 15% increase in hiding power over commercial polydispersed TiO_2. Lastly, the particle size of TiO_2 pigments is often not equivalent to the TiO_2 crystal size. Crystal size refers to the fundamental size of individual crystals. Particle size refers to the overall size of particles in the system. Often the particles supplied by the manufacture are composed of several crystals as a result of twinning during precipitation and sintering during calcination (74).

2.4.3.3 Pigment Concentration

As Figure 13(b) and (c) suggests, the hiding power of pigments also depends on the spatial distribution of the particles. For this reason the pigment industry is standardized in terms of pigment volume concentration rather than weight concentration. The pigment volume concentration (pvc) is expressed as a percentage and is the volume of the pigment relative to the total volume of the film. Figure 17 shows the effect on paint film opacity when the TiO_2 pvc is increased from zero to 70%. For up to about 10%, opacity increases in proportion to the amount of additional pigment. However, above this level the increase in opacity becomes less than the amount of pigment added until from 25-50% a decrease in opacity is observed. Pigment manufactures call this loss in scattering efficiency the crowding effect. At 50%, the point known as the critical pigment volume concentration (cpvc), opacity begins to increase again. The cpcv is the point when air becomes incorporated into the film and enhances opacity as discussed above (66).

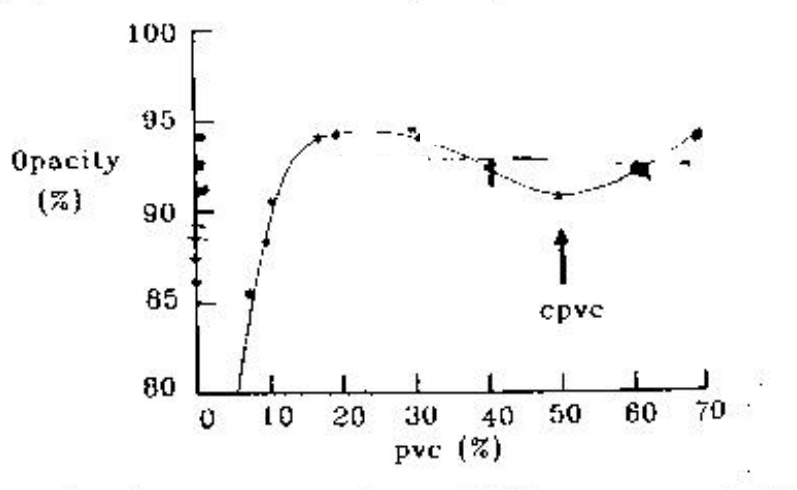

Figure 17: Dependence of film opacity on pigment volume concentration (Balfour 1990).

2.4.4 Multiple versus Dependant Scattering

An ensemble of particles exhibits two different complex scattering phenomena: multiple scattering and dependent scattering. Multiple scattering is the rescattering of already scattered light upon contact with several different well-dispersed pigments in a film as illustrated in Figure 13(b) and (c). This phenomenon occurs when a medium is optically thick, that is when scattered light has a reasonable chance of encountering another scatterer before it is observed. Multiple scattering can occur in very dilute systems, like interstellar space, where the physical thickness of the medium provides optical thickness. Multiple scattering also occurs in concentrated scattering systems such as paints and coatings where the high concentration of scatterers provides optical thickness in a fairly thin film. In both cases the combination of concentration and path length results in light experiencing several scattering interactions before it leaves the scattering medium. Thus, multiple scattering depends on the optical thickness of the scattering medium, not directly

on the volumetric concentration of pigment (75). A criterion for the application of multiple scattering theories is that no near-field optical interactions exist between the scattering features. This condition requires that the scattered wavefront produced by a particle develops independently of neighboring particles and, in pigment applications, is met only in dilute dispersions of particles not exceeding ~5% by volume (65).

Dependent scattering, on the other hand, depends on volumetric concentration and arises from the perturbation of single-particle scattering by near-field optical interactions with neighbors in close proximity. Unlike multiple scattering, dependent scattering does not occur in a system as dilute as interstellar space. This phenomenon is observed only above a threshold pigment concentration and is thought to cause the decrease in light scattering known as the crowding effect (75). The detailed mathematical description of near-field interactions between neighboring pigments is complex, and the development of understanding of these effects in systems of practical interest is still in the earliest stages. The use of large-scale numerical computation is essential in approaching these problems rigorously (65).

2.4.5 Multiple Scattering

2.4.5.1 Mie Theory

Mie theory, the fundamental case in the analysis of electromagnetic radiation scattering, is based on single scattering, in which the interaction between radiation and a single, isolated scatterer is considered. A qualitative criterion for the assumption of single scattering is that each particle in an ensemble experiences the same incident electric field, with negligible scattered field from other features in the ensemble. Mie theory allows calculation of the scattering cross section, C_{sca}. Since the value of C_{sca} depends on sphere radius, it is useful to normalize this value using the geometric properties of the particular sphere of interest (65). For many applications, C_{sca} is normalized by the particle cross-sectional area to give the light scattering efficiency, Q_{sca}. For a sphere,

$$Q_{SCA} = \frac{C_{sca}}{\left(\pi r^2\right)}$$

Equation 3: Light scattering efficiency for a sphere.

For pigment applications, C_{sca} is typically normalized by volume, yielding the scattering coefficient per micron (SCPM). For a sphere,

$$SCPM = \frac{C_{sca}}{\left(\frac{4\pi a^3}{3}\right)}$$

Equation 3: Light scattering coefficient per micron for a sphere.

However, as mentioned above the hiding power of a pigment depends not only on the amount of light it scatters, or its scattering coefficient SCPM, but also on the angle at which the light is scattered and on the number of multiple scattering events, which determines how much of the incident light will be turned backwards rather than passing through the film. Since the intensity of scattered light varies with the scattering angle, the scattering coefficient must be corrected with the asymmetry parameter g, which is the average cosine of the scattering angle, weighted by scattering intensity. The asymmetry parameter provides information about the relevant importance of forward and back scattering by spherical particles. In the context of multiple scattering, where radiation encounters a large number of independently scattering particles while traversing an ensemble of such particles, the asymmetry parameter strongly effects the redirection of scattered radiation and therefore the scattering efficiency of the ensemble of particles as a whole. For a particle that scatters light isotropically (i.e. the same in all directions), g vanishes. The asymmetry parameter also vanishes if the scattering is symmetric about a scattering angle of 90°. If the particle scatters more light toward the forward direction ($\theta = 0°$), g is positive, while g is negative if the scattering is directed more toward the back direction ($\theta = 180°$) (64). The scattering parameter, σ, the industrially preferred parameter for correlations with experimental data for systems on which multiple scattering is predominant, combines the asymmetry parameter and the scattering coefficient SCPM as follows:

$$\sigma = SCPM(1 - g)$$

Equation 4: Light scattering parameter.

2.4.5.2 Kubelka-Munk Theory

The Kubelka-Munk theory is an approximate multiple scattering theory that attempts to explain the light scattering and opacity of paint films and paper containing pigments which are optically thick enough for multiple scattering to occur. The theory is phenomenological which means that the scattering and absorption coefficients it provides describe the capacity of a material to scatter and absorb light but do not provide physical information on the nature of the scattering event or on the scattering and absorption characteristics of a single particle. Practically, experimental reflectance measurements are made and analyzed using Kubelka-Munk (K.M.) theory. This method is largely used by paint and papermakers to predict the effect of changes in pigment formulation and sheet, coating, or film thickness on opacity. This general approach avoids labor intensive trial and error experiments to achieve desired optical properties. For further discussion of Kubelka-Munk theory, several measurement definitions must be defined. Opacity is measured using a light source with λ=572 nm and is evaluated as a contrast ratio, C, which is the reflectance of a single sheet with a perfectly black backing (R_0) divided by the reflectance with a white backing (such as 89% reflectance, $R_{0.89}$ for TAPPI opacity). The reflectance of an (effectively infinite) thick pad of paper is R_∞ and is known as reflectivity (76). Now, following the derivation presented by Leskela, consider a plane parallel sheet of material of thickness D and reflectivity R irradiated with light of intensity I_0 incident as shown in Figure 18 (77). Behind this sheet is a surface of reflectance R'. The light which re-emerges from the top surface of the sheet after scattering, absorption or transmission has intensity I. At a distance z from the bottom

surface of the paper there is a thin layer of thickness dz and scattered light is traveling both upwards and downwards through it with intensities i_R and i_T, respectively.

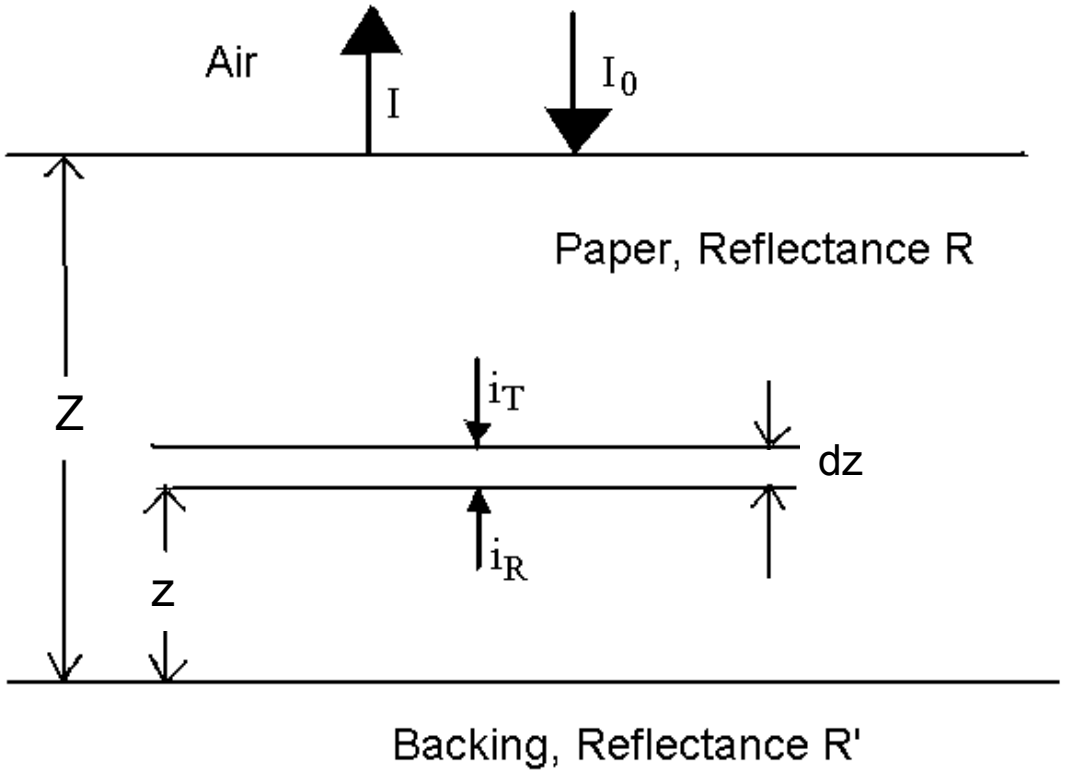

Figure 18: Incident and scattered light from a sheet with differential thickness dz.

The light streams i_t and i_r are reduced within the layer by absorption and backscattering. The intensities of the streams in dz change as:

$$d\,i_r = -(S+K)\,i_r\,dz + S\,i_t\,dz \quad \textbf{(5)}$$

$$-d\,i_t = -(S+K)\,i_t\,dz + S\,i_r\,dz \quad \textbf{(6)}$$

where K is the K.M. absorption coefficient and S is the K.M. scattering coefficient. By dividing the upper equation by i_r and the lower equation by i_t and then summing these two we obtain:

$$\frac{d\,i_r}{i_r} - \frac{d\,i_t}{i_t} = d\ln\frac{i_r}{i_t} = -2(S+K)dz + S(\frac{i_t}{i_r} + \frac{i_r}{i_t})dz \quad \textbf{(7)}$$

The reflectance of the whole sheet is defined as $R=I/I_0$. Thus, the reflectance for a thin layer dz can be defined as $r=i_r/i_t$. Thus by expressing dlnr=dr, we obtain

$$\frac{dr}{r^2 - 2\frac{S+K}{S}r + 1} = Sdz \quad \textbf{(8)}$$

Applying the two boundary equations i) if z=0, $r=R_0=0$ and ii) if $z=\infty$, $r=R_\infty$ and integrating the equation by partial fractions we obtain expressions for R_0 and R_∞ in terms of S, K, and D:

$$R_\infty = 1 + \frac{K}{S} - \sqrt{\frac{K^2}{S^2} + 2\frac{K}{S}}$$

Equation 9: Kubelka-Munk equation for reflectivity

$$R_0 = \frac{e^{SD(\frac{1}{R_\infty} - R_\infty)} - 1}{\frac{1}{R_\infty}e^{SD(\frac{1}{R_\infty} - R_\infty)} - R_\infty}$$

Equation 10: Kubelka-Munk equation for reflectance

Therefore, by measuring R_0 and R_∞, the light scattering and absorption coefficients can be determined where S and K are intensive properties and do not depend on the thickness of

sheet. In addition, the theory can be extended to multicomponent mixtures by assuming that the scattering and absorption coefficients of the components are additive. In other words, the values for these coefficients for a particular raw material are assumed to remain unchanged in different mixtures. Thus, if the relative fraction of a raw material I in the mixture is denoted by f_i, the scattering and absorption coefficient of the mixture can be expressed as

$$S = \sum_{i=0}^{n} f_i S_i$$

Equation 11: Kubelka-Munk scattering coefficient for a mixture.

$$K = \sum_{i=0}^{n} f_i K_i$$

Equation 12: Kubelka-Munk absorption coefficient for a mixture.

In practice for papermaking, if one knows the optical properties of each component of the medium such as pulp and filler, then the optical properties of a paper made with any combination of these materials can be predicted. Also, if any two variables of a film R_0, $R_{0.89}$, R_∞ are known, the third can be determined. Finally, Kubelka-Munk can also be used to determine the ratio of absorption to scattering, K/S, by rearranging Equation 9 to give

$$\frac{K}{S} = \frac{(1-R_\infty)^2}{2R_\infty}$$

Equation 13: Ratio of Kubelka-Munk scattering coefficients.

Limiting assumptions of Kubelka-Munk theory are that the particles making up the sheet must be much smaller than the total sheet thickness and that both absorbing and scattering media must be uniformly distributed through the sheet. Also, as a continuum model the theory assumes that the scattering and absorption coefficients are constant throughout the sheet. This requires that the properties of fibers and pigments and their packing remain constant throughout the layer. Finally, the theory can only be used to predict optical properties at the same wavelength of light as the experimental measurements were taken (77).

2.4.6 Dependent Scattering

Since Mie theory is valid only for single scattering, a host of numerical approaches have been developed to determine the radiation scattering properties of a system experiencing dependent scattering effects. The light scattering properties of pigment agglomerates or clusters is of scientific and practical importance and has been studied using several such methods. In addition to dependent scattering effects, such clusters of small spherical particles cannot be studied using Mie theory because they are, in general, profoundly nonspherical in shape. However, since the individual pigment particles making up the aggregate are approximately spherical in shape and therefore allow analytical solutions to the wave equations, it is possible to calculate exactly, by appropriate superposition techniques, the scattering properties of the aggregates. Two popular numerical methods for such clusters are the T-matrix Method and the Finite Element Method.

2.4.6.1 T-Matrix Method

Since its formulation in 1965 the T-matrix method has become one of the most powerful, versatile, numerically accurate, and popular theoretical techniques for rigorously computing electromagnetic scattering by single and compounded particles. A recently published comprehensive reference database cites 700 studies using the T-matrix method published between 1965 and early 2004 (78). The T-matrix approach is based on representing the total scattered field from a cluster as a vector superposition of the partial fields scattered by the individual cluster components such that the total electric field at a point r is:

$$\vec{E}\left(\vec{r},t\right)=\vec{E}^{inc}\left(\vec{r},t\right)+\sum_{i=1}^{N}\vec{E}_{i}^{sca}\left(\vec{r},t\right)$$

Equation 14: Total scattered electric field.

where N is the number of particles in the cluster, $\mathbf{E}^{inc}$ is the incident electric field, $\mathbf{E}_i^{sca}$ ($\mathbf{r}$,t) is the ith partial scattered electric field. The total magnetic field is given by a similar expression (79). The T-matrix approach defines the electromagnetic fields internal to the scattering object in terms of the incident field, then the surface currents in terms of the internal fields, and finally the scattered field in terms of the surface currents. For particle clusters, the T-matrix method is based on representing the total scattered field from a cluster as a vector superposition of the partial fields scattered by the individual cluster components (79). Conceptually, the presence of multiple particles provides more surface irregularities and interfaces for light to scatter. The T-matrix method can account for the constructive (and destructive) interferences of the light waves scattered off all the

surfaces. In this way, one can evaluate the effect of cluster geometry on the superposed intensities of light waves scattered in each direction. A significant advantage of the T-matrix method is that it calculates the orientation averaged scattering properties of the cluster, or the scattering properties of the cluster averaged over all possible orientations of the cluster with respect to the incident light (65).

2.4.6.2 Finite Element Method

As summarized by Thiele and French, the Finite Element Method is based on piecewise solutions of the time-domain form of Maxwell's equation:

$$\nabla^2 E - \varepsilon\mu \frac{\partial^2 E}{\partial t^2} = 0$$

Equation 15: Time domain form of Maxwell's Equation.

where E is electric field amplitude, ε the electric permittivity of the medium, and μ the magnetic permeability of the medium. In practice, this equation is elaborated into an integral form that facilitates numerical solution throughout an extensive three-dimensional volume (65). The computational domain is discretized into a finite number of volume elements the size and shape of which are dictated by the level of accuracy required and the geometry of the features contained within the volume. The coordinate system is defined by specifying edge dimensions, the finite element mesh density, particle position(s) and shape(s), and the optical properties of the constituent materials at the wavelength of interest. Electromagnetic radiation is allowed to propagate within the

finite element model in the time domain, with electric field amplitude and phase computed at each edge in the finite element model at each time step. A sufficient number of time steps are executed to ensure that steady state is achieved. After extrapolation of the calculated near-field scattered electric field amplitudes to far field values, macroscopically observable optical quantities such as the scattering cross-section of the microstructure being modeled and the angular distribution of scattered light can be calculated. Additionally, the simulation of diffuse illumination is accomplished by superimposing the far-field scattered intensities computed in a series of individual computations in which the illumination directions are varied step-wise over the necessary range of orientations (80). An advantage of the Finite Element Method is that it is simple in concept and implementation, while a disadvantage is that required assumptions make it unsuitable for applications in which achieving a very high and controllable numerical accuracy is important (65). Another significant disadvantage of this method, particularly relevant for clusters, is the simulation of random illumination by superposition of the fixed orientation results (quadrature) over a range of incident directions. Recent investigations of the polarimetric scattering properties of sphere clusters have shown that the scattering components can be highly sensitive to the orientation of the cluster with respect to the incident field. Thus, the accurate numerical calculation of scattering properties of a cluster can require an extremely fine quadrature scheme (81).

2.5 TiO_2 Optical Crowding

2.5.1 Evidence of Optical Crowding

The light scattering properties and hiding power of TiO_2 in paper and paint films has been the subject of experimental and theoretical research for many decades. A major component of this research has been to characterize and explain TiO_2 optical crowding. The loss in opacifying power which characterizes optical crowding is observed for two common situations: i) increase in TiO_2 pigment concentration above a threshold value and ii) upon TiO_2 flocculation. Referring back to Figure 17 which shows the effect of TiO_2 volume concentration on opacity of a paint film, we find that up to about 10% pvc, the opacity increases in proportion to the amount of pigment added. However, above this level the individual particles do not act as efficiently and the increase in opacity becomes less than proportional to the amount added. Eventually the opacity reaches a maximum and further increases in concentration above 30% lead to a decrease in opacity until the critical pigment volume concentration is reached.

The state of dispersion also affects TiO_2 hiding power and is defined by its ability to remain separated upon incorporation into a matrix, or upon its degree of flocculation. Figure 19 shows that the opacity of a typical gloss paint decreases as the flocculation gradient increases. The flocculation gradient indicates the degree of flocculation with the higher the value, the greater degree of flocculation (66). Balfour provides SEM images of TiO_2 floccules with different flocculation gradients, fg. For fg = 0.21, the floccules are composed of from two to five primary TiO2 particles and for fg = 0.5 and 0.92, the

floccules have an average of about 10 particles and 30 particles respectively. (82). Values from about 0.2 to 0.9 can be found in commercially available paints (66).

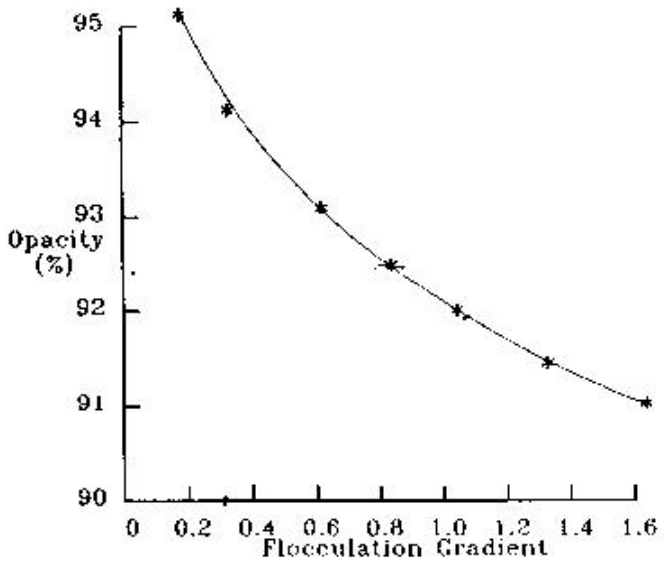

Figure 19: Effect of flocculation gradient on opacity of a gloss paint (Balfour 1990).

2.5.2 Optical Crowding Theories

Several theories exist within the paints and papermaking industries to explain the loss of light scattering efficiency and hiding power for concentrated and flocculated TiO_2 systems. The first theory is based on the refraction of light and states that excellent dispersion of TiO_2 is required, for paper in this case, because opacity is maximized by increasing the contact points between materials of high index of refraction (rutile TiO_2=2.73) and low index of refraction (pulp=1.53, air=1.00). If two high indices of refraction materials are in close contact such that the pigment air or pigment-fiber interfaces are reduced and pigment-pigment interfaces are formed, light scattering is decreased (67). The second theory is based on overlap of the individual TiO_2 particle's

"sphere of influence", or scattering cross section. The scattering cross-section of a small particle represents the theoretical size of the particle in terms of it's ability to influence the propagation of light. Optimally sized particles, about half the wavelength of light, can have cross-sections four times larger than their physical size (68). Thus pigment particles can be considered to have a sphere of influence surrounding them as illustrated in Figure 20(a). When the concentration reaches a certain level these spheres overlap, as illustrated in Figure 20(b) and consequently each of the particles scatters less light, which gives rise to a loss of scattering efficiency. In addition, flocculation gives rise to areas of low and high pvc. The areas of low pvc have low opacity because there is insufficient pigment, while the areas of high pvc also have low opacity because of the crowding effect. Also, according to this theory, particles further into the film are hidden from incident light and do not have the opportunity to scatter it (66).

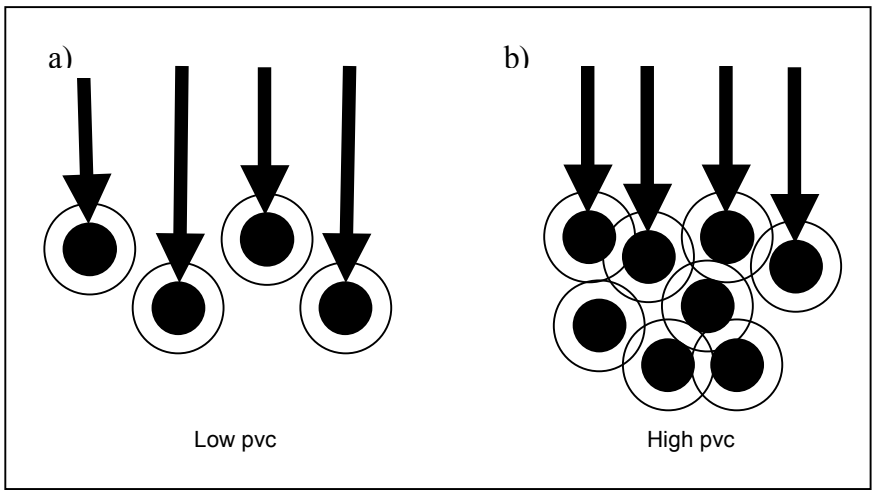

Figure 20: Sphere of influence for pigment particles under (a) low and (b) high pigment volume conditions (adapted from Balfour 1990)

2.6 Light Scattering by Small TiO_2 Aggregates

2.6.1 Conventional Pigment Industry Perspective

Some debate exists in the industry and literature regarding the effect of TiO_2 aggregate size on opacity. Titania aggregates are formed during crystallization and calcination in both the chloride and sulfate processes. Mean particle size, or aggregate size, of the supplied product is then determine by the extent of milling. According to Fields from DuPont, early company experimental data suggests that the potential hiding power improvement when going from a mean aggregate size of 4 particles/aggregate to individual crystals is by a factor of ten to twenty, although the method used to determine this data was not revealed. Again according to Fields, more recent calculations show an approximately 4% hiding power loss for each attached TiO_2 particle as shown in Table 2 (74). The method used to determine this data was also not presented.

Table 2: Dependence of hiding power on TiO_2 aggregate size according to DuPont (Fields 1993)

	Relative hiding power at 0.20 μm
One particle	100
Two particles	96
Three Particles	92
Four Particles	88

In contrast, Hornby and Murley determined that in a well dispersed system only a small portion (20%) of the TiO_2 crystals are present as a single crystal with the remainder being present in groups of two, three, and more crystals. The single crystal fraction was increased by extensive milling with no significant increase in opacity (68).

This last argument is often overlooked and historically the industry does not appear to distinguish between a) the effects of small well-dispersed TiO_2 aggregation opacity and b) the detrimental crowding effects observed for concentrated pigment scenarios. However, the two scenarios are physically quite different as illustrated by the computer simulation of random aggregation performed by Fields shown in Figure 21 (83). While, according to this model, the number of particles per cluster does increase up to about 4 as the particle volume concentration increases to 50%, the most obvious change in the system is the particle crowding, or decrease in distance between all particles and particle clusters.

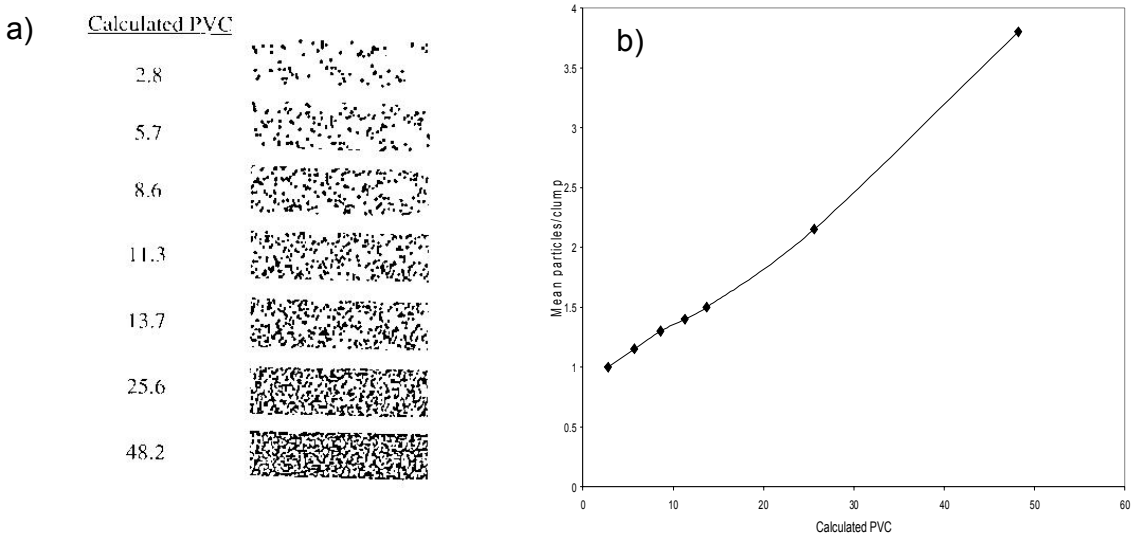

Figure 21: Simulation of random aggregation of TiO_2 particles upon increase of particle volume concentration (Fields 1993)

This concept is further illustrated in Figure 22 which shows (a) the physical crowding of aggregates at high pvc and (b) the large separation of aggregates at low pvc.

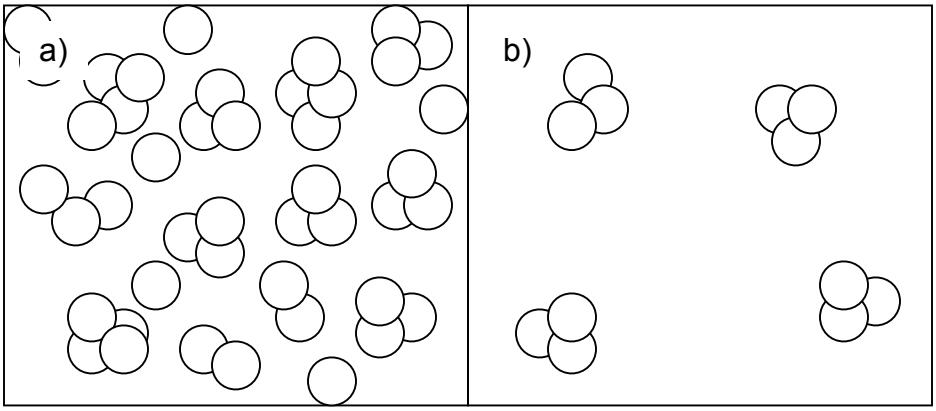

Figure 22: Illustration of physical crowding of TiO_2 aggregates at (a) high pvc and (b) low pvc

2.6.2 Numerical Modeling Perspective

The debate over the optical efficiency of small, well-dispersed aggregates has recently been fueled by several attempts to solve the light scattering problem using theoretical numerical modeling approaches. The dependant scattering of light by particle clusters is important not only to the pigment industry but can also explain environmental issues related to air pollutants such as soot aerosols, light scattering from ice crystals in clouds, and astrophysical phenomena involving the effect of interstellar dust on light propagation and scattering (84). Modeling light scattering from particle clusters requires careful consideration of particle geometry and topography. It is easy to imagine that light scattering depends on the arrangement of the primary particles in the aggregate. For example, an aggregate with significant interior interparticle void space may trap part of the incident light between the particles leading to enhanced scattering, while a linear arrangement of particles would not experience this effect. Another parameter is the location of the aggregate with respect to the polarization of the incident wave and the direction of incidence. This is illustrated in Figure 6 for a pair of identical particles. The electric field E of the incident wave may be either parallel or perpendicular to the pair axis, or completely askew. Thus, an average over either different locations of the aggregate or over different directions of incidence is required (85).

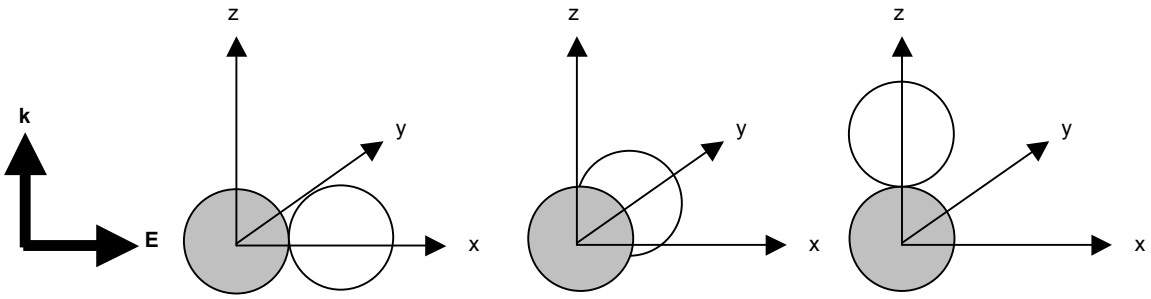

Figure 23: Illustration of arrangement of particle pair with respect to direction of incidence of light (adapted from Quinten 1999)

A variety of conflicting results from the numerical modeling of the light scattering efficiency of particle clusters appear in the literature. Often these studies claim to be investigating the same scattering problem but reach different (and often opposing) conclusions because of different particle sizes and scattering configurations studied, the assumption of different optical constants, consideration or lack of consideration of the asymmetry parameter, and the use of different numerical methods which particularly treat the random illumination problem differently. In addition, due to the lack of rigorous experimental data on light scattering of submicron particle clusters, the validity of the particular numerical methods and codes cannot be tested for appropriateness with a known solution.

Using the Finite Element Method, Thiele determined that clustering of 200 nm rutile spheres illuminated at 560 nm results in markedly reduced scattering on a volume normalized basis compared to an isolated primary particle (65). He performed computations for cluster sizes consisting of 2, 3, 4, 6, 7, 8, 13, 20, 27, and 64 primary particles with the geometry in each case chosen to be the highest symmetry possible. For a four, 13, and 64 sphere cluster, the angle weighted scattering coefficient, σ, decreases

from that of a single, isolated sphere by 30%, 60%, and 70%, respectively. The asymmetry parameter, or degree of forward scattering, is said to increase dramatically with increasing cluster size. Thiele also investigated the effect of interparticle distance for a seven sphere cluster on light scattering efficiency by varying the surface to surface interparticle separation distance from zero to 0.5 micron. He found that while σ is nearly equal to that of a single, isolated sphere for interparticle separation distances greater than 0.2 μm, for interparticle separation distances less than 0.2 micron, σ decreases sharply with decreasing interparticle separation distance. For touching spheres, σ is 35% less than that for a single sphere, indicating a substantial loss in scattering efficiency as a result of particle crowding and agglomeration in the system. Thiele also performed computations for the case of two morphological rutile particles with the same geometry and anisotropic optical properties, i.e. the previous assumptions of perfectly spherical titania particles with an average index of refraction across all angles of incidence were removed. Again he found that σ decreases with decreasing particle separation. For an interparticle separation of 0.5 micron, σ is the same as for a single particle, while for zero separation, σ is 20% lower.

McNeil et al., also using the Finite Element Method, performed calculations for rutile spheres with a surface to surface distance of 75 nm illuminated at 550 nm and found with the pair of particles oriented with the line joining the center of the particles parallel to the incident light direction, scattering strength increases by 38% and backscattering increases by 28% over that of a single particle, whereas if the particles are in a diagonal

configuration with respect to the incident light the scattering strength and backscattering decrease upon addition of the second particle (86).

Using the T-matrix method, Auger et al., assuming spherical TiO_2 crystallites, studied the light scattering cross section per unit volume of aggregates of 13 rutile spheres in a polymeric resin irradiated at 546 nm with primary rutile particle size varying from 40, 80, and 132 nm (87, 88). They found for both compact and linear configurations, an increase in size of the primary particle gives decreased light scattering compared to an isolated particle. These calculations give only the strength of scattering from the cluster and no information of spatial distribution of the scattered energy. They do not account for the orientation scattering efficiency of the aggregates by incorporating asymmetry parameter.

Lastly, Usami used the T-matrix method to study the light scattering properties of TiO_2 aggregates and states that the motivation of his study is to solve the flaw in painting technology which does not distinguish between the loss of optical efficiency of high volume TiO_2 systems and the optical efficiency of small, well-dispersed clusters of TiO_2 (89). In contrast to Thiele, Usami found that scattering efficiency increases as the distance between two identical 200 nm rutile spheres decreases from infinity to 180 nm for illumination at 600 nm with the angle of incidence at 30° to the common axis of the particles and with a refractive index of the medium set to 1.98. At a distance of 180 nm the scattering efficiency is 1.5 times greater than the efficiency for completely separated particles. He also found that the scattering efficiency of the pair of particles at zero

separation increases significantly as the particle radius of the particles increases from 75 nm to 200 nm and that the efficiency of the pair is always greater than the efficiency of the separate particles, regardless of particle size. He also found that the scattering efficiency of the pair for all sizes is greatest when the incident direction of the light is parallel to the axis joining the two particles.

2.7 Light Scattering by Innovative TiO_2 Pigments

2.7.1 Structured and Engineered Pigments

One approach to increase the light scattering efficiency of TiO_2 pigments is to create novel TiO_2 based structures designed to scatter light more effectively than conventional TiO_2 pigments. Modifying pigment structure to enhance light scattering is not a new concept. Pigment suppliers offer several varieties of "Structured and Engineered Pigments" including highly structured or calcined clay, TiO_2/clay aggregates, and hollow plastic pigments. Structured pigments like calcined clay and TiO_2/clay enhance opacity because the aggregation of pigments into larger particles offers more surfaces and void volume to scatter light. Calcined clay's "popcorn" structure results from interparticle sintering upon calcination at 1000 °C, while the TiO_2/clay structure results from chemically binding the two different minerals together. These TiO_2 aggregates give improved brightness and opacity greater than that obtained by mixtures of the two pigments in the same ratio (90).

Uniform, hollow latex plastic pigments are available in a wide variety of particle sizes and void volumes and are typically used in paper coatings to enhance gloss, bulk, brightness, and opacity. These particles enhance opacity by incorporating large amounts of air into the coating. In addition to the air entrapped in the hollow core, their spherical shape entraps air uniformly between the densely packed particles. The performance of the outer surface is like that of solid pigments. When the outer surface is next to air, scattering can occur, but where it is next to binder, little or no scattering can occur. However, unlike solid particles, the hollow spheres have a large air/particle shell interface on its interior surface that is always available to scatter light, no matter what media surrounds the outer surface of the particle (91). Experimental studies have been performed to determine the optimal particle size and void volume for hollow plastic spheres with particle diameters ranging from 260 to 1,060 nm and void volume from 20-50%. Opacity of coated paper increased from a low of 87.65 with a particle diameter of 260 nm and void volume of 20% to a high of 89.81 with a particle diameter of 1,060 nm and a void volume of 50% (92). Another principle benefit of hollow plastic pigments is their exceptional contribution to coated paper bulk with a density of only 0.5 g/mL. This density is much lower than other traditional pigments as shown in Table 3. Because of increasing fiber and mailing costs, papermakers are continually shifting to lower basis weights and looking for ways to maintain bulk. Low density plastic pigments are especially useful in achieving lower basis weights without sacrificing optical performance (93).

Table 3: Densities of common papermaking pigments.

Material	Specific Gravity
Kaolin Clay	2.58
Calcium Carbonate	2.55
Titanium Dioxide (rutile)	4.2
Hollow-sphere Pigment	0.50-0.85

Figure 24 compares the engineered pigments discussed above in terms of light scattering efficiency and price with more conventional papermaking pigments.

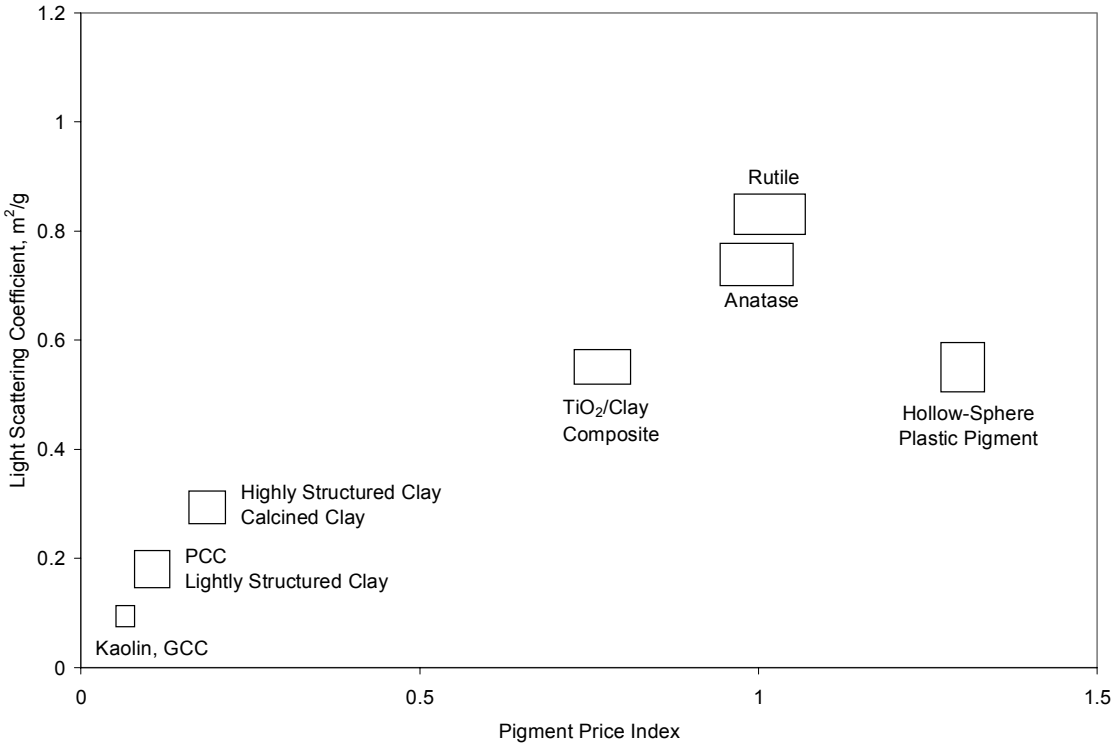

Figure 24: Light scattering efficiency vs. price for several common papermaking pigments (adapted from Atherton et al 1997)

Engineered TiO_2 pigments are currently limited to the relatively simple agglomerated composites mentioned above. However, it is intriguing to wonder by just how much light scattering can be enhanced through synthesis of novel TiO_2 pigments with core-shell or hollow structures for example. If plastic pigments, with their shell refractive index of only 1.59, enhance light scattering as light is refracted between the shell and the air-filled core, one can easily anticipate even more light scattering from a titania shell with a refractive index of 2.73. Novel engineered TiO_2 particles should consist of uniform particles with the lowest TiO_2 content possible because of titania's very high cost and limited supply.

2.7.2 TiO_2 Core-Shell Pigments

Hsu et al were the first group to experimentally and theoretically investigate the hiding power of core-shell titania particles (94). They coated monodispersed spherical silica with titania and evaluated hiding power in a cellulose matrix as a function of core diameter (0.2-1.3 μm) and titania shell thickness. The silica cores were synthesized using the Stober method and coated with amorphous titania via the sol-gel process using titanyl sulfate precursor, and calcined at 1000 °C for 10 minutes. The opacity of the synthesized core-shell particles was measured alone (pure powder) and in a matrix of Avicel cellulose. Both the powder and Avicel cellulose mixture samples were wetted with an unspecified amount of glycerol prior to measurement, presumably to fill the air voids. Optimum opacity was obtained for core-shell particles with an overall diameter of ~ 1.0 μm and a shell thickness of 50 nm, corresponding to about 40 wt% TiO_2 (shell thicknesses beyond 40 wt. % could not be successfully synthesized with their coating

method). The optimized powder gave an opacity comparable opacity to commercial rutile powder when incorporated into the Avicel matrix at constant mass loadings of 17%, 37%, and 50% filler. Using the well-known BHCOAT computer program based on Mie theory as applied to concentric spheres, the authors also calculated the Mie scattering efficiency, Q_{sca}, at λ =546 nm for titania coated silica particles in a cellulose matrix with different ratios of δ/r, where δ is the thickness of the shell and r is the radius of the entire particle. The refractive indices used were cellulose matrix = 1.45, silica = 1.48, and TiO2 = 2.6. From this theoretical evaluation, they found that the light scattering efficiency of core-shell particles wit ha diameter of ~600 nm with $\delta/r = 0.20$ is comparable to that of solid commercial TiO_2. The discrepancy in optimal size between theoretical and experimental investigations was proposed to result from the inhomogeniety of the shell after calcination.

Several years after this study, researchers from DuPont Titanium Technologies published a rebuttal based on theoretical light scattering calculations using the program BHCOAT modified to incorporate the asymmetry parameter, which accounts for the direction of light scattered from a particle (95). The researchers argue that the theoretical calculations performed by Hsu et al. for an isolated particle cannot be used to anticipate the light scattering of TiO_2 in actual films where multiple light scattering occurs between the large number of particles present. The opacity of a film depends on the ability of the pigment to scatter light back in the direction from which it came. A single particle efficiently scatters light, but typically for small spherical particles only a small portion is scattered in the backward direction. However, light scattered by multiple particles is bent a sufficient

number of times to achieve a backwards direction. Thus in practical applications, the reflectance of light by a film (opacity) depends on the predominant direction in which the pigments scatter light and the number of times the light is scattered by other particles. The asymmetry parameter includes the scattering angle to give a scattering parameter that is meaningful to correlate with the value of a pigment for opacification in real applications. In addition, since in pigment applications the performance and cost of formulations depend on particle volume, these authors calculate the scattering coefficient per micron (SCPM), defined as the Mie scattering coefficient divided by particle volume and multiply this value by the asymmetry parameter to obtain the reported scattering coefficient, $\sigma(\mu m^{-1})$. Calculations were performed at λ =560 nm with a shell thickness of 10%, a rutile refractive index of 2.74, and a matrix refractive index of 1.45 which is representative of the average refractive index of typical paper coatings composed of a mixture of clays/carbonates (index of 1.6), starch or latex binders (1.5) and air voids (1). Their calculations show that for a core-shell particle with either a hollow or silica core and a rutile shell thickness of 10% of the particle radius, the most efficient particle structure corresponds to a solid rutile particle with a diameter of 0.2 μm. The highest scattering coefficient for a core-shell particle corresponds to a rutile shell outer diameter of 350 nm and a silica core diameter of 200 nm. However, this scattering coefficient is only 64% of the value for solid rutile. The authors conclude that core-shell pigments are substantially less efficient light scattering materials than pure rutile.

2.8 Effect of Pigment Fillers on Paper Strength

Increasing the filler content of paper sheets offers many advantages including cost savings, protection of world forests by replacing virgin fibers, increasing paper production capacity without the addition of extra pulping capacity, and allowing the use of lower quality, discolored pulp such as mechanical pulp, recycled pulp, and high kappa number pulp (4). However, disadvantages of increased filler loading include reduced paper strength, increased loadings of expensive dry strength aids to help rebuild strength, increased size demand, abrasion, and dusting. Inorganic fillers reduce paper strength by interfering with interfiber bonding, since they have no ability to form similar strong bonds with the fibers. The size of the filler particle, the size distribution, and the shape of the particles are all factors that influence paper strength. For example, in general, the smaller the pigment particles, the greater their negative effect on strength (96).

2.8.1 Paper Strength

The strength of paper derives from both the tensile strength of individual fibers and the bond strength that holds the fibers together. Fiber tensile strength originates from the strong covalent linkages within the polymeric chains of cellulose oriented along the length of the fiber, whereas bond strength results from much weaker intermolecular hydrogen bonds between the hydroxyl groups of cellulose and hemicelluloses of adjacent fibers. While the covalent bonds are on the order of 100 kcal/mol, the strength of R-OH—R-OH hydrogen bonding is only 3-4 kcal/mol (76). However, the large number of potential hydrogen bonds along the length of the fiber means interfiber bonding can be

quite strong. Factors that increase the fiber surface area (or the area of fiber contact), increase interfiber bonding. Such factors include refining, which increases surface area by fiber fibrillation, and hydration of fibers, which makes them more flexible to better mold around each other. The infamous Page equation, which models the tensile strength of paper in terms of a few basic fiber and paper properties, illustrates the relative effects of fiber strength and bond strength on paper strength (97). Four of the variables are fiber properties- the fiber length, fiber density, the ratio of cross sectional area to perimeter, and the fiber strength as measured by the zero-span tensile test, one is a paper property- its relative bonded area, and one is a property of fiber-to-fiber interaction- the shear strength per unit area of the adhesive bond. Qualitatively, the Page equation states that the strength of weakly bonded paper (having unrefined fibers for example) is controlled by factors associated with bonding strength, but for papers of progressively increasing strength (increased refining), fiber strength becomes of importance. In pulp which is overly refined the weak link often becomes the strength of the individual fibers.

2.8.2 Dry Strength Additives

2.8.2.1 Starch

Dry strength agents are added during papermaking to increase the dry strength of paper by enhancing interfiber bonding. Many water soluble, hydrogen bonding polymers can be used as dry strength additives. Starch derivatives, gums, and synthetic polymers are the three most common commercial dry strength agents with starch derivatives being used 95% of the time. Starch is a white granular substance that occurs widely in higher plants such as corn, wheat, tapioca, and potato and is chemically similar to cellulose, being a

polymer composed of glucopyranose units linked through carbons 1 and 4. As shown in Figures 25 and 26, starch is composed of a mixture of two polymers, an essentially linear polysaccharide -amylose, and a highly branched polysaccharide – amylopectin (9).

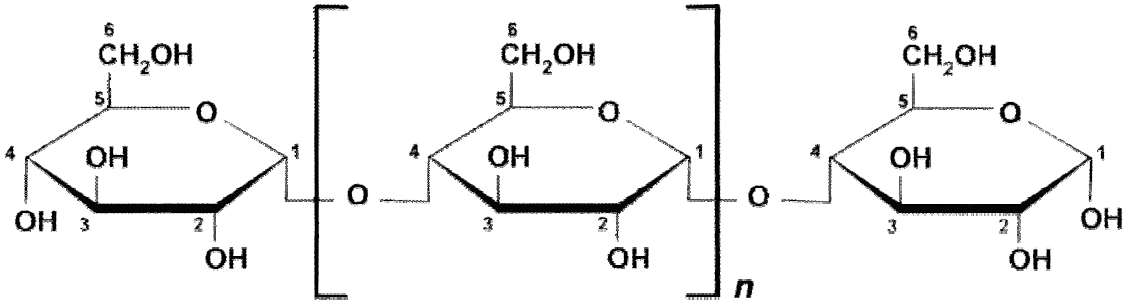

Figure 25: Molecular structure of the amylase component of starch.

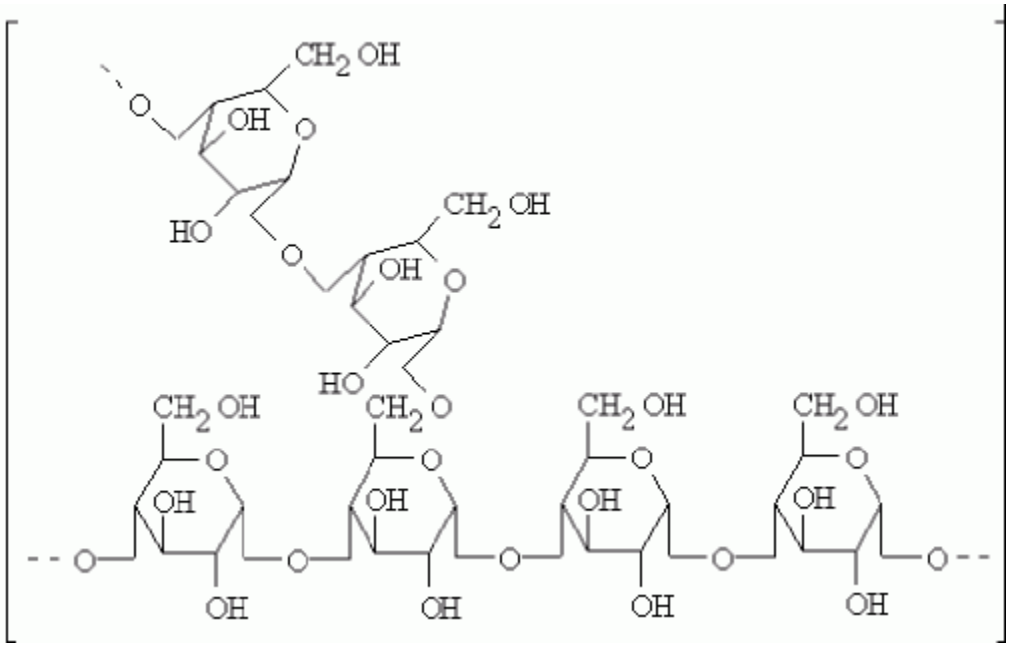

Figure 26: Molecular structure of amylopectin component of starch.

Starch is composed of tiny granules about 5-100 micron depending on origin and, for papermaking, these granules must be cooked to bring about either complete or partial

disruption. Starch is negatively charged and has little attraction to papermaking fibers and its retention is quite low (less than 40%). Thus, it must be cationized with either tertiary or quaternary amine groups, increasing the cost by at least $500/ton (3).

2.8.2.2 Polyacrylamides

Polyacrylamides, with general structure shown in Figure 27, are also used as dry strength additives. Polyacrylamide shown is nonionic and again has little attraction to papermaking fibers. Cationic polyacrylamides are produced by copolymerization with cationic monomers or by modifying some of the amide groups to cationic groups. Typically 10% of the monomers will be charged. Cationic polyacrylamides are completely ionized over the entire pH range of papermaking (9).

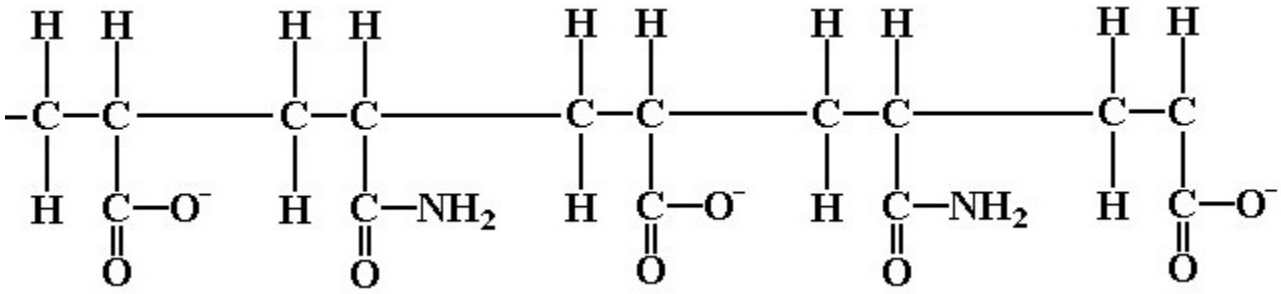

Figure 27: Chemical structure of polyacrylamide.

Dry strength additives are thought to act by several mechanisms. First, they enhance interfiber bonding as the free glucose hydroxyls (starch) or primary amide groups (polyacrylamides) participate in hydrogen bonding with fiber surface cellulose molecules and supplement the number of hydrogen bonds that would naturally occur in the bonded

area between two fibers. They also improve sheet formation which provides more uniformly distributed fiber-fiber bonds.

2.8.2.3 Hemicelluloses

Wood fibers contain their own natural dry strength additive in the form of hemicelluloses. I contrast to cellulose, hemicelluloses are linearly branched heteropolysaccharides composed of a variety of different sugars such as xylose, galactose, mannose, and arabinose and have lower molecular weights, usually containing fewer than 400 sugar units (76). It is well known that removing hemicelluloses from wood fibers makes it more difficult to develop their bonding characteristics. The presence of xylans on cellulose fiber surfaces has been shown to enhance the strength properties of the fiber network by increasing the bonding ability of the fibers. AFM imaging has show that xylan aggregates observed in solution through light scattering deposit onto a cellulose substrate as nodules. Xylans exist in the aqueous solution both as dissolved single molecules and as aggregated structures, but main form is aggregates. The aggregates diffuse to and adsorb onto the surface of fibers (98).

2.8.2.4 Wood fines

Wood fines can also increase the strength of paper. Fines are very short fibers, fiber fragments or ray cells that pass through a 200 mesh screen. Fines typically have five times the surface area of fibers per given unit weight and tend to swell and absorb more water than fibers (76). Thus they are conformable and can bond with fibers, thereby increasing strength. Fines increase sheet consolidation giving stronger, denser paper. Xu

and Pelton found that fines significantly increase the strength of highly loaded PCC filled papers (99). They hypothesize that fines fill the PCC induced voids, thereby acting as a gasket and increasing fiber-fiber contact area. However, fines are not optimal dry strength aids because their generation requires energy-intensive refining, they reduce drainage, and filling in too many voids will lower light scattering efficiency.

2.9 Filler Modifications to Increase Bondability

An active research area has developed to synthesize inorganic pigment composites with substantial amounts of material available to participate in hydrogen bonding with fibers, thus avoiding the paper strength reduction typically associated with fillers. Aho et al. synthesized cellulose-filler composites by precipitating inorganic pigments, such as calcium carbonate, onto fines in solution. The composites allowed a significant increase in filler loading without deteriorating paper strength (100). Kuboshima used acrylic acid or vinyl acetate to chemically bond hydrogen bond forming polymers to fillers (101). Gill used epichlorohydron and polyaminoamide or polyamine polymer to modify the filler surface to improve filler-fiber bonding (102). Another patent application presented polymers with phosphonated and sulfonated substituent groups and optional amide substituent groups to bond fillers and fibers together (103). However, although these modified fillers may enhance filled paper strength, their high cost makes them difficult to apply commercially (3). As an alternative, our group has developed several very low cost methods to strongly coat starch to the surface of clay and calcium carbonate fillers. These starch-inorganic composites give dramatic increases in paper strength over comparable

unmodified fillers at constant filler loading. As a first attempt, a clay slurry of 30-60% solids was simply mixed with cooked starch, vacuum dried and grinded (3). Handsheets containing 25 wt. % coated filler had the same tensile strength as those containing 15% unmodified filler made by adding cationic starch directly to pulp furnish. The coated clay had only 2.5 wt. % of starch, giving a starch of 1.47 nm which swells to 8.3 nm in water. This swollen layer is deformable and provides many hydrogen bonding groups on the filler surface that can bond strongly to wood fibers. The method differs from the traditional use of dissolved starch in that the latter gives only a molecular-level thickness of starch on the filler surface compared to a swollen starch gel. In addition, it is well known that adsorption of cationic starch on fibers will reach a saturation condition and further increase of adsorption amount beyond saturation level is impossible. So amount of starch on wood is limited, unlike with this method. This method was also used to coat precipitated calcium carbonate filler, giving significant increases in physical properties including tensile, tearing, and folding over addition of fully cooked starch (4). However, disadvantages of this method include energy intensive processing steps and the loss of around 15% of the starch by dissolution. This dissolved starch is negatively charged and will not be retained by the sheet. Thus it will likely accumulate in the white water, leading to pitch, slime, and stickies problems.

To maximize starch coating efficiency and reduce the potential for papermaking problems due to excess starch, another method was developed to precipitate insoluble starch on the filler surface using ammonium sulfate (104). This method gives starch coated clay with relatively large size and a fibril shape so that the particles are easily

entrapped by the fiber network to give a high total retention. Most importantly, paper strength increased more than 100% for the starch-modified clay compared to untreated clay at 20-30% clay loading. Optical properties like opacity at a given paper strength were also improved. Water solubility of the precipitated starch was less than 3% at 50 °C and, compared to previous approaches, a relatively larger starch ratio in the composite could be obtained (up to 1:1), leading to higher bonding. The principle disadvantage of this method is the tedious washing step required to remove free salt.

Finally, an even easier, lower cost method for coating starch on fillers was developed by precipitating starch via the formation of water-insoluble, starch-fatty acid complexes (105). It is believed that unbranched polar compounds (i.e. fatty acids and their monoglycerides) form helical inclusion complexes with amylase under suitable conditions. The soluble starch amount for these composites was found to be less than 0.3% under papermaking conditions. This composite increased paper strength by about 200% compared to untreated clay combined with 0.05-0.1 wt % cpam based on dry fiber weight. It was also found that the fiber-starch bonding strength for these composites is actually greater than fiber-fiber bonding strength. In addition, the presence of fatty acids increased the water-repellency of the paper.

2.10 Regenerated Cellulose

Another potential polysaccharide material to be used in inorganic pigment composites with high bondability is regenerated cellulose. Production of regenerated cellulose products represents the largest market for the chemical processing of cellulose, beyond

pulp and paper (106). Such regenerated cellulose products include fibers, films, membranes, beads and sponges. While cellulose can dissolve to a certain extent in several solvent systems, which include heavy metal-amine complex solutions, concentrated metal salts, cold NaOH solutions, thiocyanate/amine, LiCl/dimethylacetamide, N-methylmorpholine-N-oxide (NMMO) monohydrate, and concentrated H_2SO_4 and H_3PO_4, most of these solvent systems are industrially impractical (107). However, the NMMO monohydrate system has been used for several decades to commercially manufacture regenerated cellulose materials. Advantages of NMMO-based cellulose processing, known as the Lyocell method, include relative simplicity and small environmental footprint as the solvent is non-toxic, biodegradable, and almost completely recycled during the process (108). The structure of NMMO is shown in Figure 28.

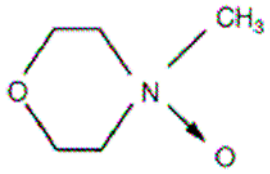

Figure 28: Chemical structure of NMMO.

N-methylmorpholine-N-oxide (NMMO) monohydrate has a water content of 13.3% by mass. With its strong N-O dipole, NMMO monohydrate solvent can dissolve cellulose without prior activation or derivitization. Solutions with a cellulose content of up to about 23% are produced by dispersing cellulose fiber in aqueous NMMO (typically 50 wt. -%).

The suspension is then concentrated at temperatures between 80 and 120 °C until the water content is reduced such that NMMO monohydrate is formed and the cellulose dissolves. The resulting viscoelastic solution can then be cast or spun to a desired shape and transformed into regenerated cellulose in a precipitation batch containing a non-solvent such as water and/or alcohol. Figure 29 shows the ternary phase diagram for the cellulose/NMMO/water system during the process of dissolution, regeneration, and drying of cellulose (106-108).

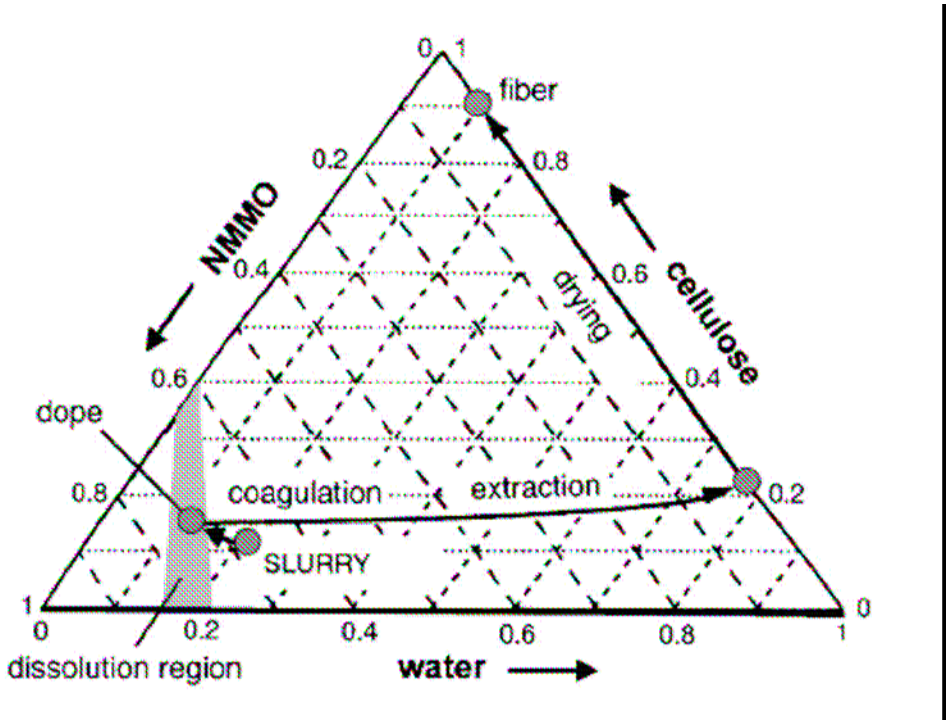

Figure 29: Phase diagram for synthesis of regenerated cellulose from cellulose/NMMO/water system (Fink et al. 2001).

The process occurring on the molecular level during dissolution of cellulose in NMMO remain largely unknown. While the swelling and dissolution of cellulose must caused by

breakage of intramolecular and intermolecular H-bonds in cellulose and between NMMO and water accompanied by the formation of new H-bonds between solvent and cellulose, the processes are extremely complex and no individual steps have been mechanistically identified thus far (108). The regeneration of cellulose from the NMMO monohydrate system converts cellulose from the cellulose I structure of the cellulose precursor to cellulose II (107). As shown in Table 4 below, the regenerated cellulose has a significantly lower degree of crystallinity than the original cellulose powder (106).

Table 4: Degree of crystallinity and crystallite size of native and regenerated cellulose (Klemm et al. 2005)

	Degree of Crystallinity (%)	Crystallite Size (nm)		
		$D_{(110)}$	$D_{(110)}$	$D_{(020)}$
Bacterial cellulose	65-79	5.3	6.5	5.7
Cotton linters	56-65	4.7	5.4	6.0
Pulp	43-56			4.1-4.7
Regenerated cellulose (Lyocell process)	35	4.4	3.3	17.5

The solution structure of cellulose dissolved in NMMO, under very dilute conditions (0.2 -3 wt. %), has been studied using static laser light scattering. The weight-average molecular masses obtained are many times higher than those calculated from the corresponding cuoxam degree of polymerizations. It is well known that cellulose is

molecularly dispersed in cuoxam at sufficiently low concentrations. In addition, single cellulose molecules could not be detected. Thus, aggregation of cellulose chains must be occurring. Additionally, a bimodal aggregate size distribution was found with the larger size having a radius of gyration, R_g, of 194 nm and the smaller size having R_g = 75 nm (109). The aggregation of polysaccharides such as cellulose, cellulose derivatives and hemicelluloses in solution is a commonly encountered phenomenon and is proposed to result from interactions through hydrogen bonds between linear portions of the polysaccharide chains. From light scattering experiments, Schultz identified the cellulose aggregates in NMMO as covalently bonded macromolecules, equivalent to worm like objects illustrated by the fringed micelle model shown in Figure 30a (110). Later Schultz suggested that the bimodal size distribution of cellulose aggregates in NMMO does not result from two separate large and small populations, but that the smaller component corresponds to dangling chains from the larger aggregate as shown in Figure 30b (111).

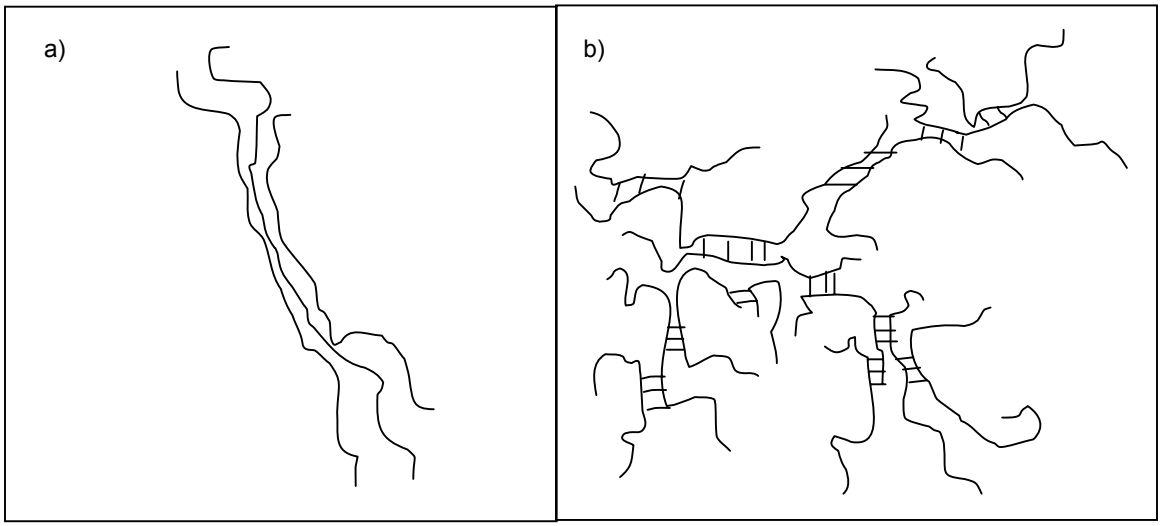

Figure 30: Illustration of cellulose aggregates dissolved in as characterized by (a) the simple fringed micelle model and (b) large aggregate model with dangling chains (adapted from Schultz et al. 2000)

Roder et al. and Fink et al. assume the smaller aggregate population corresponds to cellulose crystallites that are not completely disintegrated by the dissolution process since the size of this component is not effected by pre-treatment with a swelling agent such as NaOH (109, 112). The larger particles found in the cellulose solutions that can be influenced by the activation step could therefore stem form microfibrils (or aggregates of microfibrillar ribbons).

CHAPTER 3

PROBLEM ANALYSIS AND OBJECTIVES

3.1 Problem Statement

Of all papermaking pigments, titanium dioxide has the highest brightness, opacifying power, and cost. While papermakers have traditionally used much cheaper fillers than TiO_2 to achieve brightness and opacity, there are many grades that require TiO_2 to reach stringent opacity targets. In addition, several papermaking trends necessitate more use of TiO_2 including reduction in basis weight and the increasing use of cheap, discolored fibers. Also, because TiO_2 is used in a large variety of consumer and commodity products, its global demand growth is increasing rapidly. This fact, coupled with titanium raw material supply constraints, has lead to increasing prices for an already exceptionally expensive pigment. The introduction of novel, even more efficient light scattering TiO_2-based pigments can help manufactures limit costs while maintaining the required optical properties of their product. One approach to increasing the efficiency of TiO_2 is to create unique pigment morphologies designed to scatter light more effectively than conventional TiO_2 pigments. The achievement of this goal requires quantitatively identifying and controlling the factors which impact the light-scattering efficiency of TiO_2. Debate exists within the literature regarding the effects of TiO_2 particle morphology on light scattering efficiency. For instance, historically the pigment industry has assumed that aggregates of titania particles, regardless of aggregate size, arrangement, and crystal composition, will offer less opacifying power than optimally sized single crystal particles. However, recent

theoretical modeling attempts show the light scattering of small TiO_2 aggregates to be more efficient. In addition, disagreement exists about the light scattering efficiency of titania core-shell and hollow particles.

Finally, a well known disadvantage of adding fillers like TiO_2 to paper is the reduction of interfiber bonding, and therefore paper strength. From a papermaking perspective, it is necessary to develop novel TiO_2 pigments with enhanced opacifying power and bondability.

3.2 Problem analysis

The goal of this thesis is to a) study the relationship between light scattering efficiency and TiO_2 particle crystal structure for several TiO_2 morphologies including polycrystalline aggregates, core-shell and hollow particles and to b) determine the effect of encapsulation of inorganic fillers by natural polymers on bondabilty with cellulose fibers. There are several separate problems that must be analyzed in order to fulfill this multifaceted goal.

Problem #1

Understanding of the factors which impact the light-scattering efficiency of TiO_2 pigments is primarily limited to the effects of single crystal particle size and particle size distribution on light scattering efficiency. The degree of particle agglomeration and particle crowding are also known to affect the light scattering efficiency of TiO_2 through

near-field optical interactions between neighboring particles but this phenomenon is not fully understood. In addition, debate over the scattering performance of small well-dispersed titania aggregates exists in the literature with conflicting results being presented. From these numerical modeling based reports, it is obvious that the results depend on cluster configuration and primary particle size, location of the aggregate with respect to the angle of incidence of light, and the optical constants used. No experimental results addressing this problem have been published to date.

Problem #2

Hollow synthetic plastic pigments and polycrystalline calcium carbonate have been synthesized and shown experimentally to have better or equal opacifying power in papermaking application than their solid counterparts. However, debate exists over the light scattering performance of hollow and core-shell TiO_2 particles. Experimental results show titania core-shell particles with an overall diameter of ~ 1.0 μm and a shell thickness of 50 nm to provide opacity equal to that provided by a commercial TiO_2 pigment in cellulose. However, theoretical results based on Mie light scattering theory show hollow and core-shell titania particles to have significantly less opacifying power than conventional TiO_2.

Problem #3

Recently, both single crystal and polycrystalline titania nanostructures with different shapes, such as bullet, diamond, short and long rods, branched rods, and ellipsoids have been synthesized. From templating methods like sol-gel and layer-by-layer assembly,

hollow polycrystalline titania structures have been made with shapes limited to the sphere, ellipsoid, and tube. It is widely believed that the shape and void size of the hollow particles is exactly determined by the nanosized template for both sol-gel and LBL. Thus, synthesis of unique or complex titania nanoparticle morphologies through such templating methods is severally limited by the current availability of uniform colloidal templates with elementary geometries.

Problem #4

An active research area has developed to synthesize organic/inorganic composites capable of forming high strength bonds with wood fibers. The most promising composites to date combine traditional papermaking fillers and renewable carbohydrate materials, such as starch and wood fines, that can form strong hydrogen bonds with fibers. These composites give dramatic improvements in paper strength over comparable unmodified fillers at constant filler loading. However, the particle size, size distribution and shape of these composite filler particles cannot be well controlled, which hinders fundamental understanding of core-shell functional fillers and their practical industrial applications.

3.3 Hypotheses

Problem #1

Polycrystalline TiO_2 particles can be synthesized with controllable shape and crystal microstructure. These discrete crystallite aggregates can scatter light more effectively in a

cellulose matrix than a commercial rutile pigment which is composed primarily of single crystals and crystal twins. The light scattering capability of such aggregates is primarily affected by crystallite phase, size, and orientation.

Problem #2

Core-shell and hollow polycrystalline TiO_2 particles can be synthesized with controllable cavity size, shell thickness, and crystal microstructure. The polycrystalline hollow particles can scatter light more effectively in a cellulose matrix than a commercial rutile pigment. The light scattering capability of the hollow particles depends on core size, and crystal structure, while the light scattering efficiency of titania core-shell particles depends on the core size and crystal structure of both the titania shell and the core.

Problem #3

The shape of titania nanoparticles synthesized via conventional templating methods is not always limited to the shape of the colloidal template. The overall particle shape and cavity shape can be controlled simultaneously by choosing an appropriate template and coating thickness.

Problem #4

Inorganic-cellulose core-shell and hollow cellulose nanoparticles can be synthesized by self-encapsulation with regenerated cellulose. The regenerated cellulose shell is capable of forming hydrogen bonds with wood fibers and can provide more paper strength than

untreated inorganic pigments. The bonding ability of natural polysaccharide polymers with wood fibers depends on the crystallinity of the polymer.

3.4 Objectives

The objectives of this thesis were to:

- Develop a sensitive and reproducible method to experimentally measure the effects of polycrystalline TiO_2 particle composition and morphology on opacity of a cellulose film.
- Use the latest advances in numerical modeling of light scattering from individual and aggregate particles to theoretically determine the effects of polycrystalline TiO_2 particle composition and morphology on opacity of a cellulose film.
- Synthesize polycrystalline TiO_2 nanoparticles with controllable shape, phase composition, and crystal structure, experimentally and theoretically determine the influence of these properties on light scattering efficiency, and compare their light scattering efficiency with commercial TiO_2 pigments.
- Synthesize core-shell and hollow polycrystalline TiO_2 particles with controllable cavity size, shell thickness, phase composition, and crystal structure, experimentally and theoretically determine the influence of these properties on light scattering efficiency, and compare their light scattering efficiency with commercial TiO_2 pigments.
- Synthesize hollow polycrystalline TiO_2 nanoparticles via conventional templating methods and study the dependence of particle morphology on layer thickness

- Develop a simple method to encapsulate individual inorganic pigment particle with high bonding affinity for wood fibers.
- Quantify bonding affinity of regenerated cellulose shell for wood fibers and compare this affinity with that of other potential high bonding coating materials like starch and cellulose whiskers.

CHAPTER 4

ENHANCED LIGHT SCATTERING FROM POLYCRYSTALLINE TiO_2 PARTICLES IN A CELLULOSE MATRIX

Abstract

The opacifying power of synthesized polycrystalline TiO_2 particles in a cellulose matrix was found experimentally and theoretically to be superior to that of a commercial rutile pigment, depending on crystal structure of the synthesized particles. The crystal structure of the particles was varied by calcination of amorphous titania nanoparticles at different temperatures and was characterized using SEM, TEM, and XRD. Polycrystalline anatase pigments had less opacifying power than commercial rutile, while polycrystalline pigments containing a one-to-one mixture of anatase and rutile had similar opacifying power as the commercial pigment. High aspect ratio polycrystalline rutile pigments composed of a linear linkage of several individual rutile crystals gave 6% more opacity than the commercial rutile pigment. Theoretical light scattering calculations using the T-Matrix Method showed the light scattering efficiency of linearly arranged polycrystalline rutile particles to depend on number and size of crystals composing the particle and confirmed the higher efficiency of the synthesized polycrystalline rutile pigments over commercial rutile as a result of the optimal size of the primary crystals composing the particles. It is suggested that the efficiency of rutile pigments can be increased dramatically by controlling the primary crystal size rather than the overall particle size, as currently practiced by industry. It is believed that the greater than expected light scattering efficiency of the biphasic pigment results from reflection and refraction of light

at the grain boundaries between crystals of different phase, which have different refractive indices.

Introduction

A fundamental understanding of the scattering of light by small particles in a continuous matrix is of considerable importance to many industrial and scientific fields including paints, coatings, papermaking, dye-sensitized solar cells, climatology, astrophysics, and environmental science (1-3). This scattering is determined not only by the composition of the incident light and the optical properties of the particles and the medium but also by the size, shape, concentration, surface roughness, spatial arrangement of the particles, etc. Characterization of the scattering of light by titanium dioxide particles has been the subject of significant research for many decades, as TiO_2's many technological applications often depend on its high light scattering efficiency. Because of its exceptionally high refractive index and whiteness, titanium dioxide is used to impart opacity to a wide variety of products including coatings, paints, plastics, paper, rubber printing inks, synthetic fibers, ceramics, cosmetics, and even toothpaste (4). New high performance TiO_2 products are necessary to help manufactures limit costs while maintaining the required optical properties of their product. One approach to increase the efficiency of TiO_2 is to create novel TiO_2 based pigment structures designed to scatter light even more effectively than conventional TiO_2 pigments. The achievement of this goal requires quantitatively identifying and controlling the factors which impact the light-scattering efficiency of TiO_2. The effect of the size and particle size distribution of single

crystal particles on light scattering efficiency has been well studied. The degree of particle agglomeration and particle crowding are also known to effect the light scattering efficiency of TiO_2 through near-field optical interactions between neighboring particles (1, 5-10). While a decrease in opacity of paint films upon particle flocculation and upon increase in the particle volume concentration of the pigment above a certain level is readily observable, the mechanism responsible for this loss in light scattering is debatable (11). Thus, it is known that large floccules of TiO_2 particles scatter less light than well dispersed TiO_2 particles (6). However, it is not conclusively known how the light scattering efficiency of small, well-dispersed aggregates composed of multiple TiO_2 particles or crystals compares with that of single, optimally sized TiO_2 particles. Due to the difficulty of investigating this particular problem experimentally, only theoretical, numerical modeling attempts to explain the light scattering efficiency of such TiO_2 aggregates have been published to date. Unfortunately this collection of reports seem to complicate the issue as a variety of opposing results are presented with several authors stating that the light scattering of small TiO_2 aggregates is superior to that of an isolated TiO_2 particle (1, 7), while several authors provide the opposite conclusion (5, 9, 12).

This paper presents experimental and theoretical analysis of the light scattering phenomena of polycrystalline aggregates of TiO_2 in an optically uniform, transparent, pore free cellulose nanowhisker matrix. The effects of phase composition, crystallite size, and crystallite arrangement on the opacifying power of synthesized pigments are investigated and compared with a commercial rutile pigment.

Experimental

Materials

Cotton pulp (Procter & Gamble Cellulose) and rutile titanium dioxide (Tiona RCS-P, Millennium Chemicals) were donated and used as received. Sulfuric acid (96.5%, EM Science), poly(acrylic acid, sodium salt) (PAA, MW 5,100, Aldrich), polyethylene glycol (PEG, MW = 8,000, Aldrich), titanium(IV) ethoxide (90%, Strem Chemicals), potassium chloride (KCl, J.T. Baker), ethanol (anhydrous, VWR) were used without further purification. Water was obtained from a Nanopure ultrapure water system with a resistivity of about 18 MΩ cm.

Preparation

Monodisperse, spherical amorphous titania nanoparticles with an average diameter of 288 nm (from light scattering) were synthesized according the procedure presented by Jiang *et. al* (13). Typically, 100 mL of ethanol were first mixed with 0.4 mL of 0.1 M aqueous KCl. Titanium tetraethoxide (1.7 mL, 90 wt.-%) was then added at room temperature under mechanical stirring and a N_2 purge. The stirring was discontinued after 10 minutes. The solution was then allowed to sit for two hours. The resulting solids were isolated by three centrifugation and ethanol washing cycles at 25,900 RCF (Relative Centrifugal Force) for 2.5 min and vacuum dried at around 60 °C. To obtain polycrystalline titania particles with varying phase composition and crystallite size, this amorphous titania powder was calcined separately at 600 °C, 800 °C, and 1000 °C. Prior to calcination the titania particles were mixed with dispersed cellulose particles in water with a ratio of 1 to 5 to prevent interparticle sintering, as illustrated in Figure 31. The dispersion was then sonicated (Heat Systems-Ultrasonics W-385 probe sonicator) for about 5 minutes. The

mixture was dried under vacuum at 120 °C and then calcined at different temperatures for 1.5 hours. The cellulose powder was prepared by grinding hardened, ashless filter paper (Whatman, 541) in a Wiley Mill (Arthur H. Thomas Co.) to pass through a 1 mm mesh. This specialty filter paper was used because of its extremely low inorganic ash content (0.017%).

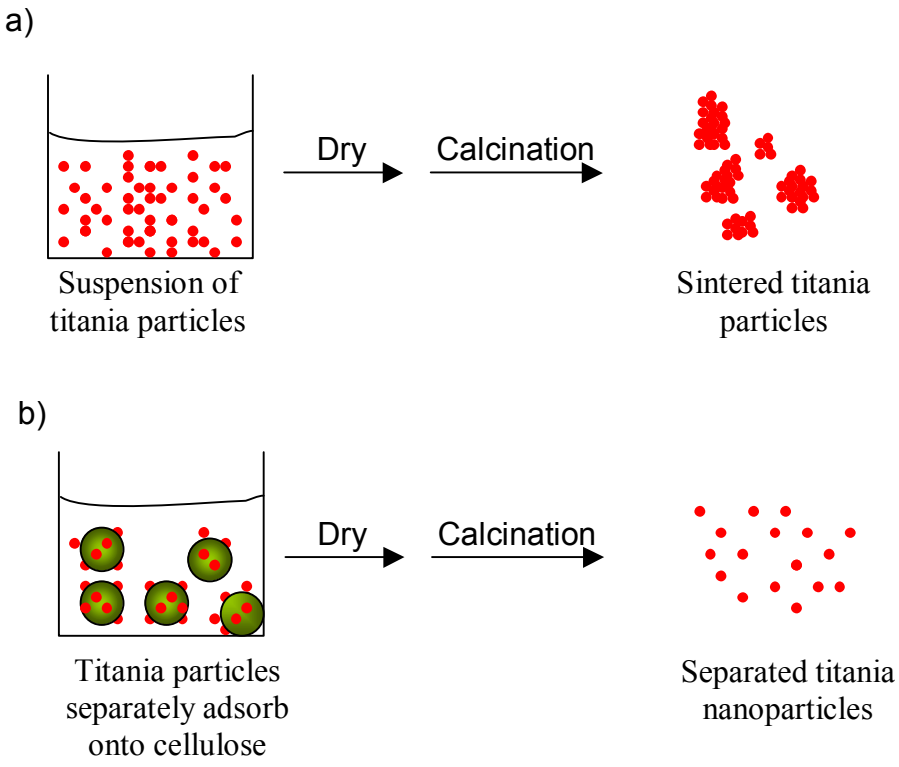

Figure 31: Illustration of (a) titania nanoparticle sintering during traditional calcination and (b) formation of discrete titania nanoparticles during calcination using the cellulose matrix method.

In order to compare the opacifying power of the synthesized nanoparticles with commercial rutile titania, the powders were distributed throughout a thin cellulose film. In a typical experiment, 0.04 g of powder were dispersed in approximately 10 mL of

water along with 0.004 g of PAA dispersant and sonicated for 10 minutes. The solutions were then allowed to rest for about 2 minutes. During this time, oversized particles that could not be dispersed into primary particles during sonication, either because of agglomeration or sintering during calcination, quickly settle to the bottom while fully dispersed primary particles remain in the supernatant. The supernatant was then removed from the settled solids and the settled solids were dried under vacuum and weighed. The supernatant was also weighed such that the exact concentration of the solution could be determined.

Cellulose films with a known volume concentration of uniformly distributed titania particles where then obtained by combining the well-dispersed filler suspension prepared above with PEG (whose role will be discussed below) and a gel-like solution of cellulose whiskers. This gel-like mixture was allowed to dry on a transparency within a 1.25 x 1.25 inch area framed by Scotch tape. For the typical film with a titania concentration of 1 vol.%, 3.9105 g of cellulose whiskers solution (8.27 wt. %) was combined with 0.1386 g of PEG, and the filler suspension containing 0.01429 g titania. This mixture was then pipetted onto four separate 1.25 X 1.25 inch area films.

The cellulose nanowhiskers were prepared as outlined previously (14). Cotton fiber was hydrolyzed with 64 wt. % sulfuric acid at 45 °C for 45 minutes. Prior to hydrolysis, the dry cotton fiber sheets were torn into small pieces and fed through a Wiley mill to pass through a 1 mm mesh. Typically, 40 g ground cotton was treated with 700 mL sulfuric acid solution. Immediately following hydrolysis, the unhydrolyzed cellulose whiskers

was diluted 10-fold with water. The solids were allowed to settle overnight and then collected with minimal amounts of solution. Excess acid was removed by three washing and centrifugation (25,900 RCF for 30 min.) cycles followed by dialysis (Spectra/Por membrane, MWCO 50K) against water for several days until the water achieved a neutral pH. The cellulose whisker suspension was then sonicated for 35 min while cooling in an ice bath. The resulting suspension was allowed to stand over a mixed bed resin (Sigma, TMD-8) for 48 h and then filtered through hardened ashless filter paper (Whatman, 541) and concentrated to 8.27% using a rotary evaporator under vacuum.

Characterization

Transmission electron microscopy (TEM) was performed using a Hitachi HF-2000 Field Emission Gun (FEG) microscope at 200kV. X-ray diffraction (XRD) was carried out using an X'Pert Pro Alpha-1 diffractometer with an incident beam monochrometer allowing only the $K\alpha_1$ component of Cu radiation. XRD spectra were analyzed using JADE 7 software from Materials Data. It is well known that the width of a peak in a diffraction pattern results from instrument optics and crystallite microstrain and size. Using the JADE software, the effect of instrumental broadening was removed by calibration with the standard LaB_6 (NIST, 660 SRM) and crystallite strain was calculated to be zero. Thus, crystallite size was calculated from peak broadening using classical Williamson-Hall plots (15). The plots were constructed for all non-overlapping anatase and rutile peaks occurring for two theta values between 20° and 80°. The phase composition of the synthesized powder containing both anatase and rutile titania was determined by constructing a calibration curve based on the XRD peak intensities of standards containing known ratios of anatase and rutile. In this method, diffraction

patterns are obtained for each standard and the intensity ratio of the predominate peak for anatase (2θ ~ 25.3°) and rutile (2θ ~ 27.5°) is calculated. This data was used to construct the calibration curve shown in Figure 32. From this curve, the quantitative amount of each phase can be determined for an unknown sample from the intensity ratio $I_{rutile\ @\ 2\theta=27.5°}/I_{anatase\ @\ 2\theta=25.3°}$.

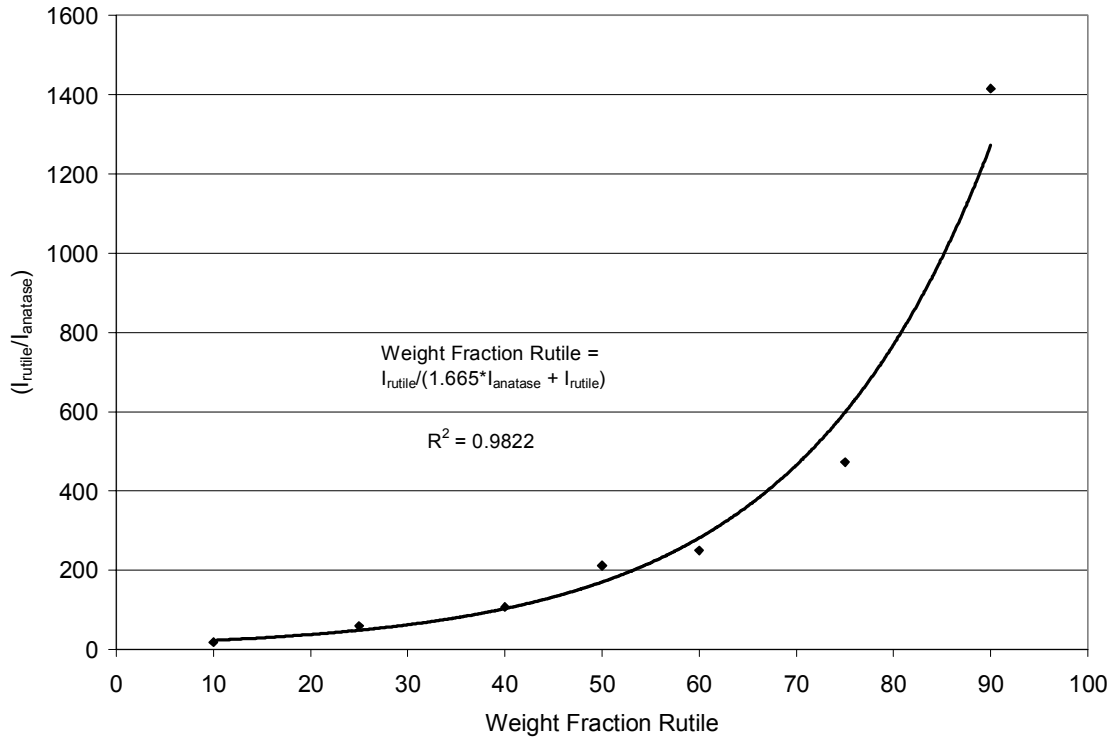

Figure 32: Calibration curve to determine weight fraction of rutile in an anatase/rutile bi-phasic powder sample from XRD analysis.

Pigment particle size distributions were obtained with a Malvern 3000 Zetasizer. The Zetasizer was also used to obtain average particle size for the nearly spherical 600 °C and 800 °C particles, while electron micrographs were used to obtain particle size for the high aspect ratio commercial rutile and 1000 °C particles. The width of the particle size

distribution, or geometric size distribution, GSD, was calculated from the particle size distributions shown in Figure 33 using the equation

$$GSD = (d_{84}/d_{16})^{0.5}$$

Equation 16: Geometric Size Distribution

where d_{84} = diameter for 84% finer, and d_{16} = diameter for 16% finer. The TAPPI opacity of the titania filled cellulose films was measured using a Technidyne BNL-3 Opacimeter with a quartz-tungsten-halogen lamp filtered for illumination at 572 nm. Film thickness was measured using a hard caliper instrument (AB Lorentzen & Wettre).

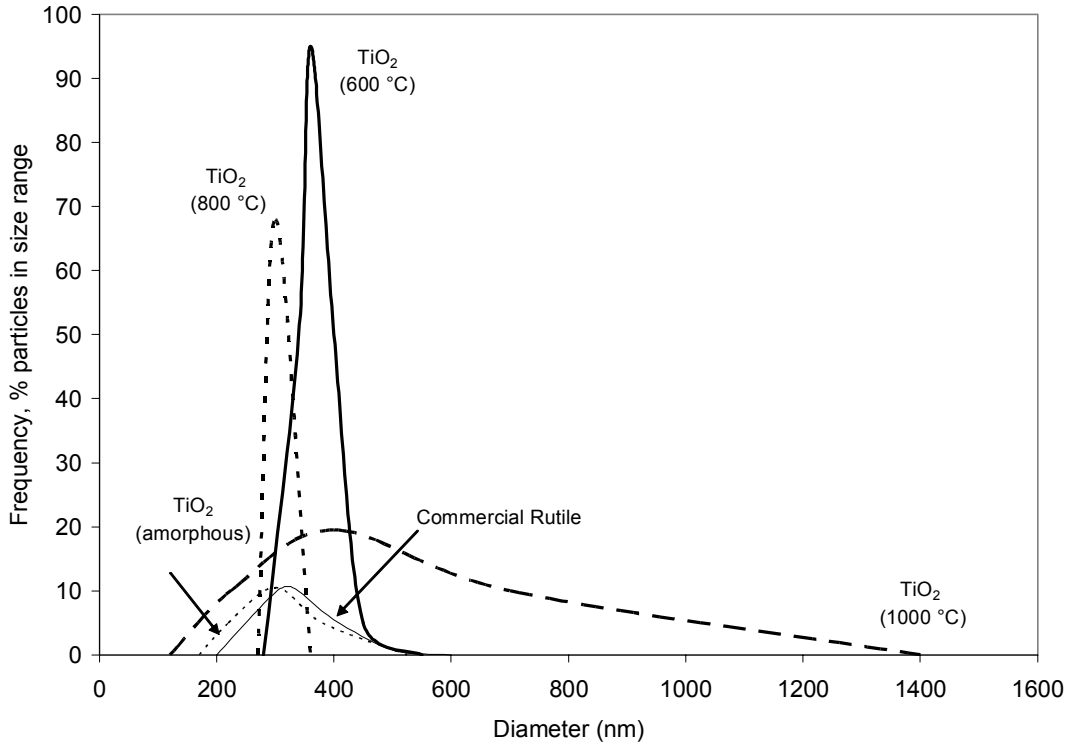

Figure 33: Particle size distribution of synthesized and commercial TiO_2 obtained from light scattering.

The theoretical light scattering efficiencies of single crystal rutile and linearly arranged polycrystalline rutile clusters were numerically calculated using the superposition T-matrix method developed by Mackowski and Mishchenko (16). This method is capable of determining the exact, theoretical light scattering for i) a single, isolated spherical particle, in accordance with Mie theory and ii) a cluster composed of multiple spheres, where the light scattering from the individual spheres making up the cluster is affected by optical interactions with the neighboring spheres, a phenomenon called dependant scattering. The corresponding computer code, SCSMTM1.FOR, is publicly available at http://www.giss.nasa.gov/~crmim/t_matrix.html. The user of the code defines the light scattering problem by setting the wavelength of incident light, the refractive index of the medium, and the refractive index, size, and location in the Cartesian coordinate system of each individual sphere in the cluster. A detailed description of the T-Matrix Method and underlying theory can be found in the literature (16-18).

The magnitude of light theoretically scattered by small particles is defined in terms of scattering cross section, C_{sca}, which is the cross-sectional area over-which light interacts with a particle. When the wavelength of light is similar to the particle diameter, this cross-sectional area is larger than the geometric cross section of the particle. Light scattering efficiency is defined by normalizing the scattering cross section in terms of particle size. For pigment applications, light scattering efficiency is normalized on a particle volume basis since pigment formulations and cost depend on volume (19). Also, in practical pigment applications, incident light that has been scatter by a particle is then rescattered upon contact with several different pigments in the system. Thus the light

scattering power, or opacifying power, of a pigment in the system depends on the direction in which the light is scattered, since this determines how many times the light will be rescattered by contact with other pigments. The light scattering parameter, σ, accounts for the variation of scattered light with scattering angle such that

$$\sigma = \frac{C_{SCA}}{4/3\pi r^3} \bullet \left(1 - \overline{\cos\theta}\right)$$

Equation 17: Light scattering parameter in terms of $\sigma = \overline{\cos\theta}$

where C_{SCA} is the scattering cross-section of the pigment and $\overline{\cos\theta}$ is the average cosine of the scattering angle, weighted by the intensity of the scattered light as a function of angle (19). For pigments composed of a single, spherical crystal, r is the radius of the crystal. For pigments composed of multiple spherical crystals, r is the volume mean radius, r_{vm}, defined as

$$r_{vm} = \left(\frac{3V_{tot}}{4\pi}\right)^{1/3}$$

Equation 18: Volume mean radius for a cluster of spheres

where V_{tot} is the sum of the volumes for each crystal in the cluster.

Results and Discussion

The light scattering power of TiO_2 in pigment applications depends on several well documented factors. The dominating factors are particle size, particle size distribution, the severity of particle agglomeration, the refractive index of the medium in which the pigment is dispersed, pigment concentration, and the wavelength of incident light (20). In addition, the opacity of the matrix in which the pigment is dispersed also depends on the surface roughness of the film and the presence of air pockets, or pores, within the film (10). In order to experimentally evaluate the effects of pigment composition and morphology on TiO_2 opacifying power, great care must be taken to fix these variables. A cellulose matrix was chosen to evaluate the light scattering performance of synthesized TiO_2 particles for two reasons: 1) papermaking represents an important technological application of TiO_2 and 2) there is an established debate in the literature on the relationship between morphology and TiO_2 opacifying power in a cellulose matrix (19, 21). In this study, cellulose whiskers were used as the matrix because they easily form a uniform, transparent cellulose film upon casting and drying. In addition, the cellulose whiskers are discrete rod-shaped nanomaterials, with dimensions of 8 x (100-300) nm, whose size allows even distribution, or spacing, of the TiO_2 particles. Larger cellulose particles, like fibers or Avicel cellulose, may not allow even distribution of the particles throughout the matrix and may force the particles into crowded regions (22). To remove the potential effect of small pores on the scattering of light within the film, low molecular weight polyethylene glycol, with an index of refraction (1.47) which closely matches cellulose (1.53), was added to the aqueous solution of whiskers and pigment prior to casting the film. PEG remains a liquid at room temperature and can effectively fill

possible small pores in the film. When the TiO_2 filled cellulose/PEG films were removed from the transparency upon which they were dried, the surface in contact with the transparency was very smooth and uniform. For all films, this surface was placed in contact with the fixed wavelength (572 nm) light source during opacity measurements. Figure 3 shows the effect of monodisperse, single crystal rutile particle size on light scattering coefficient, σ, in a cellulose film irradiated at 572 nm as determined using the well-known T-Matrix method (16). The T-matrix numerical method is one of the most versatile, numerically accurate and popular theoretical techniques for rigorously computing the light scattering by single and compounded particles (23). A shown in Figure 34, optimum light scattering efficiency is obtained for single rutile particles with a diameter around 300 nm. Pigment manufacturers provide a rutile powder with an average particle size close to this optimum by controlling crystal growth, extensive milling of particle aggregates, and size classification. The commercial rutile pigment used in this study has an average particle size of 336 nm.

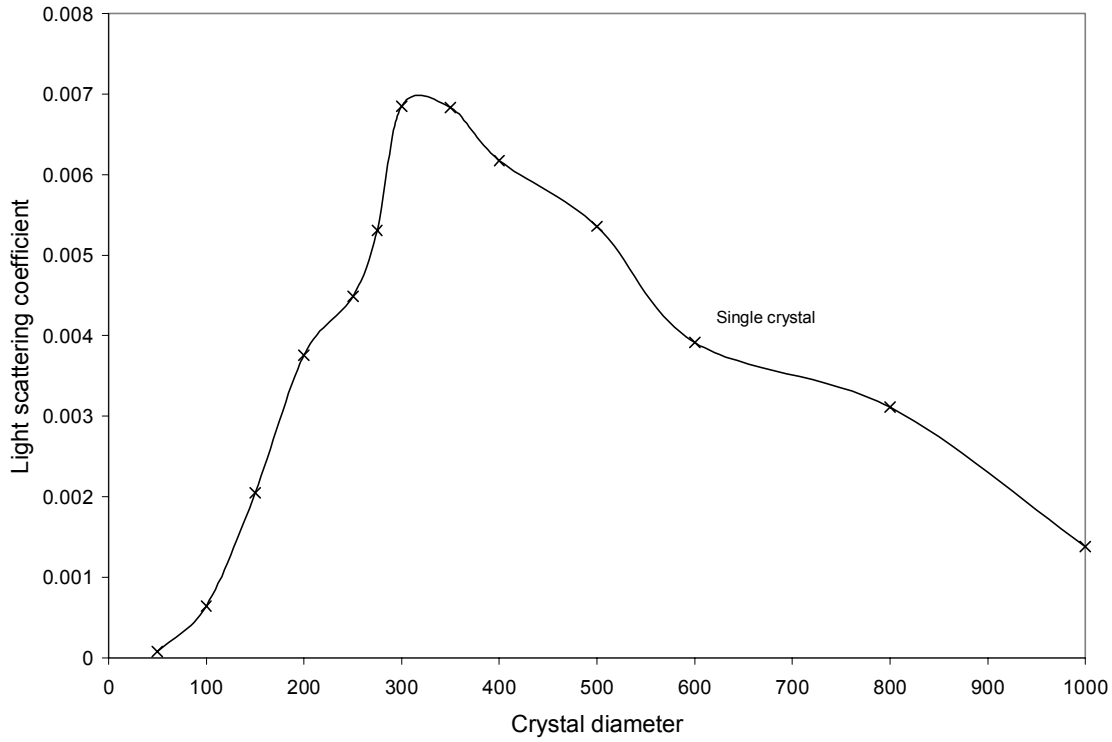

Figure 34: Theoretical dependence of single crystal rutile light scattering coefficient on particle size when embedded in a cellulose matrix and irradiated at 572 nm

Using this information as a starting point, monodisperse amorphous titania nanoparticles with a diameter of 288 nm (close to the optimum) were synthesized as shown in Figure 4(a). These amorphous templates were then heat treated to obtain polycrystalline TiO_2 particles with different morphologies and compositions. It is well known that TiO_2 pigments with a broad size distribution centered around the optimal size have less opacifying power than a corresponding monodisperse distribution (6). Pigment manufactures report the width of the particle size distribution as geometric size distribution, GSD. Typically, as GSD increases for a given pigment, opacifying power decreases. Figure 2 shows the particle size distributions of the synthesized and

commercial rutile TiO_2 particles. The widths of distribution are similar for all of the particles except the sample calcined at 1000 °C. Figure 35 shows that even though this sample has a much larger GSD than the other particles, its opacifying power is greatest.

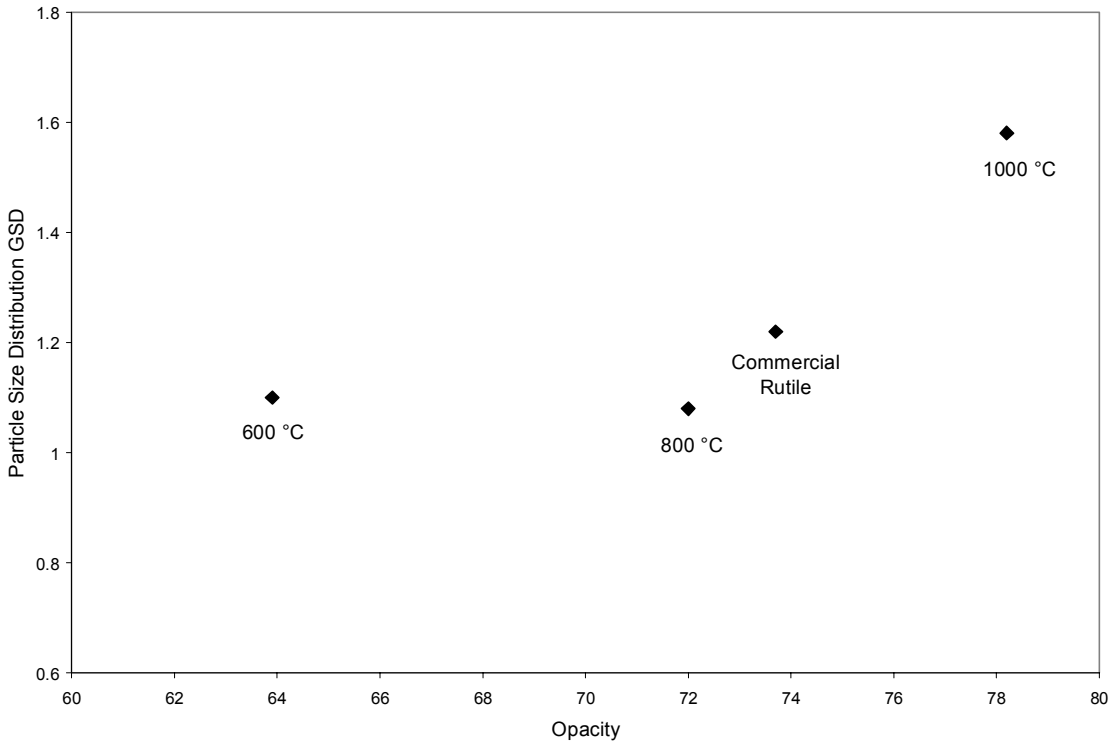

Figure 35: Opacity vs. particle size distribution for the synthesized and commercial rutile powders. Although the 1000 °C TiO_2 powder has a broader particle size distribution, it gives much higher opacity than commercial rutile.

In this study, the pigment volume concentration in the cellulose film was limited to 1% to eliminate the effects of dependent scattering between individual pigment particles. Dependent scattering is negligible only in dilute pigment dispersions not exceeding concentrations of ~5% by volume (5). Finally, several steps, such as addition of dispersant, sonication, and removal of large, undispersable aggregates, were taken in

attempts to prevent particle agglomeration within the cellulose films. In addition, the viscous, gel structure of the TiO_2/cellulose/PEG mixture helped ensure a stable, even distribution of the particles during drying of the film. The measured opacity of the films was shown to have excellent reproducibility indicating that reproducible levels of dispersion were achieved.

The phase composition and crystallite size of the amorphous titania nanoparticles are dependant upon the calcination temperature. The XRD spectra in Figure 36 show that calcination at 600 °C, 800 °C, and 1000 °C gives polycrystalline TiO_2 composed of pure anatase, a mixture of anatase and rutile, and pure rutile, respectively.

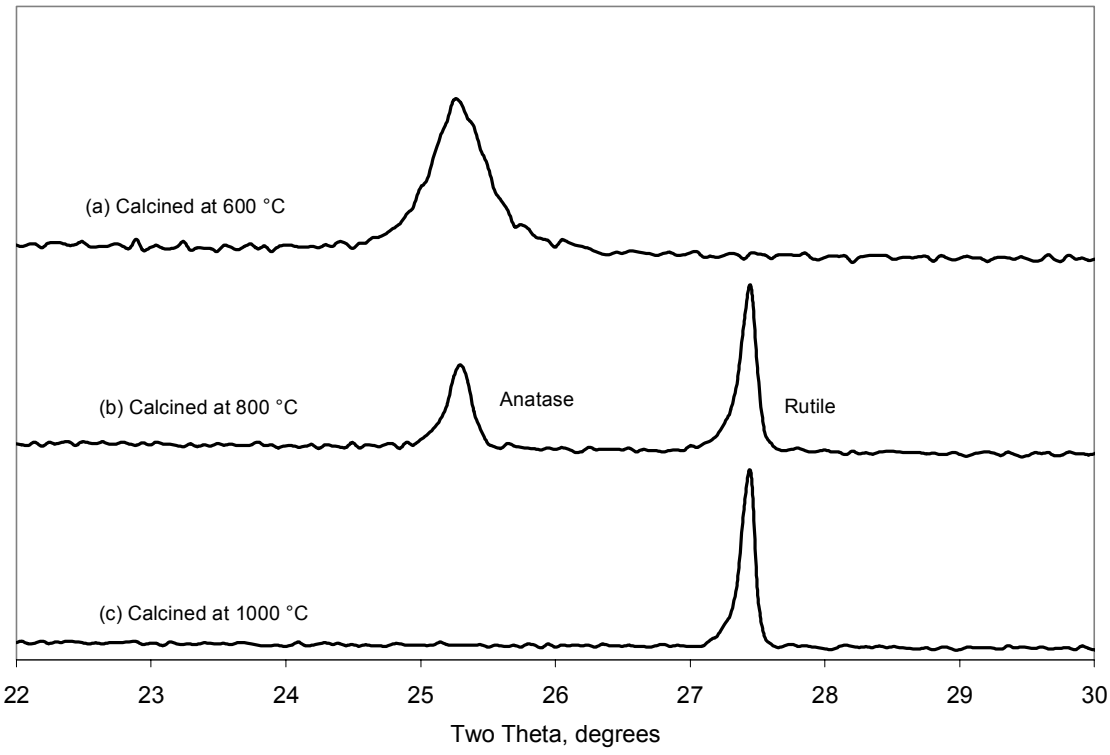

Figure 36: X-ray diffraction spectra of the synthesized TiO_2 particles.

From the width of the peaks in the spectra, the average crystallite sizes composing each of the polycrystalline particles was determined and are listed in Table 5. As shown, crystallite size increases with increasing calcination temperature and, for the biphasic sample heated at 800 °C, the rutile crystal (141 nm) is significantly larger than the anatase crystal (62 nm). This biphasic sample is composed of 46 wt.% anatase and 54 wt.% rutile, as determined from XRD analysis using the calibration curve shown in Figure 32. Table 5 also lists the average particle size of the synthesized and commercial TiO_2 powders.

Table 5: Synthesized and commercial TiO_2 particle characterization and corresponding opacity for a 1 vol. % cellulose film with a thickness of 70 µm.

	Crystal Phase	Phase wt.%	Crystallite Size	Particle Size	Crystals/ Particle	GSD	Opacity @ 70 µm
600	Anatase	100	16.6	498	27,000	1.10	63.9
800	Anatase	46	61.5	354	87	1.08	72.0
	Rutile	54	141.3		9		
1000	Rutile	100	290.8	576	2.0	1.58	78.2
Commercial	Rutile	100	210	336	1.6	1.22	73.7

The individual, nearly spherical crystals composing the synthesized polycrystalline particles can be seen in the TEM images shown in Figure 37, while the overall particle morphologies are shown in the SEM images provided in Figure 38. The images show that i) the 600 °C and 800 °C particles are approximately spherical in shape and ii) the 1000 ^{o}C particles have a high aspect ratio and are composed of a liner linkage of several individual rutile crystals with side-by-side arrangement.

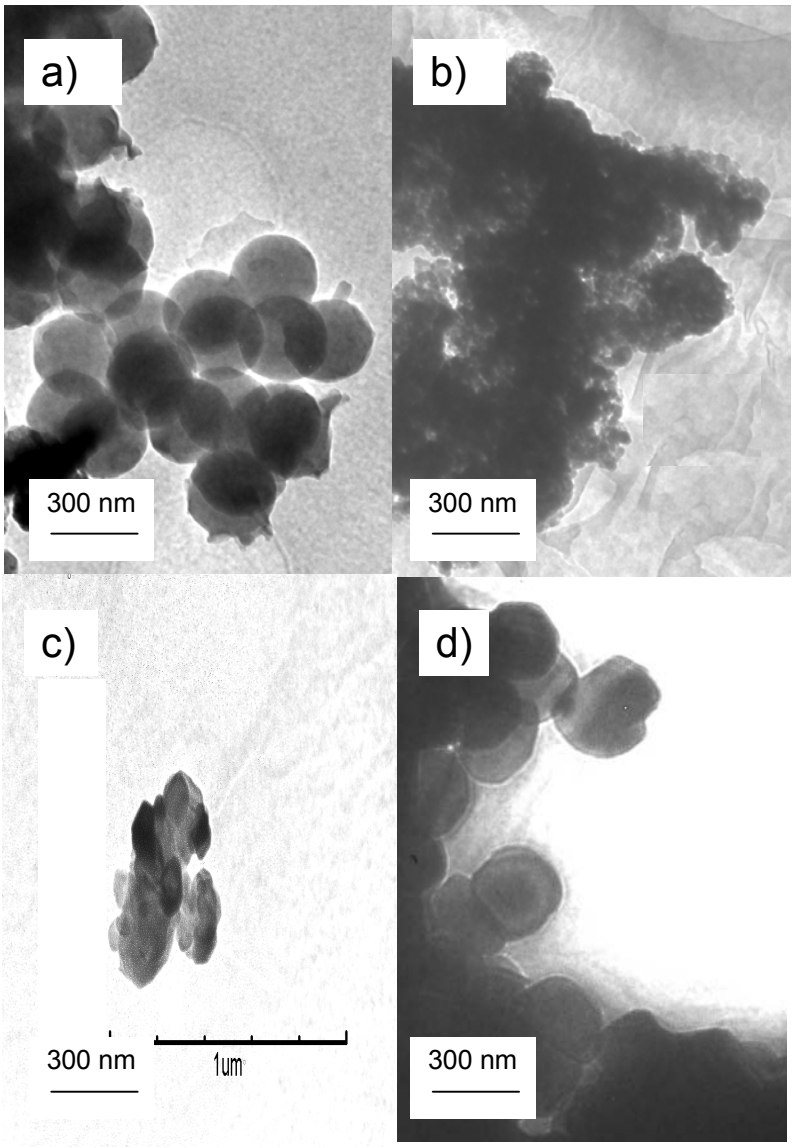

Figure 37: TEM images of synthesized TiO_2 particles prepared with the following heat treatments: (a) none, (b) 600 °C, (c) 800 °C, and (d) 1000 °C

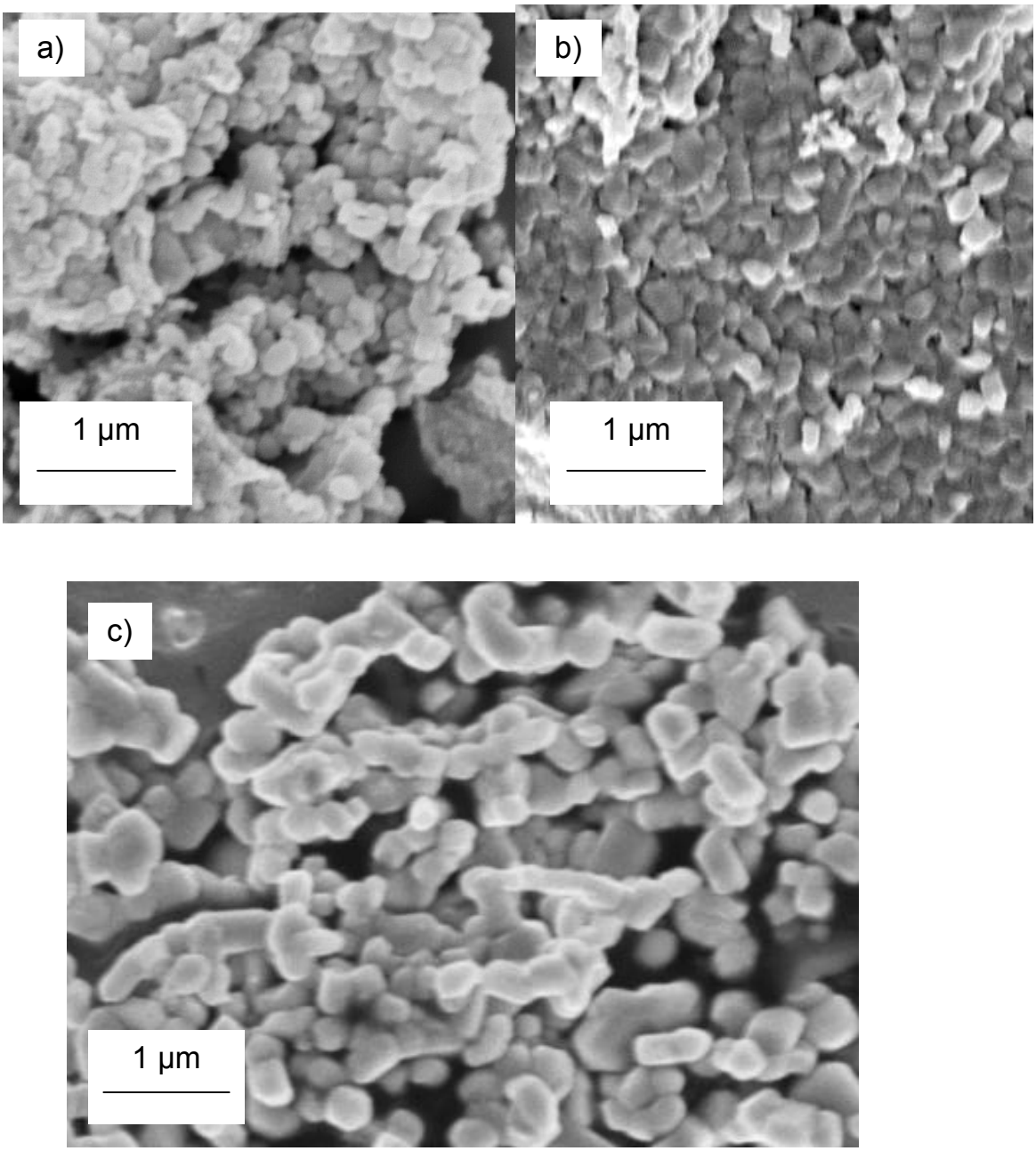

Figure 38: SEM images of the synthesized TiO_2 particles prepared with the following heat treatments: (a) 600 °C, (b) 800 °C, and (c) 1000 °C

The TEM image in Figure 39 of commercial rutile support the well known fact that many of the particles comprising commercial rutile powders are composed of crystal twins and, as a result, the particles are more oblong than spherical.

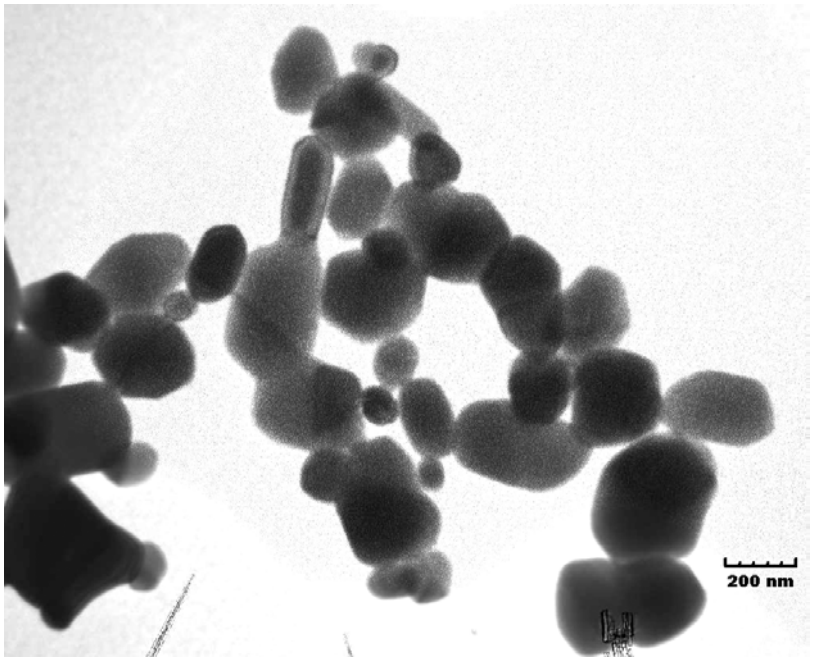

Figure 39: TEM image commercial rutile pigment

From the particle and crystallite size date, the average number of crystals per particle were estimated and are given in Table 5. This data shows that as calcination temperature increases, the number of crystals per particle decreases dramatically. With an average of 1.6 crystals/particle for the commercial rutile powder, there exists approximately one twin (with a particle size of 2*210=420 nm) for every one single crystal particles (210 nm), as estimated from the average particle size of 336 nm. The 1000 °C powder is composed of particles with an average of 2.0 crystals/ particle.

The opacity of cellulose films filled with commercial TiO_2 and the synthesized polycrystalline TiO_2 particles was investigated experimentally. Figure 40 compares the opacity of the films loaded with synthesized polycrystalline titania particles and commercial rutile, while Table 5 lists the corresponding opacity values obtained for a film thickness of 70 μm.

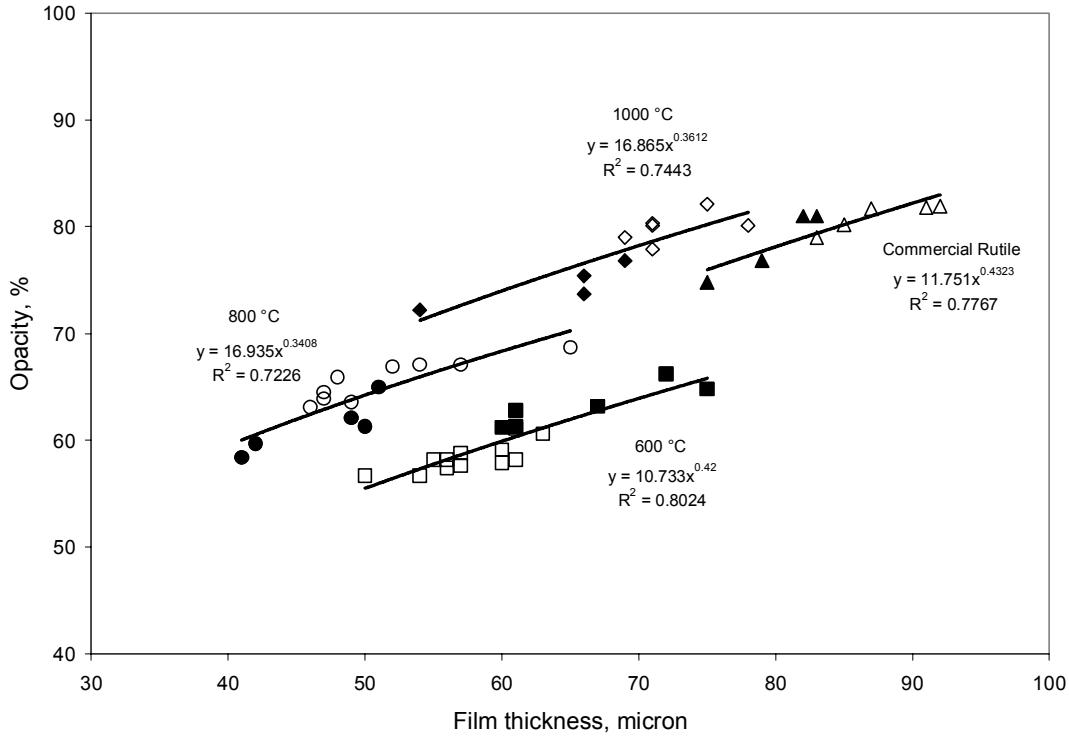

Figure 40: Comparison of opacity of cellulose films loaded with 1 vol. % synthesized and commercial rutile TiO_2 fillers. The open and closed symbols represent repeated experiments

The 600 ^{o}C sample composed of polycrystalline anatase gives 13% less opacity than commercial rutile. This result agrees closely with the literature which states that rutile pigments provide approximately 15% more opacity than anatase pigments as a result of

its higher index of refraction (24). Thus, the presence of many small anatase crystallites not appear to enhance the light scattering of the 600 °C polycrystalline anatase particles over traditional single (or double) crystal anatase pigments. Surprisingly, even though the 800 ^{o}C sample is an almost 50% mixture of rutile and the less effective light scattering anatase crystal, it provides an opacity comparable to commercial rutile. The 1000 °C sample composed of polycrystalline rutile provides 6% more opacity than the commercial sample. Figure 41 shows the effect of commercial rutile pigment volume concentration on film opacity, which indicates that, at a film thickness of 70 μm, 1.3 vol. % of commercial rutile is required to achieve the same opacity as 1 vol. % of the 1000 °C sample, a 30% increase in pigment loading.

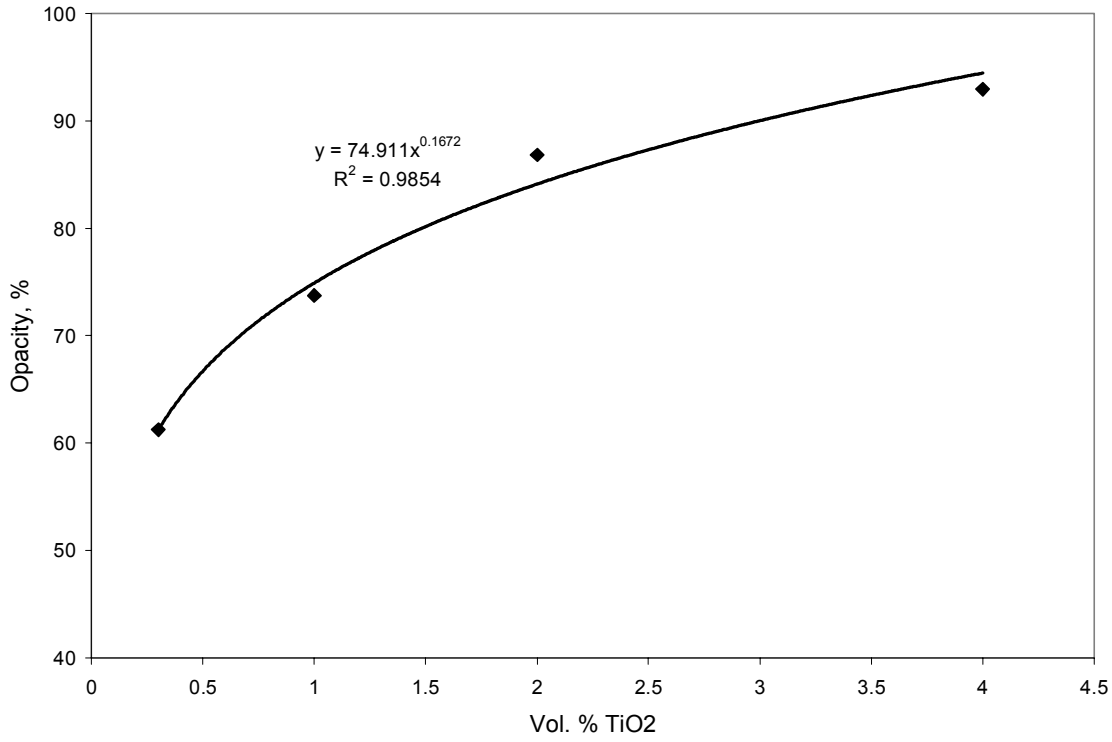

Figure 41: Calibration curve to determine concentration of commercial rutile required to achieve the same opacity as 1 vol.% of the 1000 °C synthesized sample for a film thickness of 70 μm.

Several numerical attempts have been made in the literature to model the light scattering efficiency of particle clusters composed of several individual spheres. These studies have shown that light scattering efficiency of small particle clusters is dependent on the geometrical arrangement of the primary particles, the number of primary particles, and the size of the primary particles. Based on these studies, we hypothesize that the most dominate factors accounting for the difference in light scattering efficiency between the commercial rutile and 1000 ^{o}C samples are the differing number and size of rutile crystals composing the individual particles. As discussed, the commercial rutile powder is composed of single crystals and twins with a primary crystal size of 210 nm, while the

1000 ^{o}C is composed of a liner linkage of 2 rutile crystals on average with primary crystal size of 291 nm. The T-matrix method was used to compare the theoretical light scattering efficiency of single rutile crystals with that of particles containing multiple, linearly arranged rutile crystals when embedded in a cellulose matrix and irradiated at 572 nm. For particle clusters, the T-matrix method is based on representing the total scattered field from a cluster as a vector superposition of the partial fields scattered by the individual cluster components (25). Conceptually, the presence of multiple particles provides more surface irregularities and interfaces for light to scatter. The T-matrix method can account for the constructive and destructive interferences of the light waves scattered off all the surfaces. In this way, one can evaluate the effect of cluster geometry on the superposed intensities of light waves scattered in each direction. A significant advantage of the T-matrix method is that it calculates the scattering properties of the cluster averaged over all possible orientations of the cluster with respect to the incident light. The code used has been thoroughly tested, gives very accurate results within the domain of numerical convergence, and has been extensively used in various applied sciences (2). Figure 42 shows that an optimally sized single rutile crystal (~300 nm) is more efficient than a particle composed of multiple crystals of the same size. As the number of crystals in the pigment particle increases, the light scattering efficiency decreases. This result is consistent with the well-known phenomenon of decreasing opacifying power upon pigment flocculation. However, below a primary crystal size of ~200 nm, a particle composed of multiple crystals is more efficient than a single crystal particle. For example at 100 nm, light scattering efficiency increases as the number of rutile crystals composing the pigment increases.

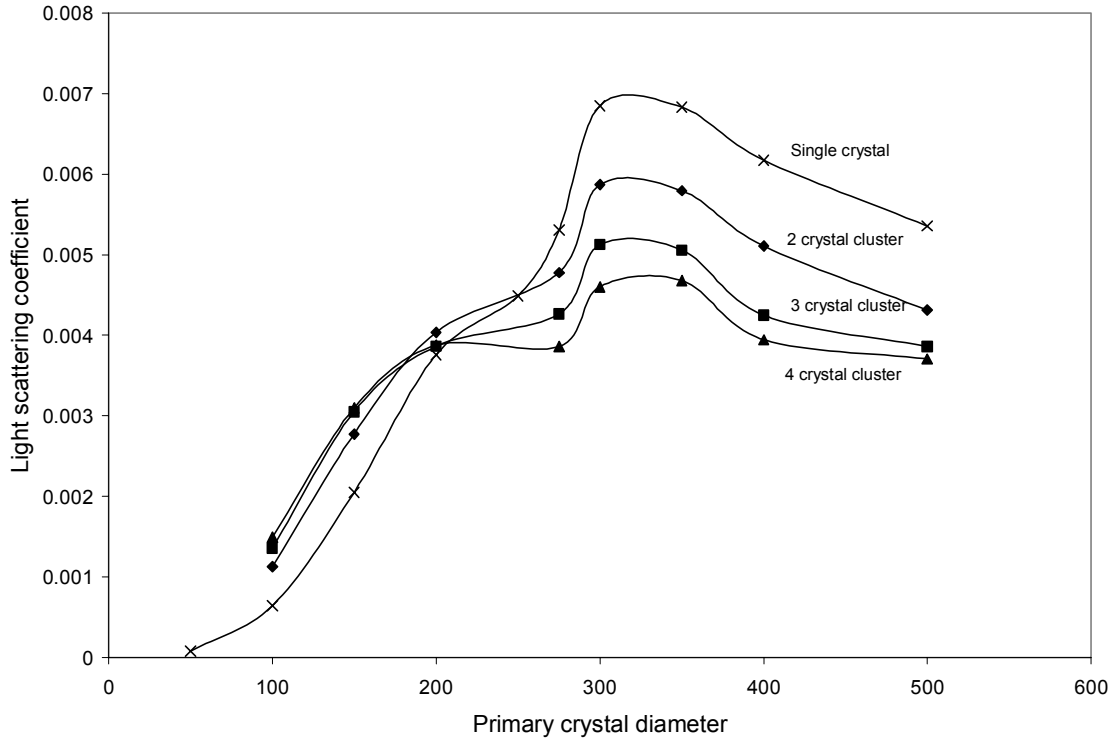

Figure 42: Theoretical light scattering efficiency of linearly arranged rutile clusters calculated using the T-matrix numerical method.

The theoretical results explain the experimental data and suggest a way to manufacture more efficient rutile TiO_2 than currently available. Figure 42 shows that because the 1000 °C sample is composed of particles with an optimally sized primary crystal size (291 nm), these particles have more light scattering efficiency than the commercial pigment composed of non-optimally sized crystals (210 nm). For single crystal particles, an optimally sized particle has about 43% more light scattering efficiency than one with a diameter of 210 nm. Even the multiple crystal pigments in the 1000 °C sample have more efficiency than the single crystal (or twin) commercial sample. These results indicate that

a fundamental distinction between overall particle size and primary crystal size must be made when manufacturing TiO_2 pigments. Currently the industry provides rutile pigments with an *overall particle* size close to the optimal *single crystal* particle size. But to achieve this average overall particle size, about two-thirds of the sample is composed of inefficient single crystals with diameters of 210 nm and the reminder is composed of inefficient twins with primary crystal sizes of 210 nm (giving an overall particle size of 420 nm). Thus, the efficiency of rutile pigments can be increased dramatically by controlling the *primary crystal* size rather than the *overall particle* size.

One of the possible reasons for the surprisingly high light scattering efficiency of the 800 °C sample composed of about 50 wt.% anatase and rutile crystals is the presence of grain boundaries between two different crystals. It is well known that light is scattered by the mechanisms of reflection and refraction when moving between two media having different refractive indices. The crystal particles of anatase and rutile TiO_2 are optically anisotropic, or birefrigent, where the refractive index depends on the direction of propagation and polarization of incident light with respect to the crystal structure. Both anatase and rutile exhibit tetragonal crystal structures with a single optic axis (parallel to the z-axis). Therefore both crystals are optically anisotropic and have two different refractive indices at a given wavelength: the ordinary n_o (for radiation polarized in the x or y direction; perpendicular to the z-axis) and the extraordinary n_e (for radiation polarized in the z-axis). When a polycrystalline material is composed of randomly oriented crystallites (as is the case for the synthesized TiO_2 particles), light propagating in a particular direction will pass through many crystals with different indices of refraction

and some degree of light scattering will occur. In contrast, pore-free polycrystalline materials having optically isotropic crystallites with only one index of refraction, such as yttrium oxide, are transparent since no light scattering occurs throughout the material (26). For rutile illuminated at 572 nm, $n_o = 2.63$ and $n_e = 2.93$, while for anatase $n_o = 2.58$ and $n_e = 2.50$ (27). Because of the large difference in their ordinary and extraordinary refractive indices, both crystals are highly birefrengent. Thus for the 800 ^oC biphasic particle clusters with randomly oriented grains, there can be a significant discontinuity of the refractive index (Δn) at the grain boundaries. The fraction of the intensity of incident light that is reflected at a grain boundary, R, is given by Equation 1. For two bordering anatase and rutile particles Δn can vary from a low value of $\Delta n = n_0^{rut} - n_0^{ana} = 0.05$ when the optical axes of the particles are aligned and to a high value of $\Delta n = n_e^{rut} - n_e^{ana} = 0.43$, In the latter case, 43% of the incident light is reflected at the grain boundary. In addition, as Δn increases refraction or the bending of light across a grain boundary also increases.

Conclusion

Polycrystalline TiO_2 nanoparticles were synthesized with varying phase composition, crystallite size, and crystallite arrangement. The morphology and crystalline structure of these particles were characterized using SEM, TEM, XRD, and light scattering. The light scattering efficiency of the pigments were evaluated by measuring the opacity of optically uniform cellulose nanowhisker films loaded with 1 vol.% pigment. Polycrystalline anatase pigments with crystal sizes of 17 nm provided 13% less opacity than the commercial rutile pigment, while polycrystalline pigments containing a one-to-one mixture of anatase and rutile crystals provided similar opacity as commercial rutile.

Polycrystalline rutile pigments composed of *on average* two rutile crystals per particle in a linear arrangement with crystal sizes of 291 nm gave 6% more opacity than the commercial rutile pigment composed of *on average* 1.6 rutile crystals per particle with crystal sizes of 210 nm. Theoretical light scattering calculations using the T-Matrix Method confirm the higher efficiency of the synthesized polycrystalline rutile pigments over commercial rutile as a result of the optimal size of the crystals composing the particles. It is suggested that the efficiency of rutile pigments can be increased dramatically by controlling the *primary crystal* size rather than the *overall particle* size. It is believed that the greater than expected light scattering efficiency of the biphasic pigment results from reflection and refraction of light at the grain boundaries between crystals of different phase, which have different refractive indices.

CHAPTER 5

ENHANCED LIGHT SCATTERING FROM *HOLLOW* POLYCRYSTALLINE TIO_2 PARTICLES IN A CELLULOSE MATRIX

Abstract

The opacifying power of hollow polycrystalline rutile particles was found experimentally to be superior to that of a commercial rutile pigment in a highly pressed bleached fiber matrix, depending on cavity size, while the opacifying power of silica-rutile titania core-shell particles was found comparable to commercial rutile at constant *titania* loading. The light scattering efficiency of titania core-shell particles was also shown to be dependant on the light scattering efficiency of the core material. The light scattering efficiency of the polycrystalline silica cores was found to depend on calcination temperature and crystal structure.

5.1 Introduction

Characterization of the scattering of light by titanium dioxide particles has been the subject of significant research for many decades, as TiO_2's many technological applications often depend on its high light scattering efficiency. Because of its exceptionally high refractive index and whiteness, titanium dioxide is used to impart opacity to a wide variety of products including coatings, paints, plastics, paper, rubber printing inks, synthetic fibers, ceramics, cosmetics, and even toothpaste (60). Increasing global demand growth, coupled with raw material supply constraints, has lead to

increasing prices for an already exceptionally expensive pigment. The introduction of novel, even more efficient light scattering TiO_2-based pigments can help manufactures limit costs while maintaining the required optical properties of their product. One approach to increasing the efficiency of TiO_2 is to create unique pigment morphologies designed to scatter light more effectively than conventional TiO_2 pigments. We recently showed that optimization of the polycrystalline structure of TiO_2 pigments leads to enhanced light scattering over conventional titania pigments. Modifying pigment structure to enhance light scattering is not a new concept. Pigment suppliers offer several varieties of "Structured and Engineered pigments" including highly structured or calcined clay, TiO_2/clay aggregates, and hollow plastic pigments. Structured pigments like calcined clay and TiO_2/clay enhance opacity because the aggregation of pigments into larger particles offers more surfaces and void volume to scatter light (90). Uniform, hollow latex plastic pigments enhance opacity by incorporating large amounts of air into coatings. Unlike solid particles whose optical performance depends on the surrounding media, the hollow spheres have a large air/particle shell interface on its interior surface that is always available to scatter light, no matter what media surrounds the outer surface of the particle (91). From experimental studies, the optimal particle size and void volume for the spheres are 1,060 nm and 50%, respectively (92).

A recently developing field of practical and scientific interest is the synthesis of novel inorganic pigment structures using sophisticated techniques borrowed from the fields of nanotechnology and interfacial science. While such particles have wide applicability across many fields, for papermaking they are designed to offer enhanced optical and

physical performance. Ideally these particles should have high opacity and provide high bulk and minimal impact on paper strength. As a result of these requirements, most of these novel fillers have a highly porous or hollow structure, designed to minimize material usage and density and enhance light scattering. These particles are largely composed of traditional inorganic papermaking pigments like calcium carbonate, clay, and TiO_2. Several research groups have synthesized hollow calcium carbonate particles ranging from 0.5 to 300 μm (11-19). Enome and Tsujino prepared spherical hollow particles of calcium carbonate between 0.5 and 2 μm in diameter using interfacial reaction in a water-in-oil (W/O) emulsion (14). The shell is composed of aggregated crystals between 50 and 300 μm in mixed crystal forms of calcite and vaterite. These particles give higher specific light scattering coefficient than conventional ground calcium carbonate for both paper filler and coating applications. Also, when compared to hollow plastic pigments, the hollow PCC particles give higher light scattering, presumably due to PCC's higher refractive index. Researchers have also synthesized hollow silica (20, 21) and clay particles (21, 22). Many reports have been published on the synthesis of spherical core-shell (23, 24) and hollow (25-44) titania particles.

If hollow plastic and calcium carbonate pigments, with low shell refractive near 1.59 enhance light scattering as light is refracted between the shell and the air-filled core, one can easily anticipate even more light scattering from a titania shell with a refractive index of 2.72. Hsu et al were the first group to experimentally and theoretically investigate the hiding power of core-shell titania particles (94). They coated monodispersed spherical silica with titania and evaluated hiding power in a cellulose matrix as a function of core

diameter (0.2-1.3 μm) and titania shell thickness. Optimum opacity was obtained for core-shell particles with an overall diameter of ~ 1.0 μm and a shell thickness of 50 nm, corresponding to about 40 wt% TiO_2. This powder gave an opacity comparable to a commercial rutile powder when incorporated into an Avicel matrix at constant mass loadings of 17%, 37%, and 50% filler. These experimental results were supported by theoretical light scattering calculations using the well-known BHCOAT computer program based on Mie theory as applied to concentric spheres. Several years after this study, researchers from DuPont Titanium Technologies published a rebuttal based on theoretical light scattering calculations using the program BHCOAT modified to incorporate the asymmetry parameter, which accounts for the direction of light scattered from a particle (95). The researchers argue that the theoretical calculations performed by Hsu et al. for an isolated particle cannot be used to anticipate the light scattering of TiO_2 in actual films where multiple light scattering occurs between the large numbers of particles present. The opacity of a film depends on the ability of the pigment to scatter light back in the direction from which it came. A single particle efficiently scatters light, but typically for small spherical particles only a small portion is scattered in the backward direction. However, light scattered by multiple particles is bent a sufficient number of times to achieve a backwards direction. Thus in practical applications, the reflectance of light by a film (opacity) depends on the predominant direction in which the pigments scatter light and the number of times the light is scattered by other particles. The asymmetry parameter includes the scattering angle to give a scattering parameter that is meaningful to correlate with the value of a pigment for opacification in real applications.

Their calculations show that core-shell pigments are substantially less efficient light scattering materials than pure rutile.

This paper presents an experimental solution to the problem of light scattering by well dispersed polycrystalline core-shell and hollow titania particles in an optically uniform, transparent, pore free cellulose nanowhisker matrix. The effects of shell crystal structure, core structure, and core/cavity size on the opacifying power of the synthesized pigments are investigated and compared with a commercial rutile pigment.

5.2 Experimental

5.1.1 Materials

Cotton pulp (Procter & Gamble Cellulose) and rutile titanium dioxide (Tiona RCS-P, Millennium Chemicals) were donated and used as received. Commercial dry lap bleached Kraft pulp (1:1 softwood/hardwood) was refined to a Canadian Standard Freeness of 400. Sulfuric acid (96.5%, EM Science), poly(acrylic acid, sodium salt) (PAA, MW 5,100, Aldrich), polyethylene glycol (PEG, MW = 8,000, Aldrich), poly(vinylpyrrolidone) (PVP, MW = 55,000, Aldrich), titanium(IV) butoxide (TBT, 97%, Aldrich), tetraethyl orthosilicate (TEOS, 98 wt. %, Aldrich), ammonia (29 wt.-%, VWR), hydrofluoric acid (48%, Aldrich) and ethanol (anhydrous, VWR) were used without further purification. Water was obtained from a Nanopure ultrapure water system with a resistivity of about 18 MΩ cm.

5.1.2 Preparation

As shown in the TEM images of Figure 43, monodispersed silica particles with diameters of 272 nm and 1186 nm were prepared by hydrolysis of TEOS in ethanol in the presence of water and ammonia. Particles with a diameter of 272 nm were prepared following the methods of Hsu *et al* and Giesche (23, 113). Water (53.307 g) and ammonia (29 wt.-%, 26.441 g) were added to 330 mL ethanol and heated to 40 °C under reflux. TEOS (98%, 26.573 g) was also heated to 40 °C in a separate, closed container. TEOS was then added to the ethanol solution under vigorous stirring. Fifteen seconds later, the stirring was reduced to low and continued for 1 hour at 40 °C. The resulting solids were isolated by three centrifugation and ethanol washing cycles at 25,900 RCF (Relative Centrifugal Force) for 2.5 min and lyophilized.

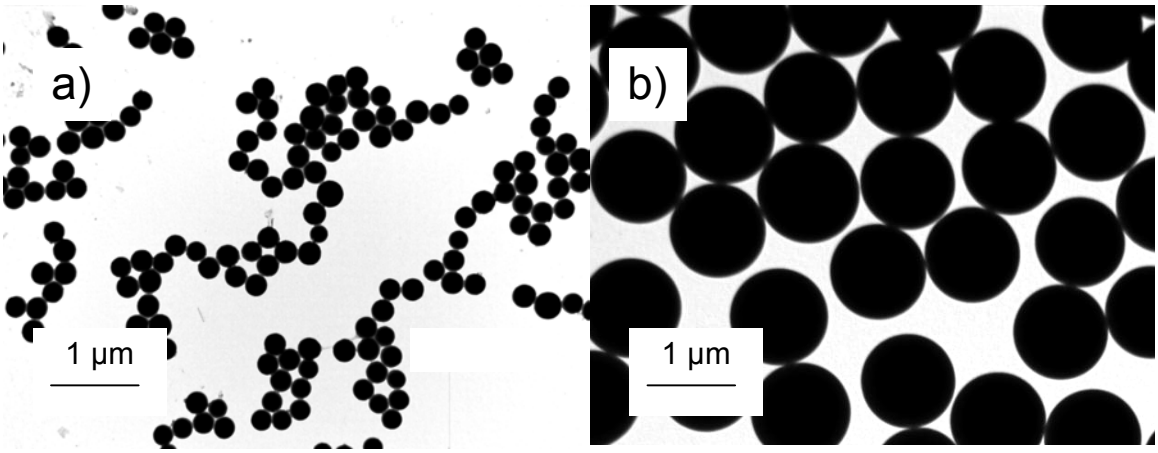

Figure 43: TEM images of the monodisperse silica cores with average diameters of (a) 272 nm and (b) 1186 nm.

Silica particles with a diameter of 1186 nm were prepared following the method of Barder and DuBois (114). The synthesis requires (a) 312 mL of TEOS (98%) and (b) 651

mL of a solution containing ethanol (11.3 wt.-%), ammonia (10.6 wt.-%), and water (78 wt.-%). In Step 1, 12 mL of solution (a) are combined with 50 mL of solution (b) at room temperature and stirred gently for 5 min. The same amounts of solutions (a) and (b) are then added to the reaction every 5 minutes for 1 hour for a total of 12 additions. In step 2, the same amounts of solutions (a) and (b) are added to the reaction every 3.5 minutes for 2 hours and fifteen minutes for a total of 39 additions. The resulting solids were isolated by three centrifugation and ethanol washing cycles at 25,900 RCF (Relative Centrifugal Force) for 2.5 min and lyophilized.

To study the affect of calcination on the polycrystalline composition of the silica particles, both silica powders were calcined at 600 °C and 1000 °C. Prior to calcination the particles were dispersed in a cellulose matrix to prevent interparticle sintering, as discussed in Chapter 4.

The lyophilized 272 nm and 1186 nm silica templates were coated with an amorphous titania shell using the sol-gel synthesis methods of Hanprasopwattana *et al* and Liu *et al* (115, 116). Table 6 gives the concentrations of reactants used for each template to obtain an amorphous shell thickness that is approximately 20% of the core-shell radius. Using the 272 nm template case as an example of the general synthesis method, 0.075 g of the silica powder was first added to 10 mL of ethanol along with 0.06 g of PVP dispersant and sonicated for up to 45 minutes (5 minutes for the 1 μm template) to completely disperse the particles. The remaining 40 mL of ethanol were added to the suspension along with 0.224 g of TBT solution (96%). Under moderate stirring at room temperature,

0.512 g of water was added to the system at a rate of 0.003 g/min. The resulting solids were isolated by three centrifugation and ethanol washing cycles at 25,900 RCF (Relative Centrifugal Force) for 2.5 min and vacuum dried at 60 °C.

Table 6: Reactant concentrations for synthesis of titania coated silica core-shell particles.

Silica diameter, nm	272	1186
Silica, g	0.075	0.075
PVP, g	0.06	0.06
Ethanol, mL	50	50
TBT (96 wt.-%), g	0.224	1.1228
Water	0.512	2.56

The particles were then calcined in a cellulose matrix as described in Chapter 4 at either 600 °C or 1000 °C for 1.5 hours to obtain anatase or rutile polycrystalline shells, respectively. Half of the calcined core-shell powder was then treated with hydrofluoric acid overnight to dissolve the silica core and obtain hollow polycrystalline particles. Excess acid was removed by dialysis (Spectra/Por membrane, MWCO 50K) against water for several days until the water achieved a neutral pH. Figure 44 illustrates the four different particle morphologies synthesized four each silica template size, giving a total of eight morphologies. However, the titania shell of the 1 μm core-shell and hollow particles calcined at 600 °C did not remain intact during synthesis and these powders were discarded.

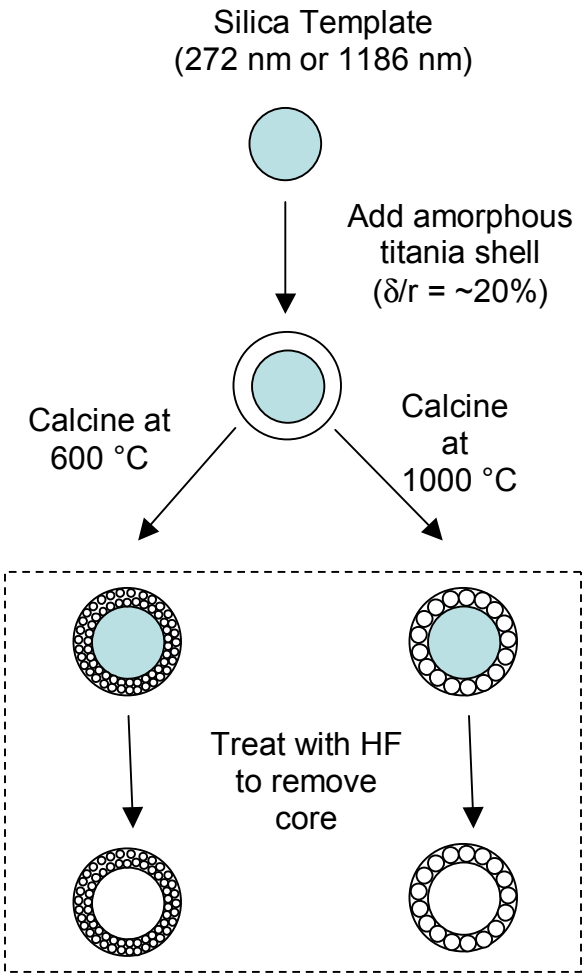

Figure 44: Illustration of synthesized core-shell and hollow titania morphologies

In order to compare the opacifying power of the synthesized nanoparticles with commercial rutile titania, the powders were distributed throughout a thin cellulose film. In a typical experiment, 0.04 g of powder was dispersed in approximately 10 mL of water along with 0.004 g of PAA dispersant and sonicated (or mini-vortexed in the case of hollow particles) for 10 minutes. The solutions were then allowed to rest for about 2

minutes. During this time, oversized particles that could not be dispersed into primary particles during sonication, either because of agglomeration or sintering during calcination, quickly settle to the bottom while fully dispersed primary particles remain in the supernatant. The supernatant was then removed from the settled solids and the settled solids were dried under vacuum and weighed. The supernatant was also weighed such that the exact concentration of the solution could be determined.

Cellulose films with a known weight concentration of uniformly distributed particles where then obtained by combining the well-dispersed filler suspension prepared above with PEG (whose role will be discussed below) and a gel-like solution of cellulose whiskers. This gel-like mixture was allowed to dry on a transparency within a 1.25 x 1.25 inch area framed by Scotch tape. For the typical film with a particle concentration of 3 wt.%, 3.9105 g of cellulose whiskers solution (8.27 wt. %) was combined with 0.1386 g of PEG, and the filler suspension containing 0.01429 g titania. This mixture was then pipetted onto four separate 1.25 X 1.25 inch area films. The cellulose nanowhiskers were prepared as outlined in Chapter 4.

Since the hollow titania particles have a porous shell, the effect of air entrapped in the core on light scattering (and opacifying power) is negated when embedded in the cellulose/PEG film, since the liquid PEG fills the center cavity. Thus, in order to compare the hiding power of the hollow particles with the corresponding core-shell particles and with commercial rutile, the fillers were incorporated into a matrix composed of bleached fibers. This matrix was then highly pressed to remove air pores. Experimentally, the pulp

was concentrated to a consistency of 5.47% such that only water bound to the pulp solids remained. The pulp (4.57 g) was then combined with 0.773 g of 1 wt % TiO_2 solution containing 0.1 wt.% PAA dispersant and minivortexed. The resulting paste was then spread onto a metal platen in a 4 x 1 inch square and vacuum dried at 120 °C until slightly damp and pressed at 50 psi at 105 °C for 2 minutes using an automated pressing apparatus (P. Bonk & Co.). The resulting paper sheet was cut into four samples for optical testing.

5.1.3 Characterization

Transmission electron microscopy (TEM) was performed using a Hitachi HD-2000 Field Emission Gun (FEG) microscope at 200kV. X-ray diffraction (XRD) was carried out using an X'Pert Pro Alpha-1 diffractometer with an incident beam monochrometer allowing only the $K\alpha_1$ component of Cu radiation. XRD spectra were analyzed using JADE 7 software from Materials Data. It is well known that the width of a peak in a diffraction pattern results from instrument optics and crystallite microstrain and size. Using the JADE software, the effect of instrumental broadening was removed by calibration with the standard LaB_6 (NIST, 660 SRM) and crystallite strain was calculated to be zero. Thus, crystallite size was calculated from peak broadening using classical Williamson-Hall plots (117). The plots were constructed for all non-overlapping peaks occurring for two theta values between 20° and 80°. Pigment average particle size and particle size distributions were obtained with a Malvern 3000 Zetasizer. The width of the particle size distribution, or geometric size distribution, GSD, was calculated from the particle size distributions shown in Figures 45 according to Equation 16.

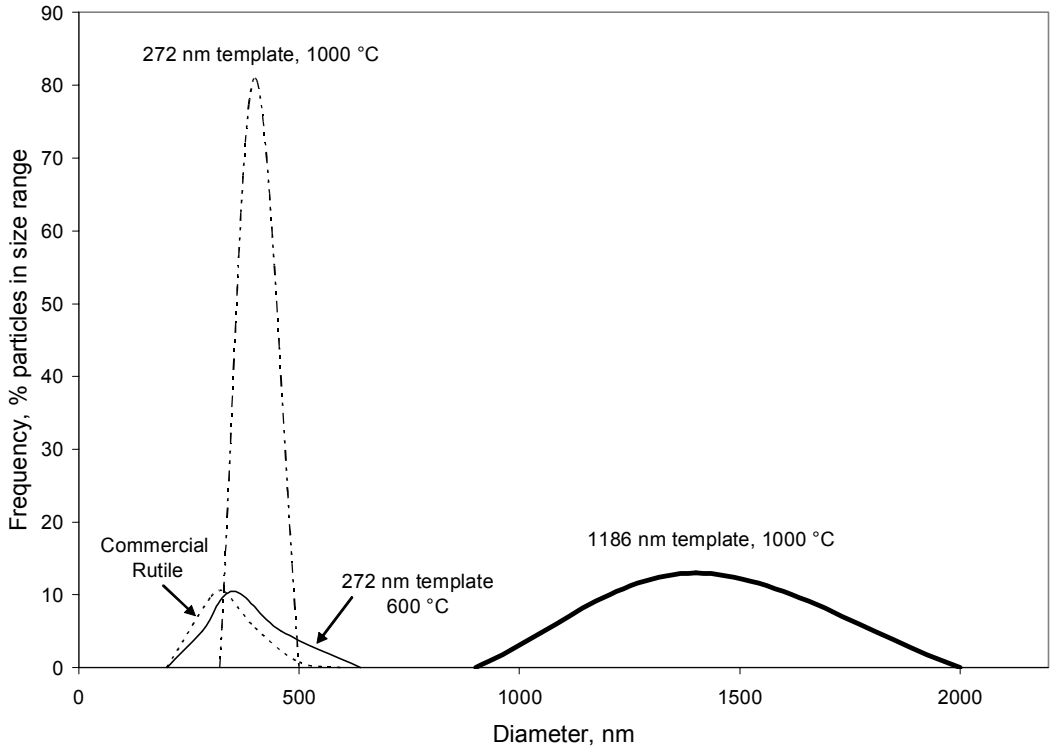

Figure 45: Particle size distributions of synthesized and commercial TiO_2 obtained from light scattering.

The TAPPI opacity of the pigment filled cellulose films was measured using a Technidyne BNL-3 Perimeter with a quartz-tungsten-halogen lamp filtered for illumination at 572 nm. Film thickness was measured using a hard caliper instrument (AB Lorentzen & Wettre).

5.3 Results and Discussion

The first part of this study evaluates the light scattering power of core-shell and hollow titania particles in an optically uniform cellulose/PEG film. The same method and matrix material was used to evaluate the light scattering by solid polycrystalline titania particles in Chapter 4. A cellulose matrix was chosen to evaluate the light scattering performance of synthesized TiO_2 particles for two reasons: 1) papermaking represents an important technological application of TiO_2 and 2) there is an established debate in the literature on the relationship between morphology and TiO_2 opacifying power in a cellulose matrix (23, 95). The light scattering power of TiO_2 in pigment applications depends on several factors including the severity of particle flocculation, the refractive index of the medium in which the pigment is dispersed, the wavelength of incident light, particle size distribution, particle size, and pigment concentration. In order to experimentally evaluate the effects of pigment composition and morphology on TiO_2 opacifying power, care must be taken to fix these variables. The reader is referred to Chapter 4 for a discussion on how the first three variable are controlled with this experimental design. It is well known that pigments with a broad size distribution centered around the optimal size have less opacifying power than a corresponding monodisperse distribution (83). Pigment manufactures report the width of the particle size distribution as geometric size distribution, GSD. Typically, as GSD increases for a given pigment, opacifying power is lower. Figure 45 shows the particle size distributions of the synthesized and commercial rutile TiO_2 powders. The widths of distribution are similar for all powders except the one synthesized from the 272 nm template and calcined at 1000 °C sample. Figure 46 shows

that even though this synthesized sample has a significantly lower GSD than the other particles, it does not give the highest opacity.

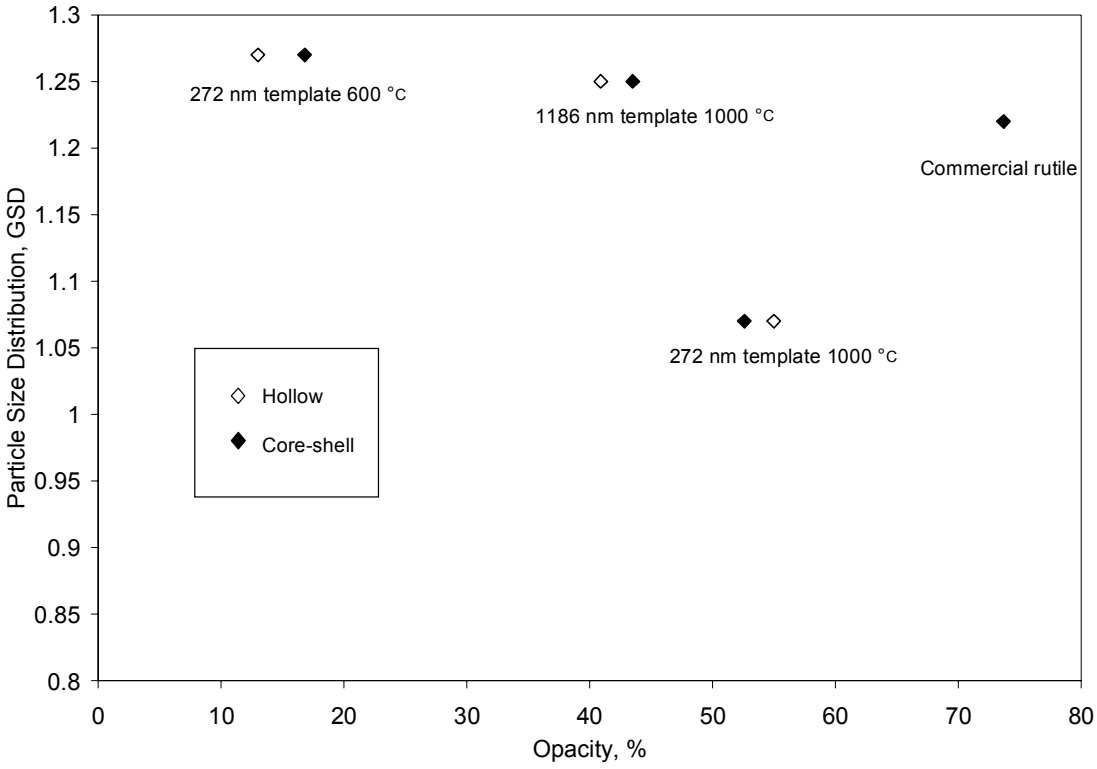

Figure 46: Relationship between GSD and opacity for the synthesized and commercial rutile powders.

Particle sizes under investigation were chosen based on previous work by Hsu et al who showed experimentally that opacifying power of titania coated silica particles depends on silica core diameter and titania shell thickness. Optimum opacifying power was observed for silica cores ~ 1.0 μm in diameter and for the maximum titania thickness that they could achieve, δ/r ~10%, where δ is shell thickness and r is the diameter of the core-shell particle. In order to confirm these results, silica cores with diameters of 272 nm and 1186

nm were chosen. The sol-gel coating method used in this study allows deposition of uniform amorphous titania shells with any thickness. The amorphous titania shell thickness target was fixed at δ/r ~20% for this study. Upon crystallization of the shells during calcination, the density and thickness of the shell changes, depending on calcination temperature and titania crystal phase formed. Table 7 lists the post calcination particle sizes and shell thicknesses.

Table 7: Synthesized and commercial TiO_2 particle characterization and corresponding opacity for a 70 μm thick cellulose film loaded with 3 wt% pigment

		Crystal Phase	Crystallite Size, nm	Particle Size, nm	Shell thickness, nm	Shell thickness, δ/r	Opacity @ 70 μm
272 nm template 600 °C	Core-shell	Anatase	19.9±1.5	357	43	24%	16.8
	Hollow						18.3
272 nm template 1000 °C	Core-shell	Rutile	82.3±1.2	400	64	32%	52.6
	Hollow						55.0
1186 nm template 1000 °C	Core-shell	Rutile	158.9±5.4	1425	120	17%	41.8
	Hollow						40.9
Commercial		Rutile	210	336	N/A	N/A	73.7

In this study, the pigment concentration was limited to 3 wt.% to eliminate the effects of dependent scattering between particles. Dependent scattering arises from the perturbation of single particle scattering by near field optical interactions with neighboring particles in close proximity and is negligible only in dilute pigment dispersions not exceeding concentrations of ~5% by volume (65). For solid titania particles like commercial rutile (ρ=4.26 g/ml), 3 wt.% corresponds to 1 vol.%, while for the largest and least dense

hollow micron sized particles used in this study (ρ=1.93 g/ml), 3 wt.% corresponds to 2 vol.%. Thus, dependant scattering is negligible.

The phase composition and crystallite size of the titania shell are dependant upon calcination temperature. X-ray analysis showed the titania shells for the particles calcined at 600 °C and 1000 °C to be composed of pure anatase and rutile, respectively. As shown in Table 7, for both coated templates calcined at 1000 °C , the average rutile crystallite size and the shell thickness estimated from light scattering data agree closely, 82 nm and 64 nm for the 272 nm template and 159 nm and 132 nm for the 1186 nm template, respectively. The close agreement of these values suggests that the rutile shell is one rutile crystal thick. The particle morphologies of the synthesized hollow and core shell particles are shown in the TEM and SEM images of Figures 47-49. While the 600 °C shell is smooth and uniform, the 1000 °C samples have a rough and irregular shell.

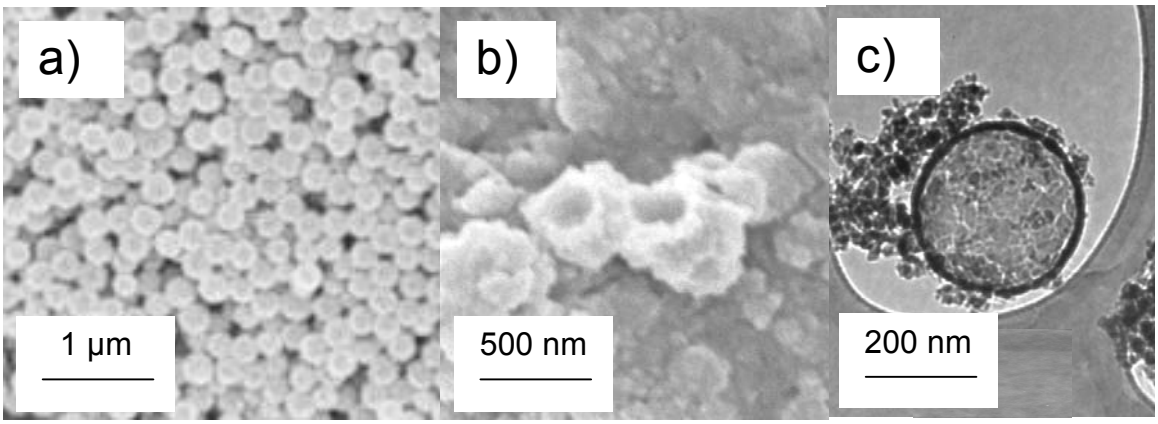

Figure 47: SEM images of synthesized (a) core-shell and (b) hollow titania particles with a 272 nm core calcined at 600 °C and (c) TEM image of corresponding hollow particles

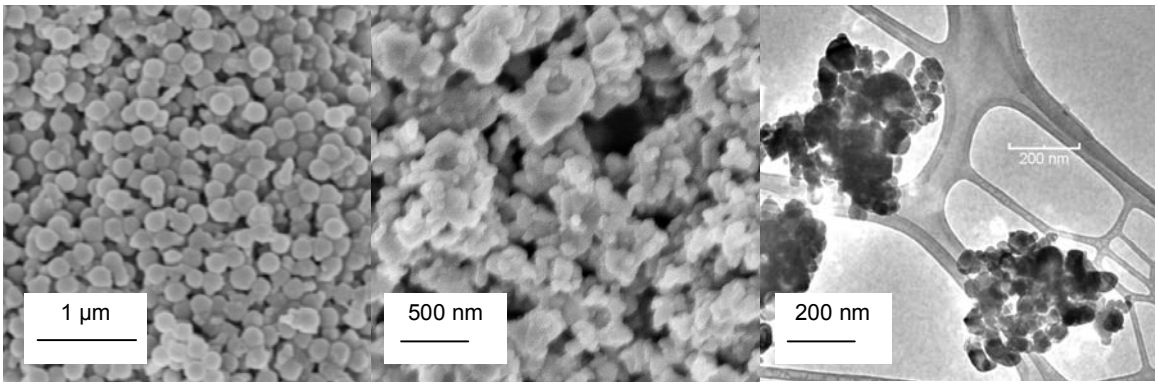

Figure 48: SEM images of synthesized (a) core-shell and (b) hollow titania particles with a 272 nm core calcined at 1000 °C and (c) TEM image of corresponding hollow particles

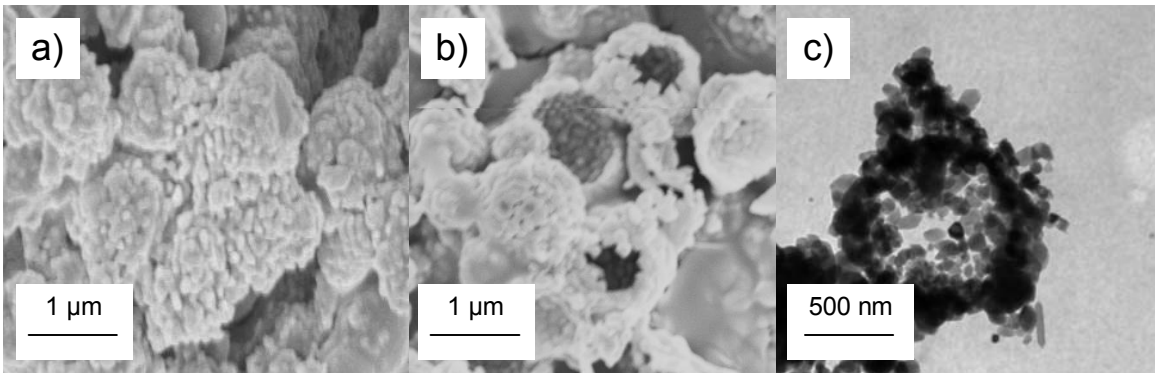

Figure 49: SEM images of synthesized (a) core-shell and (b) hollow titania particles with a 1186 nm core calcined at 1000 °C and (c) TEM image of corresponding hollow particles

The opacifying power of the synthesized polycrystalline core-shell and hollow TiO_2 particles in a cellulose film was investigated experimentally and compared to that of a commercial rutile TiO_2 pigment. Figures 50 and 51 compare the opacity of cellulose whisker/PEG films loaded with the titania particles. It is important to note that due to the porous nature of the hollow particles, their interior in this matrix is filled with liquid PEG rather than air. Since the refractive index of air is 1 compared to 1.467 for PEG, the refraction of light going from the TiO_2 shell to the interior cavity, and therefore light scattering, should be greater for air filled cavities. This issue will be address below. The opacifying power of the titania core-shell and PEG filled hollow titania particles are very similar at constant pigment loading. Also, in this matrix, the opacifying power of the synthesized particles is significantly less than that of commercial rutile, with the 600 °C particles composed of the less efficient light scattering anatase phase being dramatically worse. Table 7 lists the corresponding opacity values for a film thickness of 70 μm.

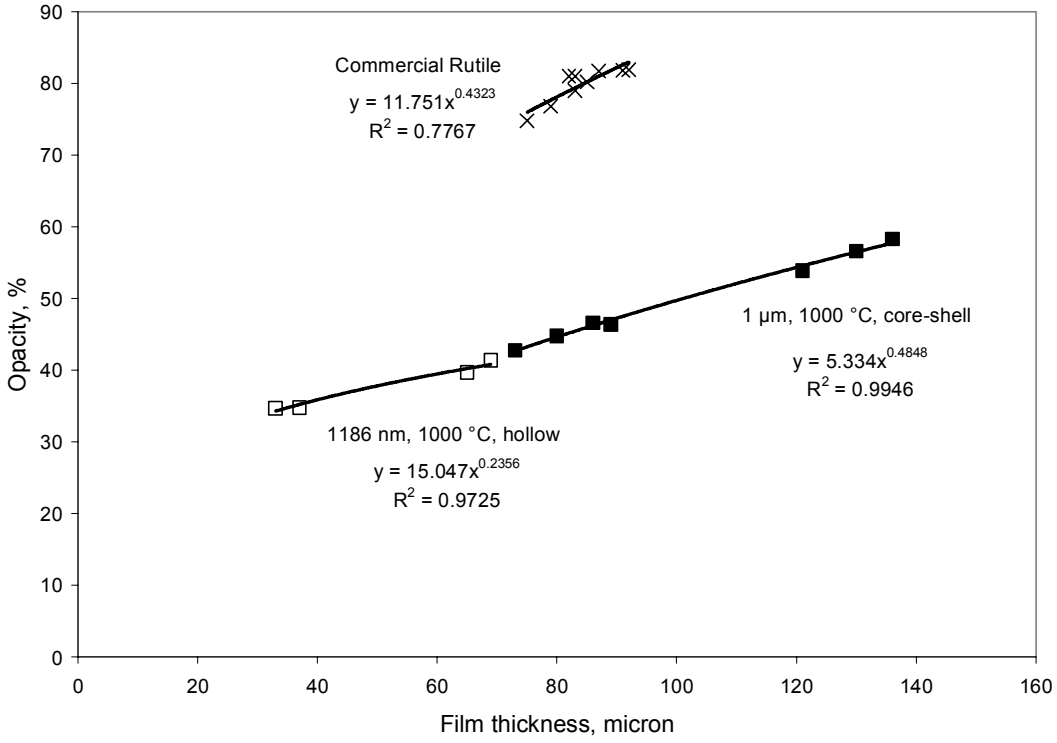

Figure 50: Opacity of cellulose films loaded with 3wt.% 1186 nm template core-shell and hollow particles calcined at 1000 °C.

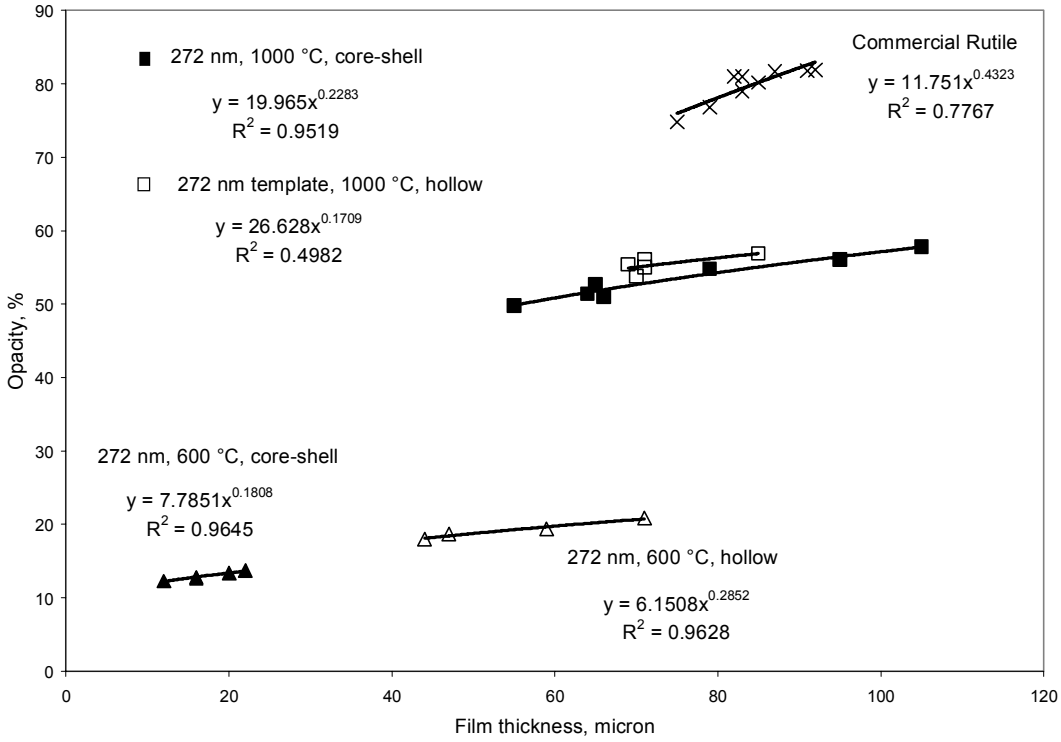

Figure 51: Opacity of cellulose films loaded with 3 wt.% 272 nm template core-shell and hollow particles calcined at 1000 °C.

While the core-shell and PEG filled hollow particles give similar opacities, the weight % of titania in the core-shell powders is less than for the hollow powders, which are 100 wt.% titania. Table 8 gives the weight content of titania for the core-shell particles. Taking the 1186 nm template particle calcined at 1000 °C as an example, the core-shell particle gives a similar opacity as the corresponding PEG filled hollow titania particle even though there is 41% less TiO_2 present in the film. Opacity is known to increase linearly with increasing pigment concentration under dilute conditions where dependent scattering does not play a role. Thus, the opacity of the film for the core-shell particles if the weight concentration of *titania* is increased to 3 wt%. was calculated and listed in Table 8. At this titania loading level, the opacity of the core-shell particles increases

dramatically. Thus, at equal titania loadings, the titania-silica core shell pigments have significantly more opacifying power than the hollow titania particles filled with PEG.

Table 8: Weight content of titania for core-shell particles and corresponding estimated opacity of a 70 μm thick cellulose film loaded with 3 wt% *titania*

	wt.% titania in powder	Experimental *Pigment* Loading in films, wt.%	Experimental *Titania* Loading in films, wt.%	Measured opacity for 3wt% *pigment* loading	Calculated opacity for 3wt% *titania* loading
272 nm template, 600 C	68.6	3	2.1	18.3	26.4
272 nm template, 1000 C	70.9	3	2.1	52.6	73.5
1186 nm template, 1000 C	58.7	3	1.8	41.8	70.3

The only difference between these two cases is the core material. This is an interesting finding since the refractive index of PEG is 1.467 and that of precipitated silica is reported to be in the same range depending on silica crystalline phase. Based on the findings in Chapter 4, which showed that the light scattering efficiency of polycrystalline TiO_2 nanoparticles changes as the crystal composition changes upon calcination, the relationship between crystal composition, calcination temperature, and light scattering efficiency was investigated for the silica cores. Figure 52 shows that the opacifying power of the silica templates dispersed in the cellulose/PEG matrix increases dramatically upon calcination and, for the case of the 272 nm template, calcination at 1000 °C gives significantly better opacifying power than calcination at 600 °C.

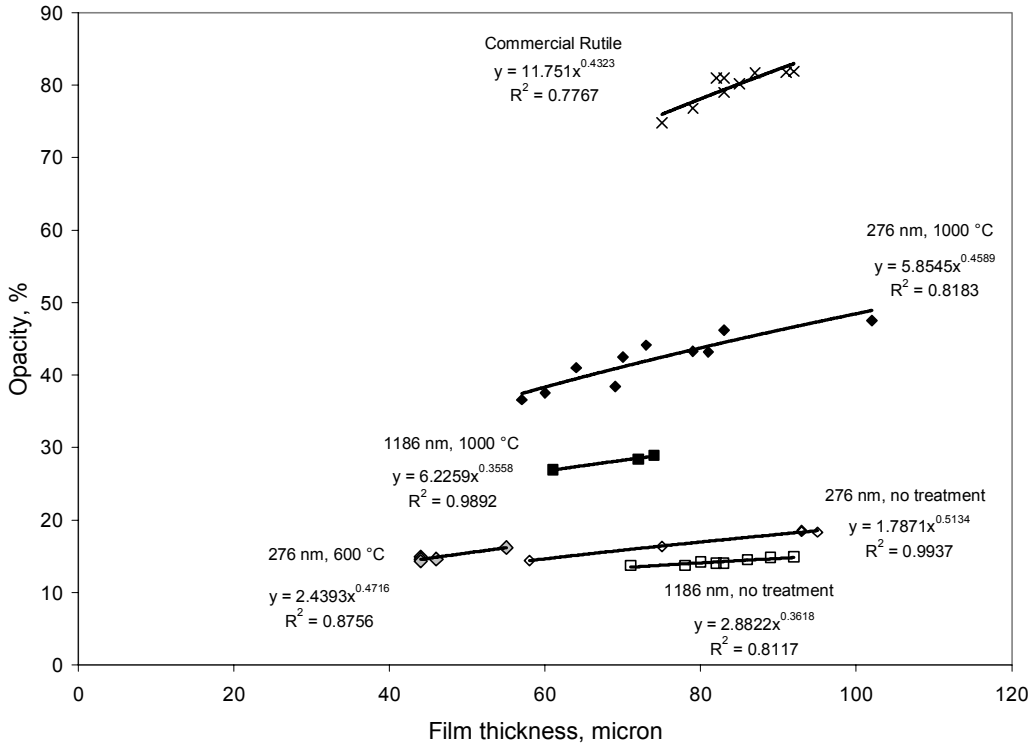

Figure 52: Opacity of cellulose films loaded with 3 wt.% silica templates

Table 9 gives the results of XRD analysis of the crystal structure of the silica powders. Indeed, the silica particles are polycrystalline in nature and the opacifying power increases as the character and phase composition of the crystals changes upon calcination. Thus it is concluded that the increased opacifying power of the silica-titania core-shell particles over the same titania shells filled with PEG results from light scattering taking place within the polycrystalline silica cores. No light scattering is expected to take place in the optically uniform liquid PEG core.

Table 9: Synthesized silica particle characterization and corresponding opacity for a 70 μm thick cellulose film loaded with 3 wt% pigment

	Crystalline Phase	Crystallite Size	Opacity
250 nm			
no heat	cristobalite low	1.4 ± 0	15.8
	cristobalite high	2 ± 1	
600 °C	cristobalite low	<1	18.1
	cristobalite high	49.2 ± 1.3	
1000 °C	cristobalite low	34.9 ± 2.6	41.1
	quartz	51.0 ± 1.4	
1 micron			
no heat	cristobalite low	1.7 ± 0	14.9
	cristobalite high	2 ± 1	
1000 °C	cristobalite low	27.6 ± 0.5	28.2
	quartz	24 ± 2	
Commercial TiO2	rutile	210	336

In order to investigate the light scattering properties of air filled hollow titania particles, the hollow particles calcined at 1000 °C were dispersed in a bleached fiber matrix which was highly pressed to remove air pockets. As shown in Figure 53 and Table 10 the hollow particles with the 1186 nm cavity size provide about 6% more opacity then commercial rutile, while the hollow particles with the 272 nm cavity provide about 3% less for a film thickness of 135 μm.

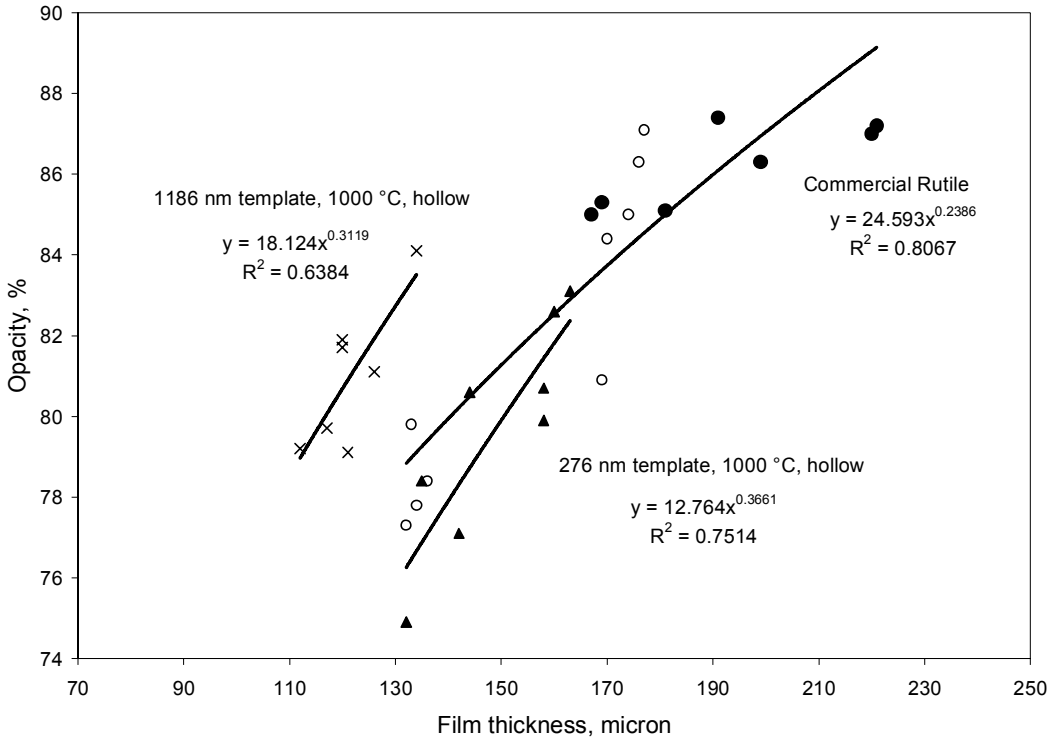

Figure 53: Opacity of pressed fiber films loaded with 3 wt.% hollow titania particles

Table 10: Opacity for a 135 μm thick bleached fiber matrix loaded with 3 wt% hollow pigment

	Structure	Opacity @ 135 μm
272 nm template 1000 °C	Hollow Polycrystalline Rutile	76.9
1186 nm template 1000 °C	Hollow Polycrystalline rutile	83.7
Commercial	Rutile	79.2

These results contradict the theoretical light scattering results calculated by Johnson et al for hollow titania spheres in a cellulose matrix (95). Johnson et al. used the well-known program BHCOAT which calculates the light scattering efficiency of isolated core-shell particles based on Mie theory (64). Their results show that the light scattering efficiency for a hollow titania particle with a shell thickness of 10% of the particle radius is dramatically less than that for a solid optimally sized rutile particle, regardless of cavity size. However, there is a decisive difference between the hollow titania particles considered in this study and those modeled using Mie theory. Mie theory assumes an optically uniform titania shell characterized by a single refractive index throughout and lack of any inclusions including pores, crystals and grain boundaries. However, the hollow titania shells synthesized here are composed of many birefringent rutile crystals and the TEM and SEM images in Figures 5 and 6 suggest the presence of pores. As discussed in Chapter 4, the strong birefringence of the rutile crystal is characterized by two different refractive indices at a given wavelength depending on the direction of propagation and polarization of incident light. Thus when a polycrystalline material is composed of randomly oriented crystallites (as is the case here), light propagating in a particular direction will pass through many crystals with different indices of refraction and light scattering will occur through reflection and refraction. A similar phenomenon results in the presence of pores. The complex light scattering patterns that result in the polycrystalline shell through the multitude of reflections and bendings of the light path at grain boundaries are expected to become even more complex and substantial as the many light paths reflect and refract upon entering the air filled core and bounce around. The

reason why the ~1 μm cavity size gives more light scattering than the ~250 nm size is not fully understood at this point.

5.4 Conclusion

Polycrystalline titania-silica particles were synthesized with varying titania and silica phase compositions. Hollow titania particles were synthesized by dissolution of the silica core. The light scattering efficiency of the pigments were evaluated by measuring the opacity of optically uniform cellulose nanowhisker/PEG films loaded with 3 wt% pigment. The opacifying power of the rutile titania core-shell particles was found to be superior to the PEG filled hollow particles at equal *titania* loadings in the film. The light scattering efficiency of the polycrystalline silica cores was found to depend on calcination temperature and crystal structure. It is suggested that the increased opacifying power of the silica-titania core-shell particles over the same PEG filled titania shells results from light scattering taking place within the polycrystalline silica cores. Hollow rutile titania particles with a 1186 nm cavity size provide about 6% more opacity then commercial rutile, while hollow particles with 272 nm cavity provide about 3% less in a highly pressed bleached fiber matrix.

CHAPTER 6

THE SHAPE DEPENDENCE OF CORE-SHELL AND HOLLOW TiO_2 NANOPARTICLES ON COATING THICKNESS DURING LAYER-BY-LAYER AND SOL-GEL SYNTHESIS

Abstract

Titania core-shell and hollow nanoparticles with different aspect ratios were synthesized using layer-by-layer assembly and sol-gel nanocoating methods with cellulose nanowhiskers as the template. During coating layer growth, the shape of the nanoparticles did not maintain the shape of the high aspect ratio template, as previously assumed. The shape of the coated particles is a function of the coating thickness. It is suggested that the overall particle shape and aspect ratio of the nanoparticles are tunable by choosing an appropriate template and coating thickness in layer-by-layer or sol-gel templating synthesis. The nanorods and hollow titania particles synthesized by these methods were characterized by TEM, SEM, and XRD.

6.1 Introduction

Interest in the fabrication of inorganic nanoparticles with controlled size, shape and hollow interior is driven by their potential unique and tunable physical properties and the desire to engineer advanced bulk materials from nanoscale building blocks (118). The four most relevant questions in this research area are (i) how can nanostructures that have controlled morphology be reasonably synthesized, (ii) what are the intrinsic and potentially unique physical properties of the nanostructures, (iii) how can three-dimensional periodic lattices be reasonably fabricated from such nanoparticles and (iv)

what unique properties or functionality result from such organized structures (119, 120). In recent decades, there has been a lot of interest in the morphological control and organization of titanium dioxide nanoparticles in particular because of their use in photocatalysis, controlled drug delivery, photonic crystals, and pigments (121-125). Both single crystal and polycrystalline titania nanostructures with different shapes, such as bullet, diamond, short and long rods, branched rods, and ellipsoids have been synthesized (126, 127). From templating methods like sol-gel and layer-by-layer assembly, hollow polycrystalline titania structures have been made with shapes limited to the sphere, ellipsoid, and tube (25, 55-57, 128). While conceivably the range of different shapes achieved from the nanocoating methods is infinite, a practical limitation has been the availability of uniform uniquely shaped colloidal templates. In the past, it has been widely believed that the shape and void size of the hollow particles is exactly determined by the nanosized template (128-130) for both sol-gel and LBL. Studies appearing to uphold this belief include the coating of sphere (d = 150 nm –1 μm) (25, 42, 131), ellipsoid (1.08 x 0.78 μm)(128), and rod-shaped (20-65nm x 1 μm) (55-57) templates. However, this report shows that the shape of high aspect ratio nanosized colloidal templates is not actually preserved during synthesis of thick coating layers. In fact, the shape of the coated particles is a function of the coating thickness, as shown by optical microscopy. We suggest that the overall particle shape *and* cavity shape of coated nanoparticles is tunable by choosing an appropriate template and coating thickness.

6.2 Experimental

6.2.1 Materials

Cotton pulp (Procter & Gamble Cellulose), sulfuric acid (EM Science), poly(diallyldimethylammonium chloride) (PDADMAC, 20% solution, MW 100-200K, Aldrich), sodium chloride (99.999%, Aldrich), titanium(IV) bis(ammonium lactato) dihydroxide (TALH, 50% solution, Aldrich), titanium(IV) butoxide (97%, Aldrich) and potato starch (National Starch and Chemical Co.) were used without further purification. Water used for layer-by-layer assembly was obtained from a Nanopure ultrapure water system with a resistivity of about 18 MΩ cm.

6.2.2 Preparation

An aqueous suspension of cellulose whiskers was prepared following the procedure outlined by Edgar and Gray (132)[19]. Cotton pulp was hydrolyzed with 64 wt % sulfuric acid at 45 °C for 45 min. Prior to hydrolysis, the cotton pulp sheets were torn into small pieces and fed through a Wiley mill (Arthur H. Thomas Co.) to pass through a 1 mm mesh. Typically, 40 g of ground cotton with 6% moisture was treated with 700 mL of sulfuric acid solution. Immediately following hydrolysis, the suspension was diluted 10-fold with water to quench the reaction. The suspension was concentrated by allowing the solids to settle overnight and then collecting the solids from solution with minimal amount of water. Excess acid was removed by three washing and centrifugation cycles at 25,900 RCF (Relative Centrifugal Force) for 30 min. The sample was then dialyzed (Spectra/Por membrane, MWCO 50K) against water for several days until the water

achieved a neutral pH. To separate flocculated whiskers, the suspension was continuously sonicated (Heat Systems-Ultrasonics W-385 sonicator) for 35 min while cooling in an ice bath. The suspension was allowed to stand over a mixed bed resin (Sigma TMD-8) for 48 h and then filtered through hardened ashless filter paper (Whatman, 541). The concentration of the final aqueous suspension was 2.05% by weight. The yield of cellulose whiskers was about 35%. For imaging, cellulose whiskers were dried on a carbon coated lacey TEM grid and stained with 25% uranyl acetate solution for 30 minutes. TEM micrographs were obtained at 100kV using the 3rd aperture and the defocus contrast technique. The micrographs show the whiskers to be uniform in thickness but with a wide distribution in length, as expected.

Titania core-shell and hollow nanoparticles were prepared from cellulose whiskers as the colloidal template using two nanocoating methods: layer-by-layer electrostatic assembly and sol-gel. For layer-by-layer assembly, a dilute solution of cellulose whiskers (2.0 mg/mL) was prepared by diluting 7.32 g of the as prepared whisker solution (2.05 wt.-%) to 75 mL. Then, 150 mL of PDADMAC (0.25 mg/mL, containing 0.125 M NaCl) was added. PDADMAC was allowed to adsorb for 15 minutes. Excess PDADMAC was then removed by three repeated centrifugation and washing cycles (RCF and time varied with each layer). The solids collected after removing the supernatant from the final centrifugation step were diluted to 75 mL. Then, 150 mL of TALH (2.5 wt.-%) was added and allowed to adsorb for 15 minutes. Excess TALH was removed by three repeated centrifugation and washing cycles (RCF and time varied with each layer).

Titania/PDADMAC coatings were formed on the cellulose whiskers by refluxing the polyelectrolyte-coated whiskers in aqueous solution for 24 h at 100 °C.

Hollow titania nanoparticles were produced by calcination of the polyelectrolyte coated cellulose whiskers. In order to prevent nanoparticle sintering so that the shape of discrete particles could be observed, the coated whiskers were adsorbed on a starch matrix surface by mixing them with uncooked starch particles in water before calcination. Experimentally, a solution of cellulose whiskers coated with 10 PDADMAC/TALH bilayers was first lyophilized. An aqueous solution containing 0.25 g of the dried coated particles and 2.5 g of potato starch was then prepared and sonicated for 15 minutes while cooling in an ice bath to allow the coated nanoparticles to adsorb separately onto the starch surface. The dispersion was then vacuum-dried under low temperature. The resulting solid matrix was then calcined at 525 °C for 4 hours in air.

For sol-gel synthesis, whiskers were coated with titania using titanium tetrabutoxide (TBT) as the titanium dioxide precursor following the continuous coating technique of Liu et al (116). Experimentally, 0.06 g lyophilized cellulose whiskers were added to 100 mL of ethanol. The mixture was sonicated in an ice bath for roughly one hour to disperse the whiskers. TBT (0.009 M) was then added to the solution followed by water added dropwise under stirring for four hours at a rate of 0.003 mL/min. The solution was then refluxed at 80 °C for 1.5 hours to ensure complete condensation of the titania shell. The core-shell particles were then collected by three repeated centrifugation and washing cycles using ethanol and dried under vacuum at 100 °C. These particles were calcined at 900 °C for 10 minutes to obtain hollow titania particles. Unlike the LBL coated particles,

significant sintering is not observed for sol-gel coated particles during calcination. Therefore, the starch matrix was not necessary to prevent sintering.

6.2.3 Characterization

Electrophoretic mobilities of the particles in pure water were measured with a Malvern 3000 Zetasizer. Transmission electron microscopy (TEM) was carried out with a JEOL 100 CX II microscope at 100kV. X-ray diffraction (XRD) of the titania/cellulose composite sample was obtained using an X'Pert Pro Alpha-1 diffractometer with an incident beam monochrometer allowing only the $K\alpha_1$ component of Cu radiation. All other x-ray diffraction patterns were recorded on a Philips PW 1800 diffractometer with Cu Kα radiation. Scanning electron microscopy (SEM) was performed using a LEO 1530 thermally-assisted field emission (TFE) microscope at 3 kV. The samples were lightly sputter coated with Au/Pd prior to observation. The aspect ratio of the individual titania core-shell particles and their corresponding whisker templates were manually measured directly from the TEM micrographs. The whisker template within a core-shell particle appears transparent in the micrograph, while the coating layer appears dark. Thus, for each core-shell particle, the length and width of the cellulose whisker can be directly measured along with the length and width of the coated particle itself from the TEM images. For a coated particle with uneven coating thickness along its sides and tips, the length and width of the particle were measured at their thickest points.

6.3 Results and Discussion

Titania core-shell and hollow nanoparticles with different aspect ratios were obtained using the layer-by-layer assembly and sol-gel coating methods with cellulose whiskers as a template. Cellulose whiskers, with their inherently large distribution of aspect ratios, were chosen in order to study the dependence of coated particle shape on the aspect ratio of the template. Figure 54 shows a TEM image of the cellulose whiskers with their polydispersity in length.

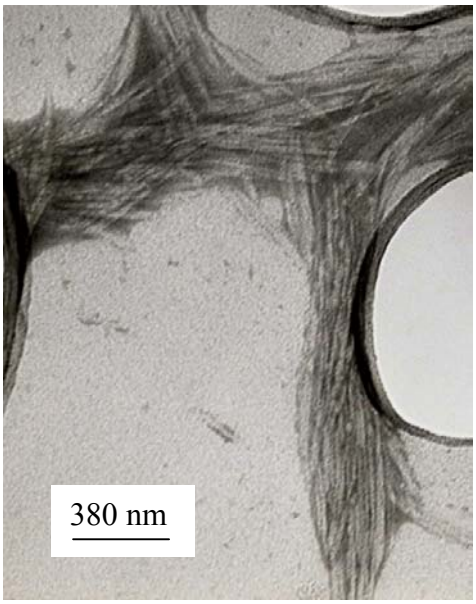

Figure 54: TEM image of cellulose whisker template coated with 25% uranyl acetate negative stain.

Cellulose whiskers have a negative electrostatic layer surface that gives stable dispersions in aqueous solution, an important prerequisite for colloidal templates. For layer-by-layer assembly, the whiskers were coated successively with layers of a positively charged

polymer (PDADMAC) and a negatively charged titania precursor (TALH). Unlike titania alkoxides that hydrolyze rapidly in the presence of water, TALH is stable at ambient temperature in neutral solution (25). This prevents the conversion of TALH to titania at this stage of preparation. Electrophoresis measurements monitored the surface charge reversal with adsorption of each oppositely charged layer. As shown in Figure 55a, the zeta potential varied between +40 mV (PDADMAC layer) and –40 mV (TALH layer) upon adsorption of 10 polyelectrolyte bilayers. The zeta potential of uncoated cellulose whiskers was about –30 mV. Electrophoresis measurements were also used to determine the concentrations of PDADMAC and TALH giving maximum adsorption. The concentration for the maximum adsorption of PDADMAC was determined to be 0.06 mg/mL in a solution containing 0.1 M NaCl. For TALH measurements, the cellulose whiskers were first saturated with one layer of PDADMAC to obtain a positively charged surface before adsorption of TALH. Figure 55b indicates that maximum adsorption of TALH occurs at a solution concentration of 8 mg/mL TALH. At this point, the particle surfaces are saturated. Increasing the concentration of TALH beyond this point does not result in the adsorption of more TALH and zeta potential remains constant.

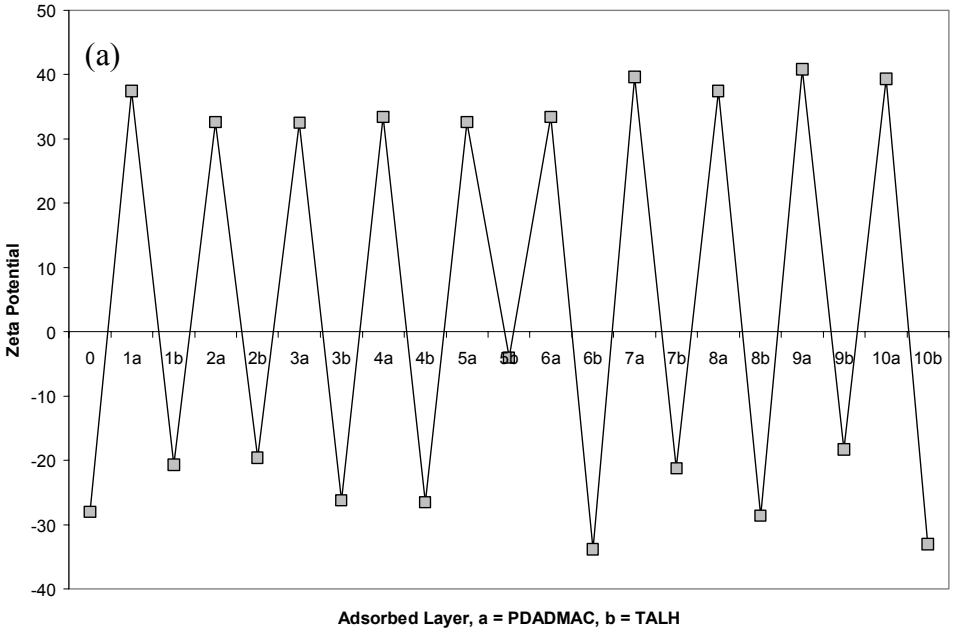

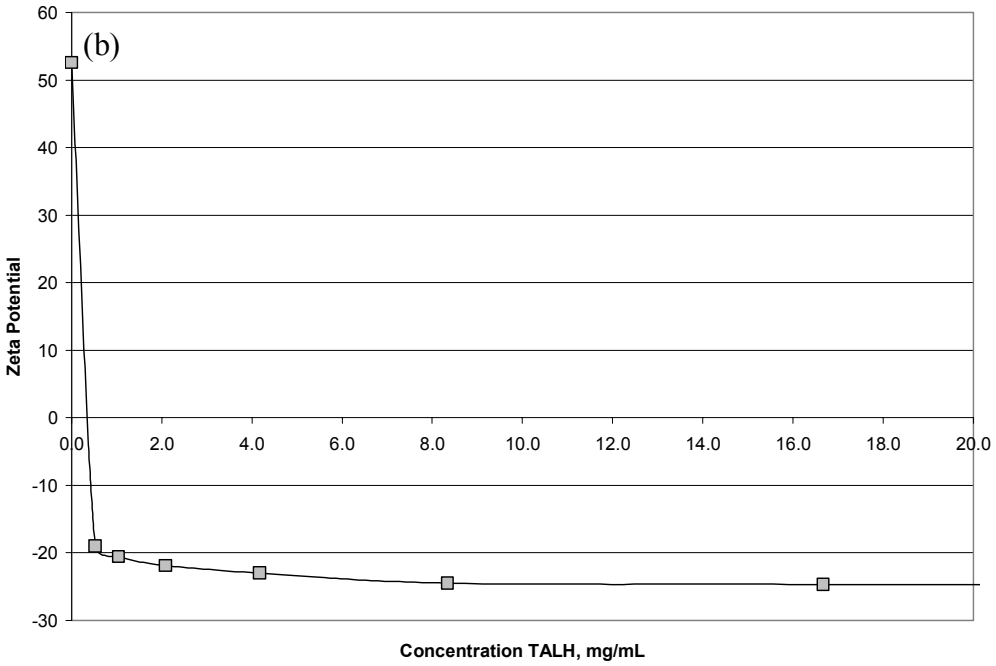

Figure 55: (a) Electrophoretic mobility reversal of cellulose whiskers coated with alternating layers of PDADMAC and TALH and (b) electrophoretic mobility of cellulose whiskers saturated with one layer of PDADMAC followed by adsorption of TALH.

Previously, it has been assumed that particles produced by LbL assembly replicate the shape of the colloidal template, regardless of coating thickness. While this appears to be the case for very thin coatings and for spherical nanoparticle templates and micron-sized nonspherical templates, the TEM images in Figure 56 clearly show that for high aspect ratio templates with sub-micron dimensions, the shape of the nanoparticles no longer maintains the shape of the template as the number of adsorbed polyelectrolyte bilayer increases. The aspect ratio of the coated particles decreases significantly as the number of bilayer increases.

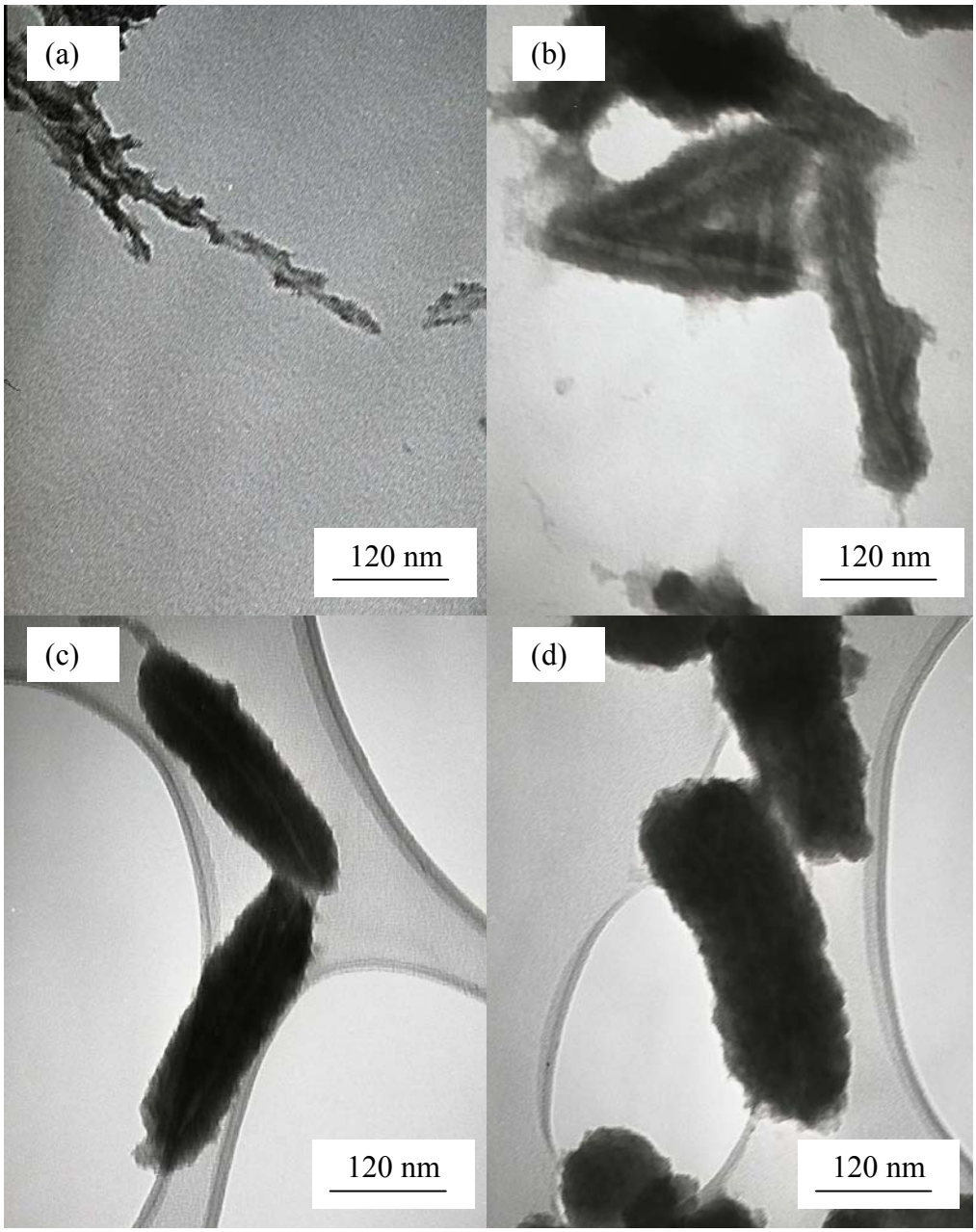

Figure 56: TEM images of PDADMAC/TALH coated cellulose whiskers from LBL method with (a) 2 bilayers, (b) 6 bilayers, (c) 8 bilayers, and (d) 10 bilayers.

The SEM images in Figure 57 further illustrate how the aspect ratio changes with number of adsorbed bilayers. In addition, Figure 57b shows that adsorption of 10 bilayers onto

the cellulose whiskers yields particles with a wide range of shapes, depending on the aspect ratio of the template.

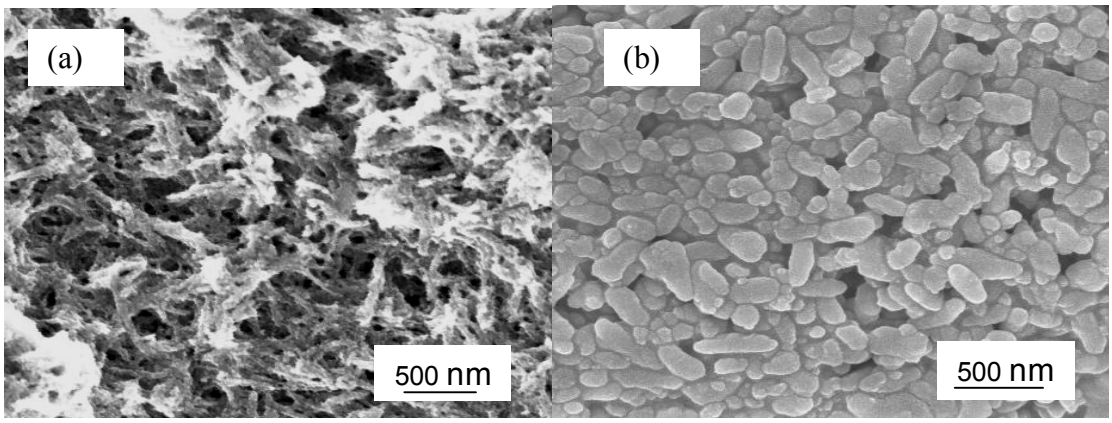

Figure 57: SEM images of titania/PDADMAC coated cellulose whiskers derived from LBL method with (a) 5 PDADMAC/TALH layers and (b) 10 PDADMAC/TALH layers.

It is clear from Figure 56 that the tendency of adsorption of the polyelectrolytes on the whiskers' tip and flat surfaces are not equal. The coated layer is thicker on the sides than at the tips. The same adsorption tendency was observed for cellulose whisker templates coated using the sol-gel method, as shown in Figure 58.

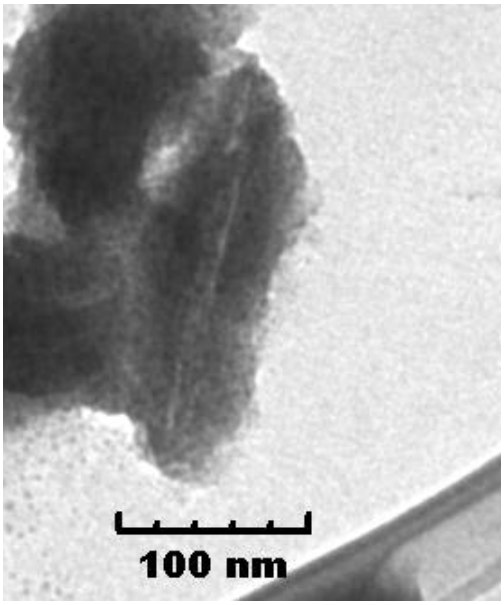

Figure 58: TEM image of titania/cellulose nanoparticle derived from sol-gel nanocoating method.

During sol-gel synthesis, oligimers are adsorbed from solution and can be thought to build up in a layered fashion. From these observations, the aspect ratio of the particles as a function of layer thickness, for a given template, can be calculated. For a cylindrical particle with length L and diameter D, the aspect ratio, r, of the particle can be simply calculated from r = L/D. If the cylindrical particle is coated and the average thickness of each bilayer (including both PDADMAC layer and TALH layer) for LBL or each oligomer layer for sol-gel on the tips is h_L, and the thickness of each bilayer on the sides is h_w, the aspect ratio becomes

$$r = \frac{L^0 + 2n_L h_L}{D^0 + 2n_w h_w} = \frac{r^0 + \frac{2n_L h_L}{D^0}}{1 + \frac{2n_w h_w}{D^0}} = \left(\frac{D^0}{D^0 + 2n_w h_w}\right) r^0 + \frac{2n_L h_L}{D^0 + 2n_w h_w}$$

Equation 19: Aspect ratio in terms of layer thickness

Where n_w *and* n_L *are* the numbers of layers on the side and tip respectively, and superscript *o* represents the uncoated template state. The average diameter of the cellulose whisker templates, D^o, is 8 nm, as estimated from TEM measurements. Equation (1) indicates that the aspect ratio, *r*, of the coated particles has a liner relationship with the aspect ratio of the template. Figure 59 shows a plot of the aspect ratio of TiO_2 coated particles, *r,* obtained experimentally from LBL and sol-gel methods, versus the aspect ratio of template, r^o. For the purpose of comparison, the data calculated from Equation (1) by assuming $n_L h_L = n_w h_w$ (an even coating on the tips and sides) are plotted as dot line. For the LBL method, 10 bilayers were deposited, and for sol-gel method, the coating conditions were given in the experimental section. Clearly, the experimental data do not follow the even coating curve. For LBL, the best liner fit from the experimental data shown in Figure 6 gives a slop of 0.0922 and an intercept of 0.2138. By applying this slope and intercept to Equation (1), a total coating layer thicknesses of $n_w h_w$ = 39.4 nm and $n_L h_L$ = 9.3 nm were obtained for the side and tip, respectively. Similar results were found for the sol-gel method, with the best fit line to the experimental data giving total coating thicknesses of $n_w h_w$ = 28.9 nm and $n_L h_L$ = 18.5 nm at our experimental conditions.

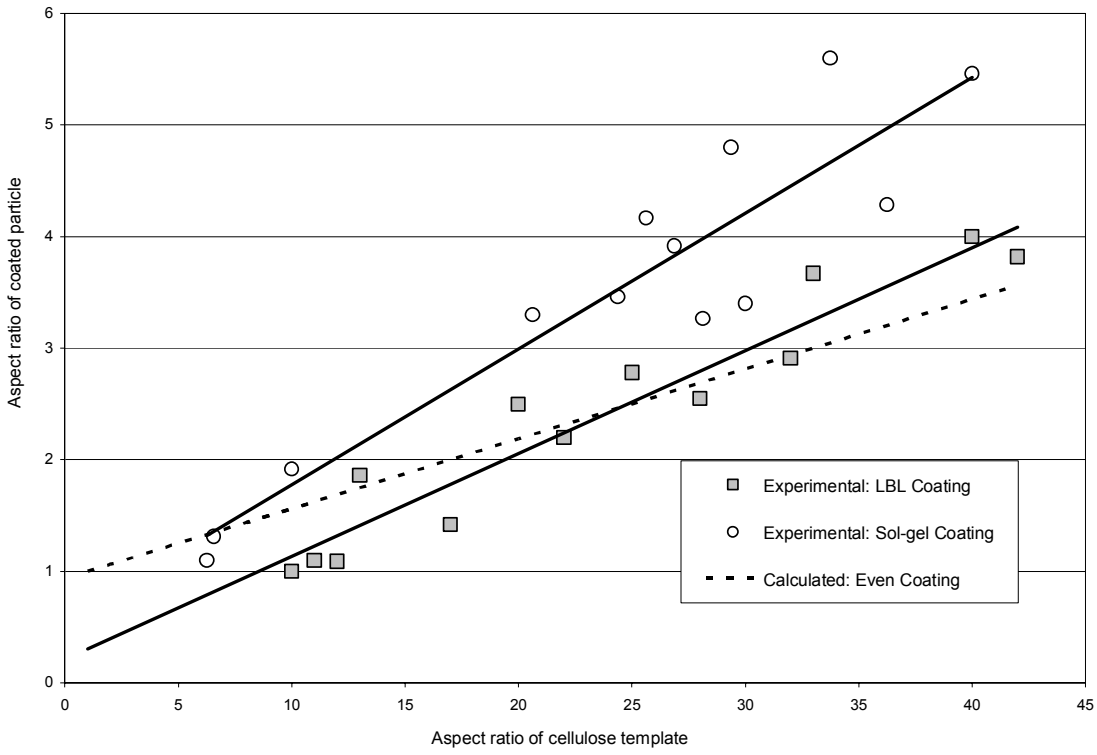

Figure 59: Dependence of aspect ratio of coated particles derived from LBL and sol-gel on aspect ratio of cellulose whisker template for a fixed coating thickness. For the LBL method, 10 bilayers were deposited, and for sol-gel method, the coating conditions were given in the experimental section.

From a thermodynamic point of view, the phenomenon of uneven coating may be explained by total surface free energy effects. It is well known that the total surface energy play a dominating role during the particle growth as particle enters the nanoscale. By reducing specific area, the total surface free energy of particles is reduced. Because spherical particles, with an aspect ratio of 1, have the smallest specific area, all particles will try to minimize their surface free energy by reducing their aspect ratio during coating growth. This surface area minimization is illustrated here. Thus, for more than just a nominal coating thickness, in the nanoscale, sol-gel and LBL coating methods will not preserve the template shape if the template is not spherical. That the shape of the final

product is a function of the template aspect ratio and the number of coating layers suggests that the shape of coated nanoparticles is actually tunable by choosing a desirable template and coating thickness for nanocoating methods involving the adsorption of polyelectrolyte or oligimer species from solution such as sol-gel and layer-by-layer. . It is believed that this principle can also be applied to fabricate other types of nanoparticles or films. Figure 60 illustrates how the shape of the coated particles changes as the coating layer increases for high aspect ratio templates as shown experimentally as well as the shapes anticipated for a star-shaped template. This diagram suggests that the cavity shape as well the particle shape can be tuned. Tailoring the cavity shape of hollow nanoparticles may lead to interesting optical and other properties.

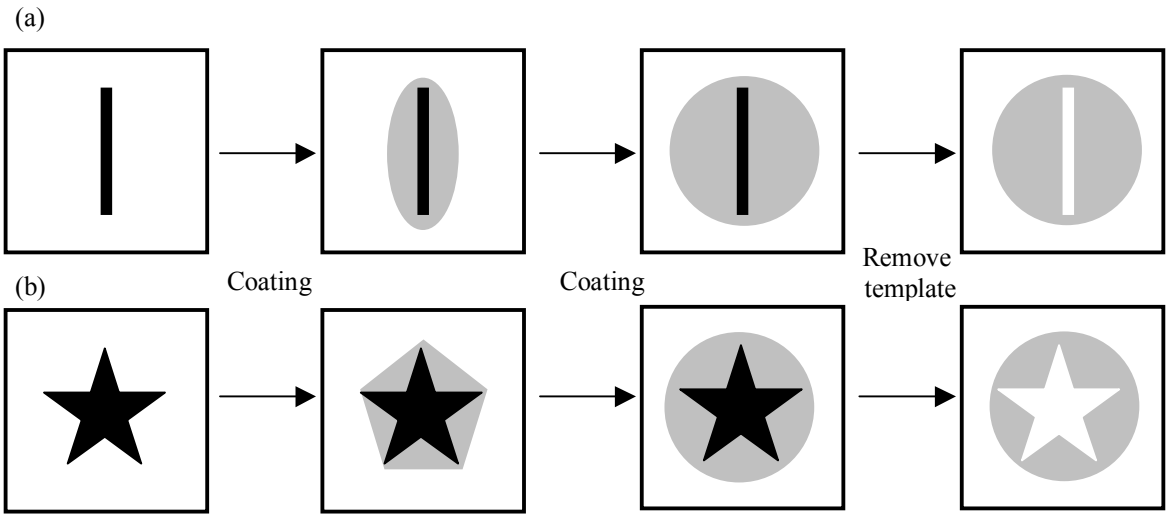

Figure 60: Illustration of suggested dependence of nanoparticle shape on coating thickness for (a) high aspect ratio template and (b) star-shaped template.

It should also be noted that the surface energy may not be a critical parameter for controlling the particle geometry if the particle size is big. Therefore, the template shape

may be preserved during the LBL coating for large particles, but it is not the case for nanoparticles.

Figure 61 A and B shows that, for the LBL method, the particle shape determined by the uneven adsorption of polyelectrolytes is conserved when converting the titania precursor to crystalline TiO_2 for both core-shell particles and hollow particles.

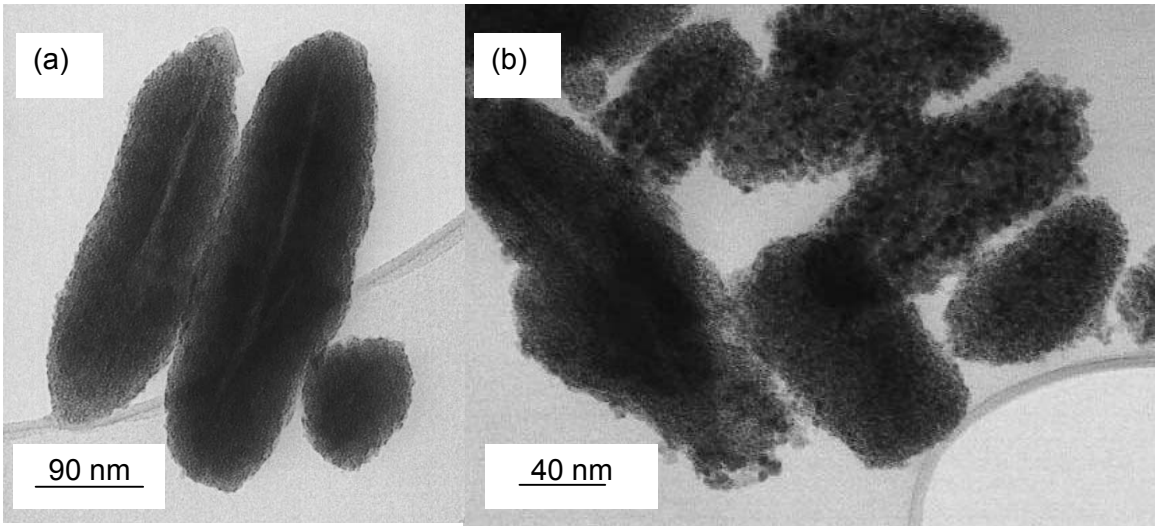

Figure 61: TEM image of (a) titania/cellulose nanoparticles and (b) hollow titania nanoparticles after calcination derived from LBL method with 10 TALH/PDADMAC bilayers.

The cavity running through the center of the hollow particles is clearly visible in the SEM image shown in Figure 62.

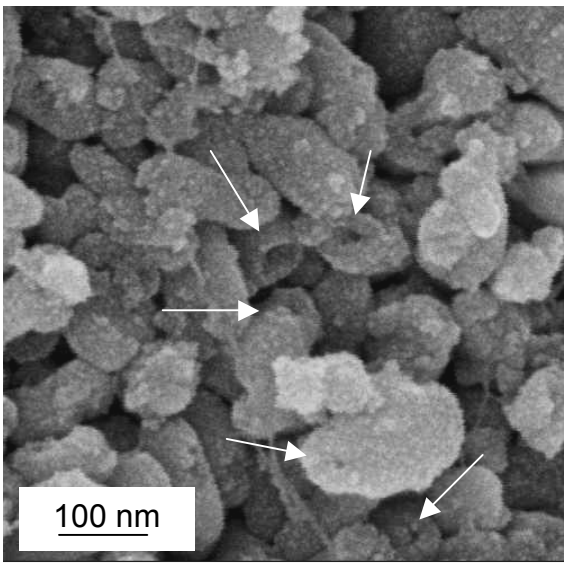

Figure 62: SEM image of intentionally broken titania nanoparticles obtained after calcination. Arrows indicate hollow channel running through center of particles.

Figure 63 presents the XRD patterns of the core-shell and hollow titania nanoparticles. The XRD pattern for the composite nanoparticles clearly shows crystal peaks for both titania and cellulose. The titania shells of these composite particles contain amorphous, anatase, and rutile phases. Figure 9b shows that the hollow titania nanoparticles after calcination are of the anatase phase.

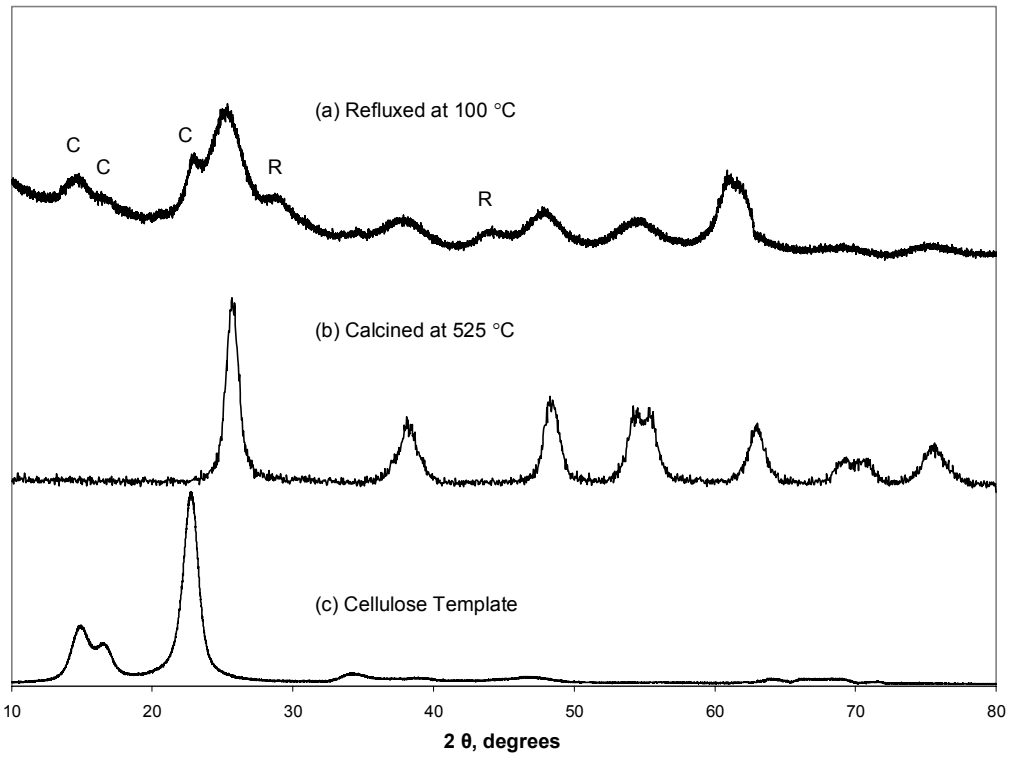

Figure 63: X-ray diffraction patterns of (a) titania/cellulose composite particles, (b) hollow particles calcined at 525 °C, and (c) cellulose whiskers template.

6.4 Conclusion

Cellulose whiskers with a wide distribution of aspect ratios were used as a colloidal template to form titania core-shell and hollow nanoparticles with tunable aspect ratio via layer-by-layer assembly and sol-gel nanocoating techniques. It was found that the shape of the cellulose whisker template was not maintained during growth of the coating layer and that the aspect ratio of the synthesized titania particles can be tuned by varying the coating thickness and/or the aspect ratio of the template. In addition, the overall particle shape and cavity shape can be simultaneously tuned by choosing an appropriate template and coating thickness. It is believed that for particles in the nanoscale, the mechanism

allowing the shape tunablity is the minimization of surface area, and therefore surface free energy, during coating growth.

CHAPTER 7

FORMATION OF CELLULOSE NANOPARTICLES AND THEIR ENCAPSULATION ON ORGANIC PARTICLES BY CONTROLLED PRECIPITATION

Abstract

Inorganic-cellulose core-shell and hollow cellulose nanoparticles were prepared by self-encapsulation with regenerated cellulose via precipitation of cellulose in a polyacrylic acid hydrogel layer surrounding inorganic particle templates in 4-Methylmorpholine N-oxide (NMMO) monohydrate solution. The hydrogel layer surrounding the inorganic particle surface plays a decisive role in core-shell formation. The core-shell nanostructures were characterized using TEM, SEM, and X-Ray Diffraction. The cellulose shell was found to be composed of ~30 nm cellulose spheres or nodules. Individual regenerated cellulose nanoparticles were also synthesized by addition of nonsolvent under agitation to dilute solutions of cellulose dissolved in NMMO. The effects of addition rate of water (the non-solvent) on the nanostructure, morphology and crystallinity of the regenerated cellulose nanoparticles were studied. Results indicate that the faster the water addition rate, the smaller the cellulose nanoparticles formed. In addition, only cellulose-I crystal phase was found for water added all-at-once, while both cellulose-I and cellulose-II were obtained for water added drop-by-drop. The mechanism of crystal phase formations via controlled addition rate of non-solvent is also discussed.

7.1 Introduction

Micro- and nanometer-sized capsules and core-shell particles have found applications in diverse areas such as drug delivery (133-135), polymer composites (136-138), foods and drinks (139, 140), coatings and paint (141, 142), sensors (143, 144), and papermaking (3, 104). Many encapsulation methods such as *in situ* polymerization (145, 146) and layer-by-layer assembly (147, 148) have been developed using a range of functional or biodegradable encapsulating polymers (149-151). Biodegradable or bioinert polymers are especially interesting for drug delivery and biosensor applications. Polylactic acid (PLA), polyhydroxybutyrate (PHB), and poly(ε-caprolactone) are examples of biodegradable polymers used in encapsulation of drugs or nanosensors. Cellulose is the most abundant natural polymer and is considered an almost inexhaustible source of raw material for environmentally friendly and biocompatible products. Cellulose can form a hydrogel when it absorbs waters, and can form hydrogen bonds with many biomaterials and engineering substrates. Therefore, successful encapsulation of nano- or micro-particle surfaces with cellulose have great potential for making new functional materials with wide applications including bioinert biosensors, microcapsules for drug delivery, fillers with strong hydrogen bonding ability, etc. However, pure cellulose has not previously been used as a discrete coating material because of the poor processibility of cellulose in water and most common organic solvents.

One of only a few technically feasible solvents, NMMO (4-Methylmorpholine N-oxide) has been used for several decades to commercially manufacture cellulose fibers, films,

membranes, and beads (152, 153). Advantages of NMMO-based cellulose processing include relative simplicity and small environmental footprint as the solvent is non-toxic, biodegradable, and almost completely recycled during the process (99.6-99.7%) (108). Extensive research has been performed to characterize and mechanistically explain the development of the unique morphology of regenerated cellulose fibers and membranes precipitated from NMMO solution (112, 154-157). Light scattering studies have shown that the cellulose in NMMO monohydrate solution is not in a single molecule form, but exists as micelle-like cellulose aggregates (109, 111, 112, 158). In this study we show that the cellulose aggregates can uniformly encapsulate inorganic colloidal templates, giving unique core-shell structured materials. We also show that the regenerated cellulose morphology, crystalline phase, and crystallinity are closely related to the addition rate of a non-solvent under agitation.

7.2 Experimental

7.2.1 Materials

Schalenahedral precipitated calcium carbonate (PCC, Albacar HO, Minerals Technologies) and rutile titanium dioxide (Millennium Chemicals) were donated and lyophilized. Cellulose powder (medium fibers from cotton linters, Sigma), NMMO (50% w/w aqueous solution, Alfa Aesar), poly(acrylic acid, sodium salt) (PAA, MW 5,100, Aldrich), tetraethyl orthosilicate (TEOS, 98 wt. %, Aldrich), ammonia (29 wt.-%, VWR), hydrochloric acid (37%, Aldrich), and ethanol (VWR) were used without further

purification. Water was obtained from a Nanopure ultrapure water system with a resistivity of about 18 MΩ cm.

7.2.2 Preparation

The monodisperse colloidal silica template with a diameter of ~270 nm was prepared by hydrolysis of TEOS in ethanol in the presence of water and ammonia following the Hsu *et al* and Giesche [32,33]. Water (53.307 g) and ammonia (29 wt. %, 26.441 g) were added to 330 mL ethanol and heated to 40 °C under reflux. TEOS (98%, 26.573 g) was also heated to 40 °C in a separate, closed container. TEOS was then added to the ethanol solution under vigorous stirring. Fifteen seconds later, the stirring was reduced to low and continued for 1 hour at 40 °C. The resulting solids were isolated by three centrifugation (25,900 RCF for 5 min) and ethanol washing cycles and lyophilized.

Regenerated cellulose nanospheres were synthesized as illustrated in Schematic 1a. A dilute solution of cellulose dissolved in NMMO was prepared by first combining 0.5 g of cellulose powder with 95.5 g of aqueous NMMO (50 wt. %). This mixture was then heated in a rotary evaporator under vacuum at 60 °C for 20 minutes followed by 95 °C for 20 minutes. During heating, bulk water was removed from solution and the cellulose dissolved in NMMO. Water (50 mL) was then added to the solution at three different rates: (i) all-at-once, (ii) drop-by-drop at 5 mL/min, and (iii) drop-by-drop at 0.5 mL/min. The resulting solids were isolated by three centrifugation (25,900 RFC for 2.5 min.) and washing cycles. For imaging, cellulose nanospheres were dried on a carbon coated TEM grid and stained with 4% uranyl acetate solution for 3 minutes.

Regenerated cellulose coated nanoparticles were synthesized using several different nanoparticle templates including TiO_2, silica, and PCC in powder form. The inorganic particles were dispersed in aqueous suspension (1 wt.%) in the presence of 0.5 wt. % PAA. The suspensions were sonicated up to 45 minutes to ensure complete dispersion. An aqueous suspension of cellulose powder and NMMO was prepared by combining 0.5 g of cellulose powder with 95.5 g of aqueous NMMO (50 wt.%). Three grams of the 1 wt.-% nanoparticle template suspension were combined with 20 g of the cellulose/NMMO suspension and briefly sonicated. This mixture was then heated in a rotary evaporator under vacuum at 60 °C for 20 minutes followed by 95 °C for 20 minutes. During this heating process, the cellulose was dissolved and the template becomes encapsulated by regenerated cellulose (the mechanism will be discussed later). To isolate these core-shell particles from residual dissolved cellulose, the solution was transferred to an oil bath and maintained at 95 °C under mechanical stirring. Water was then added to the solution in excess (about 20 ml) all-at-once to precipitate the residual cellulose into nanoparticles. Because the core-shell particles are much bigger than pure cellulose nanoparticles, they were separated from these cellulose nanospheres by filtering the suspension through a 200 nm Millipore membrane. The core-shell particles remaining on the filter paper were then washed several times with distilled water and stored as a dilute aqueous solution. Hollow cellulose nanocapsules were prepared by dissolving the core of cellulose coated PCC by lowering the pH of the suspension to 5 with hydrochloric acid and allowing the PCC to dissolve for 48 hours.

7.2.3 Characterization

Transmission electron microscopy (TEM) was carried out with a JEOL 100 CX II microscope at 100kV. X-ray diffraction (XRD) was carried out using an X'Pert Pro Alpha-1 diffractometer with an incident beam monochrometer allowing only the $K\alpha_1$ component of Cu radiation. XRD spectra were analyzed using JADE 7 software from Materials Data. Crystallinity was estimated from the equation

$$X_c = \frac{A_{cr}}{A_{total}}$$

Equation 20: Crystallinity estimation

where A_{cr} is the area above the background and A_{total} is the total area (background + area above background). Figure 64 shows the XRD spectra and corresponding backgrounds for the solid regenerated cellulose nanostructures synthesized from all-at-once and drop-by-drop (0.5 mL/min) addition of nonsolvent.

Scanning electron microscopy (SEM) was performed using a LEO 1530 thermally-assisted field emission (TFE) microscope at 5 kV. The samples were lightly sputter coated with Au/Pd prior to observation.

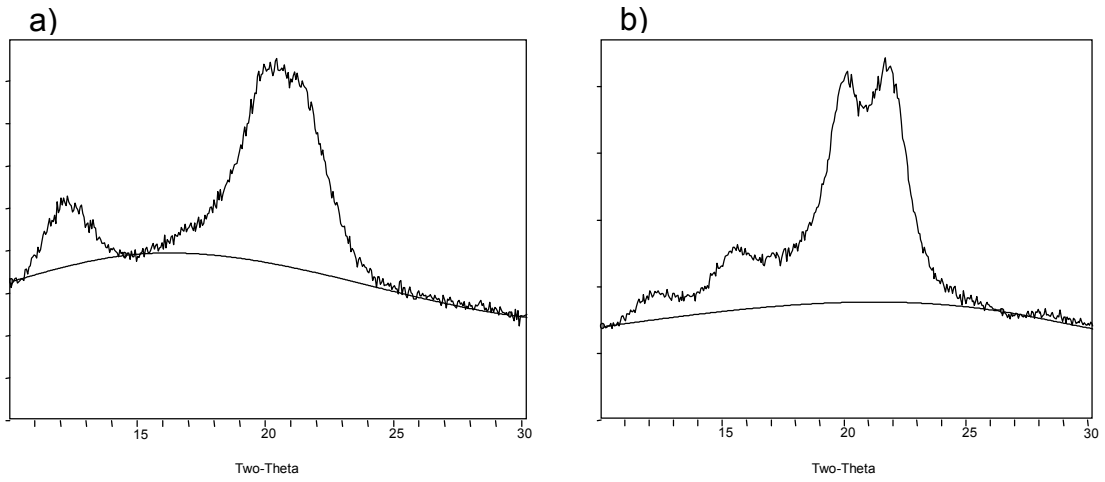

Figure 64: XRD spectra and corresponding background estimates for crystallinity determinations of solid regenerated cellulose nanostructures prepared with a) all-at-once and b) drop-by-drop (0.5 mL/min) addition of non-solvent.

7.3 Results and Discussion

As reported by previous researches (109, 111, 112, 158), cellulose forms nanosized aggregates when dissolved in NMMO. These cellulose aggregates can be precipitated from dilute NMMO solution by adding a non-solvent, such as water. Figure 65 shows that the particle size and morphology of such pure regenerated cellulose nanoparticles depend on the addition rate of water to the dissolved cellulose- NMMO monohydrate solution under agitation (stirring or sonication). For addition rates of 5 mL/min and 0.5 mL/min, the sphere diameters are approximately ~30 nm and ~100 nm, respectively. However, adding nonsolvent all-at-once to the solution yields precipitated microfibrillar ribbons or worm like structures with diameters of approximately 10 nm.

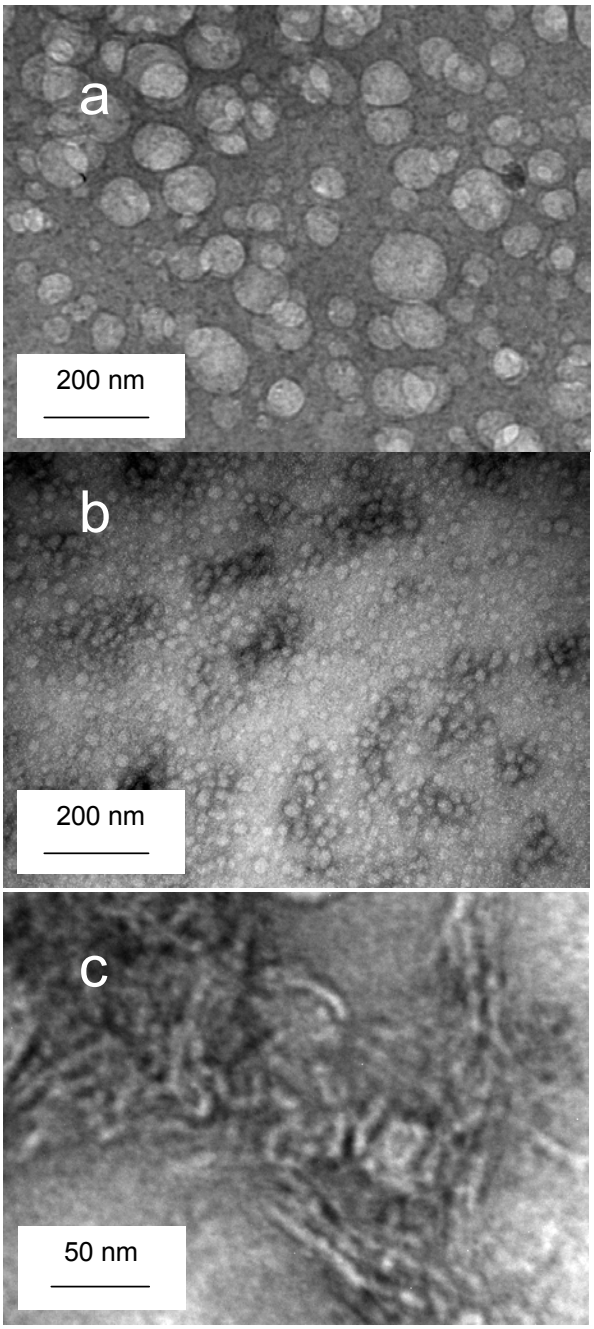

Figure 65: TEM images of solid regenerated cellulose nanostructures generated from (a) drop-by-drop at 5 mL/min (b) drop-by-drop at 0.5 mL/min, and (c) (a) all-at-once of nonsolvent addition rate.

Thus, adding nonsolvent at a slower rate gives nanospheres whose size increases as the rate of addition decreases. It appears that adding non-solvent in a drop-by-drop fashion allows the cellulose aggregates to collapse into spheres when confronted with the incompatible environment. As the rate of addition decreases, the polymers can further diminish their interaction with the non-solvent by incorporating more polymer aggregates into the collapsed sphere, forming larger diameter particles. In contrast, all-at-once addition does not allow time for chain orientation during the collapse, suggesting that a rapid desolvation process leads to the precipitation of the original shape of the cellulose aggregate in NMMO solution during the regeneration process. The worm like structures shown in Figure 65c are consistent with the simplest fringed micelle model originally suggested by Schulz for cellulose aggregates in solution rather than the more complex star-shaped structure with dangling chains suggested later (111, 158).

The lyophilized regenerated cellulose nanoparticles were also characterized by x-ray diffraction. Table 11 gives the crystallinity and crystal phase of the regenerated cellulose powders synthesized from all-at-once and drop-by-drop (0.5 mL/min) addition of non-solvent.

Table 11: Crystal structure of solid regenerated cellulose nanostructures synthesized from all-at-once and drop-by-drop (0.5 mL/min) addition of nonsolvent.

	All-at-once	Drop-by-drop (0.5 mL/min)
Crystallinity, %	24.2%	34.4%
Type of the crystal phase	Cellulose-I	Cellulose-I and Cellulose-II

Notably, the all-at-once addition of non-solvent gives only amorphous cellulose and cellulose-I crystal phase, while drop-by-drop addition gives amorphous, cellulose-I, and cellulose-II phases. It is well known that under typical manufacturing conditions of regenerated cellulose materials from NMMO solution in a precipitation bath, only amorphous cellulose and cellulose-II crystal phase are obtained (107). The lack of crystalline cellulose-II for the all-at-once regenerated cellulose particles suggests that the precipitation of dissolved cellulose molecules was too rapid to allow reorientation and crystallization of the cellulose molecules. In other words, the regenerated cellulose can only form an amorphous, not crystal, phase, if the non-solvent is quickly added to the solution, such as in an all-at-once addition manner. It can also be concluded that the 24.2% cellulose-I phase obtained from "all-at-once" precipitated method was from undissolved crystallites of the original cellulose powder. Drop-by-drop addition of non-solvent increases the crystallinity to 34.4% with both cellulose-I and cellulose-II present. Thus, collapse of the cellulose aggregates during slower addition of non-solvent allows molecular ordering of the chains to give cellulose-II in addition to the undissolved cellulose-I crystallites. The proposed precipitation mechanism is illustrated in Figure 66.

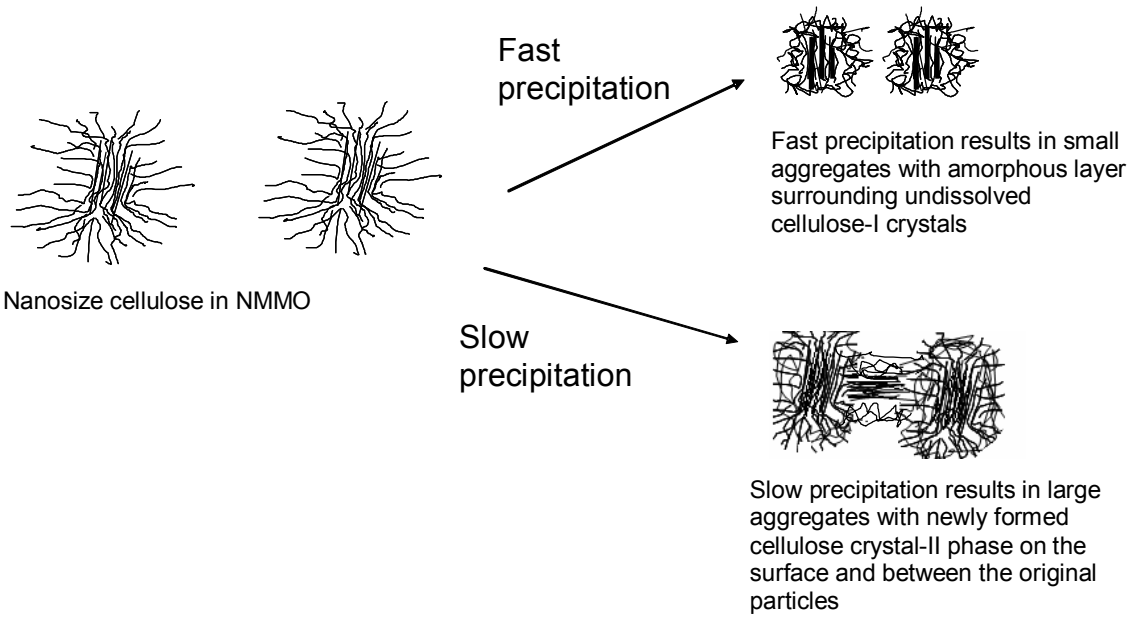

Figure 66: Proposed mechanism of cellulose nanoparticles precipitation from NMMO monohydrate by adding water at different water-addition rates.

In additional to pure cellulose nanoparticle precipitation, discrete inorganic-cellulose core-shell and hollow cellulose nanoparticles were prepared by self-encapsulation with regenerated cellulose as shown in Figure 67. The regenerated cellulose core-shell particles could be synthesized using a variety of colloidal templates including TiO_2 (Figure 67a), PCC (Figure 67b), and silica (Figure 67c), independent of template chemistry and shape. The SEM images clearly show that while the pristine templates have a smooth surface, the regenerated cellulose shell is composed of nanoparticles similar to the regenerated pure cellulose nanospheres discussed above.

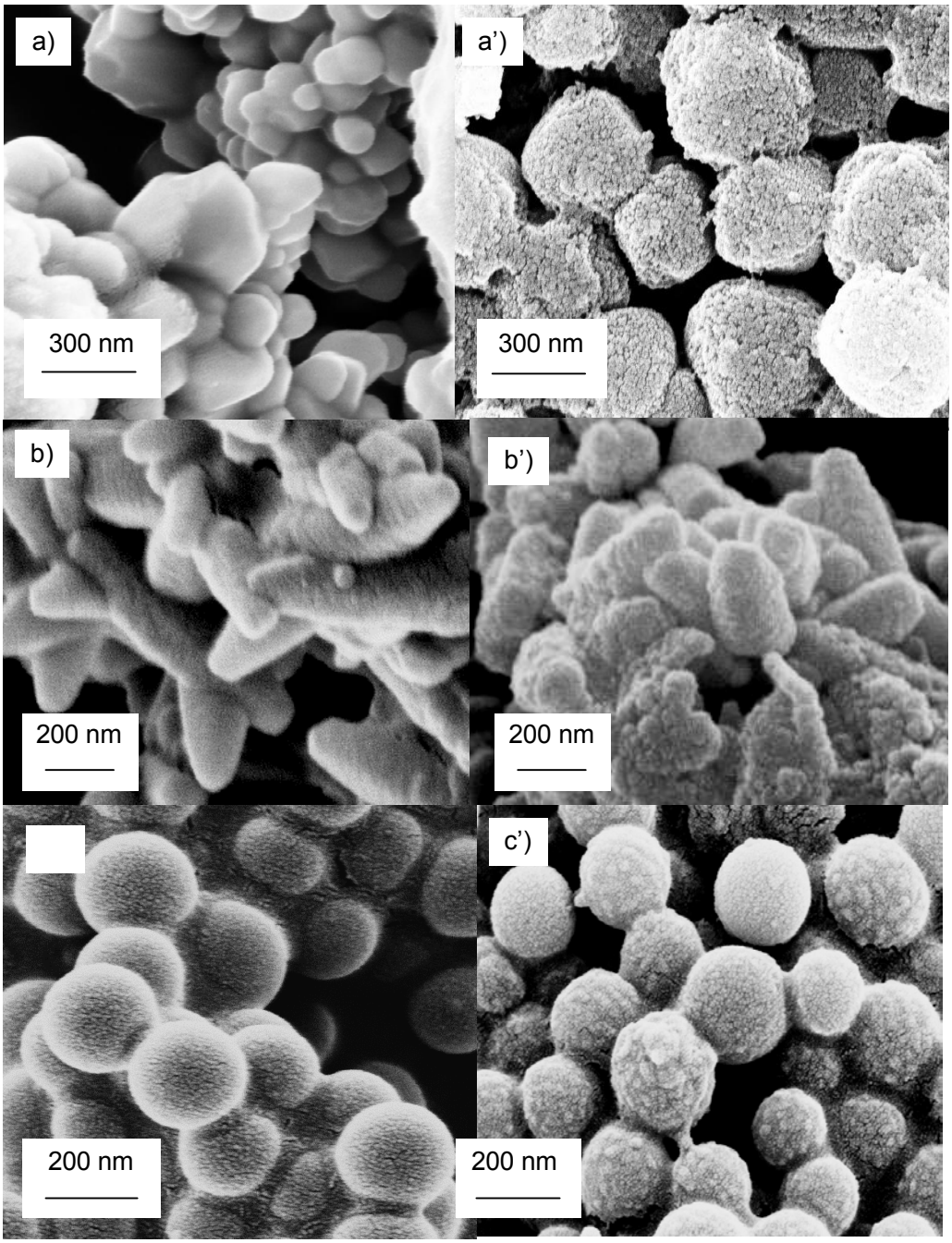

Figure 67: SEM images of the uncoated colloidal templates of (a) TiO_2, (b) PCC, (c) silica and the corresponding regenerated cellulose core-shell nanoparticles (a'-c').

Significantly, cellulose coated particles could only be obtained in the presence of PAA. Without addition of PAA to the water-cellulose-template-NMMO solution, no regenerated cellulose shell was observed on the template surface. The difference between the mechanisms of cellulose precipitation with and without PAA is explained by the illustration shown in Figure 68.

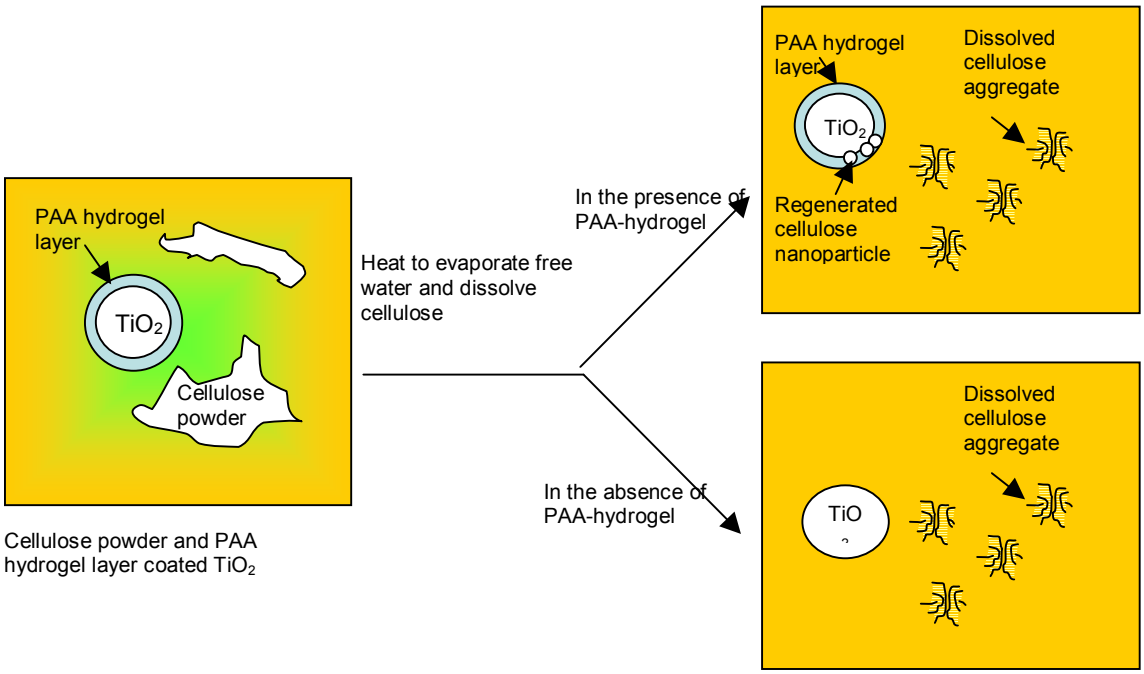

Figure 68: Proposed mechanism for the formation of cellulose core-shell nanoparticles during dissolution of cellulose in NMMO monohydrate.

During synthesis of the core-shell particles, a small amount of polyacrylic acid is first added to an aqueous dispersion of the inorganic colloidal template, where it adsorbs onto the template surface and stabilizes the inorganic suspension. When this suspension is blended with cellulose powder and NMMO solution and then heated under vacuum, bulk water evaporates and NMMO monohydrate solvent is formed with a water content of

13.3 wt.% and the cellulose powder is dissolved (106). At this condition, although the majority of free water in NMMO is removed, the water bound in the PAA hydrogel layer surrounding the template surface remains. The micelle-like cellulose aggregates in the NMMO bulk solution then immigrate to the inorganic particle surface, and are precipitated out by the water in the hydrogel layer. In contrast, there is no remarkable water layer on the inorganic surface in the absence of PAA. Again, the critical role of the PAA hydrogel on the encapsulation mechanism was confirmed by repeating the synthesis without PAA. In this case, no regenerated cellulose shell was observed on the template surface.

Figure 69 shows the hollow nanocapsules obtained upon removal of the PCC core in slightly acidic solution. Notably, the integrity of the hollow shell, which is about 30 nm thick, is maintained after drying.

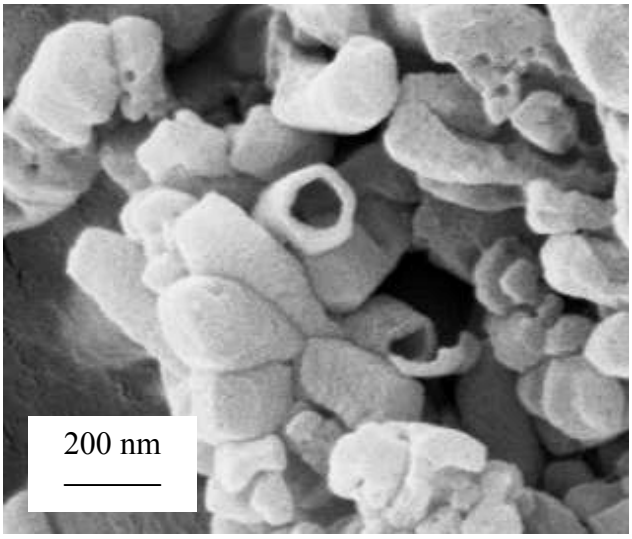

Figure 69: SEM image of hollow cellulose nanocapsules obtained after dissolving the sacrificial PCC core under slightly acidic conditions.

7.4 Conclusion

Regenerated cellulose nanoparticles were synthesized with varying morphology, crystalline phase, and crystallinity via simple precipitation of dissolved cellulose in NMMO monohydrate solution under agitation. Depending on the rate of addition of non-solvent, the regenerated cellulose formed either spherical nanoparticles with diameters from 20 to 150 nm or wormlike microfibrillar ribbons. Discrete, uniform cellulose shells were formed on the surface of inorganic colloidal templates in NMMO solution via precipitation of dissolved cellulose in the PAA hydrogel layer surrounding the templates. Hollow cellulose nanoparticles were also prepared by dissolving the inorganic cores.

CHAPTER 8

ENHANCED BONDABILITY BETWEEN INORGANIC PARTICLES AND POLYSACCHARIDE SUBSTRATE BY ENCAPSULATION WITH REGENERATED CELLULOSE

Abstract

Inorganic fillers are widely used in coatings, paints, printing inks, and papermaking. A general problem in such applications is the poor compatibility and weak bondability of the filler with polymeric substrates. Surface modification and encapsulation are common methods adapted to enhance interactions between the filler surface and the substrate. This paper presents the bondability improvement between inorganic particles and a polysaccharide substrate by the discrete encapsulation of the filler with a thin cellulose shell. The crystallinity of the coated carbohydrate layer is shown to significantly affect the bondability of the core-shell particles. The impact of the coating layer on light scattering efficiency was also studied using theoretical Mie scattering calculations.

8.1 Introduction

Chapter 7 presents the facile synthesis of nanostructured inorganic-regenerated cellulose core-shell particles. The process is based on a subtle modification of the Lyocell process that has been widely used in manufacturing regenerated cellulose fibers and films from 4-Methylmorpholine N-oxide (NMMO) monohydrate solvent system (152, 153). In principal, this method is general and can be used to prepare cellulose core-shell nano- or micro-scale particles from a wide range of core materials, such as inorganic fillers,

organic pigments, drugs, etc. Because cellulose is renewable, biodegradable, bioinert, and has strong hydrogen bondability and swellability, the encapsulation of colloidal templates with cellulose has wide applicability in drug delivery, food industry, polymer composite manufacturing, coatings, paints, and papermaking.

The enhanced bondability of the inorganic-cellulose core-shell particles with cellulose and other polysaccharide substrates is particularly advantageous for papermaking. Inorganic fillers such as TiO_2, clay, and $CaCO_3$ have traditionally been used to improve end-use properties of paper such as opacity, brightness, gloss, smoothness, porosity, and printability (4). The increased substitution of low cost inorganic fillers, such as clay and $CaCO_3$, for expensive wood fibers in the paper sheet should also lead to a significant reduction in the cost of papermaking. In fact, as the price of wood pulp continues to rise (a 75% price increase per ton between 2001 and 2006), there is mounting pressure to increase the filler loading across all paper grades. However, it is well known that increasing filler content decreases paper strength, as the non-bonding filler disrupts and reduces the fiber-fiber bonding within the sheet. To overcome this critical constraint, an active research area has developed to synthesize organic/inorganic composites capable of forming high strength bonds with wood fibers. The most promising composites to date combine traditional papermaking fillers and renewable carbohydrate materials, such as starch and wood fines, that can form strong hydrogen bonds with fibers (3, 4, 100, 104, 105). These composites give dramatic improvements in paper strength over comparable unmodified fillers at constant filler loading. However, the particle size, size distribution and shape of these composite filler particles cannot be well controlled, which hinders

fundamental understanding of core-shell functional fillers and their practical industrial applications.

Here we report the high bonding strength between wood fiber and the regenerated cellulose shell material of our inorganic core-shell particles and compare this strength with traditional paper strength enhancing additives. Using a well known computer code based on Mie theory (BHCOAT), we show that our well-defined, discrete cellulose coated inorganic fillers can scatter more light within a paper sheet than uncoated fillers under optimized conditions. Thus, the inorganic-cellulose core-shell particles can enhance the physical and optical properties of paper.

8.2 Experimental

8.2.1 Materials

Cotton pulp (Procter & Gamble Cellulose), potato starch (Experimental Industrial Starch X100, Grain Processing Corporation), mechanical pulp (Augusta Newsprint/ Abitibi Consolidated), and CPAM (cationic polyacrylamide retention aid, medium-charge density, high molecular weight, Ciba Specialty Chemicals Corp.) were used as received. Cellulose powder (medium fibers from cotton linters, Sigma), NMMO (50% w/w aqueous solution, Alfa Aesar), and sulfuric acid (96.5%, Em Science) were used without further purification. Water was obtained from a Nanopure ultrapure water system with a resistivity of about 18 MΩ cm.

8.2.2 Preparation

The bondability of the encapsulating shell with a wood fiber substrate was investigated for several polysaccharide shell materilas including cellulose nano-whiskers, wood fines, and starch by measuring the peal force between the compressed polysaccaride sheet and the substrate. Typically, for preparation of pure regenerated cellulose nanospheres, a dilute solution of cellulose dissolved in NMMO (1 wt. %) was first prepared by dispersing 0.5 g of cellulose powder with 95.5 g of aqueous NMMO (50 wt. %). This mixture was then heated in a rotary evaporator under vacuum at 60 °C for 20 minutes followed by 95 °C for 20 minutes. During heating, bulk water is removed from solution and the cellulose dissolves in NMMO. The solution was then transferred to an oil bath and maintained at 95 °C under mechanical stirring. The dissolved cellulose in NMMO was then precipitated by adding 50 mL of water drop-by-drop at a rate of 0.5 mL/min. The resulting solids were isolated by three centrifugation (25,900 RFC for 2.5 min) and water washing cycles and then lyophilized.

Cellulose nanowhiskers were prepared as outlined previously (159). Cotton fiber was hydrolyzed with 64 wt. % sulfuric acid at 45 °C for 45 minutes. Prior to hydrolysis, the dry cotton fiber sheets were torn into small pieces and fed through a Wiley mill (Arthur H. Thomas Co.) to pass through a 1 mm mesh. Typically, 40 g ground cotton was treated with 700 mL sulfuric acid solution. Immediately following hydrolysis, the unhydrolyzed cellulose whiskers was diluted 10-fold with water. The solids were allowed to settle overnight and then collected with minimal amounts of solution. Excess acid was removed by three washing and centrifugation (25,900 RCF for 30 min.) cycles followed by

dialysis (Spectra/Por membrane, MWCO 50K) against water for several days until the water achieved a neutral pH. The cellulose whisker suspension was then sonicated (Heat Systems-Ultrasonics W-385 probe sonicator) for 35 min while cooling in an ice bath. The resulting suspension was allowed to stand over a mixed bed resin (Sigma, TMD-8) for 48 h and then filtered through hardened ashless filter paper (Whatman, 541) and concentrated to 8.27% using a rotary evaporator under vacuum.

Wood fines were prepared by refining mechanical pulp for one hour at 25% consistency in a Valley beater. Fines were collected from the fiber suspension using a Britt Jar with a 200 mesh screen, yielding a stable suspension. In order to concentrate the suspension, CPAM (1ppm) was added to flocculate and settle the fines and a majority of the supernatant was removed.

The bonding strength between polysaccharide coating material and fiber was measured for laminates prepared following the method of Yoon and Deng as illustrated in Figure 70 (160).

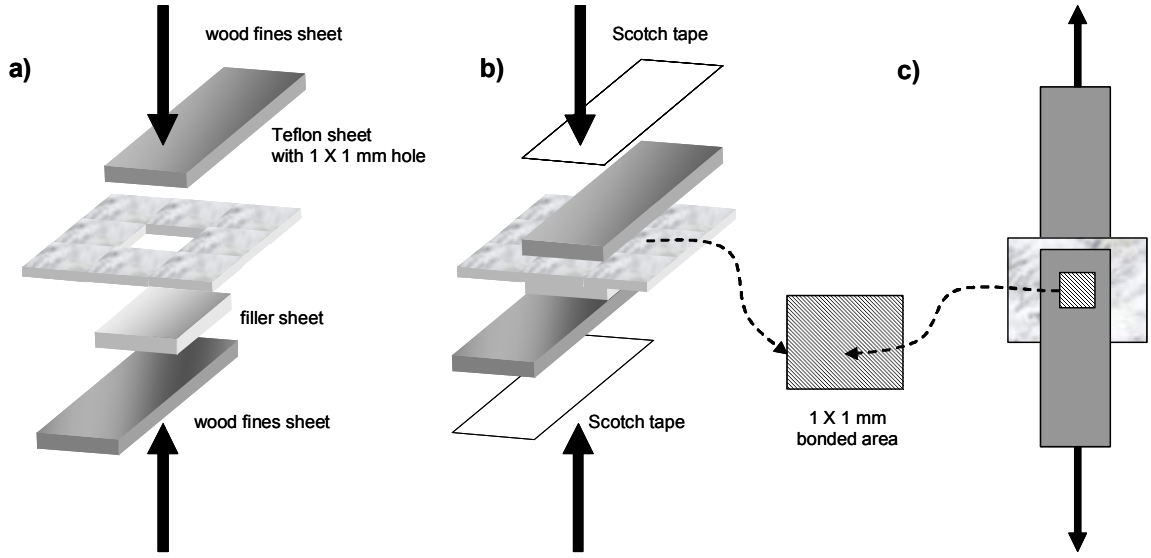

Figure 70: Illustration of the assembly of laminates for the measurement of fiber/polysaccharide material shear bond strength. The laminate is a) assembled and wet pressed at 20 psi and 105 °C for 5 minutes, b) reinforced with scotch tape and pressed for 1 minute at 20 psi and 105 °C, and c) delaminated under tensile stress.

Wood fines were used as the model fiber because their size and conformability allows them to be pressed into a strong, smooth sheet. These sheets were prepared by vacuum filtering the concentrated suspension of fines onto qualitative filter paper (Whatman). Using a razor blade, the damp pad was cut into individual strips, approximately 1 x 3.5 cm in size, and the filter paper backing removed. Several different methods were required to obtain a compressed, uniform 1 x 1 cm polysaccharide material sheet, depending on the type of material. The lyophilized cellulose nanospheres were dampened and pressed at 90 psi and 120 °C for 10 minutes using an automated pressing apparatus (P. Bonk &

Co.). Starch powder was dampened and pressed at 50 psi and 120 °C for 10 minutes. Cellulose nanowhiskers were cast as a film from concentrated solution and dried at room temperature. The fines filler sheet was prepared as above.

A laminate composite composed of fiber and polysaccharide material was made by placing the polysaccharide sheet on a wet wood fines sheet, followed by a thin Teflon film with a 2 x 2mm hole in the center, followed by another wet fines sheet. The bonding area between the filler and fiber was fixed by the hole in the Teflon film. This composite was then pressed at 20 psi and 105 °C for 5 minutes to form a laminate. To ensure the integrity of the fines sheets during tensile testing, both sheets were reinforced by applying Scotch tape to the back-side followed by pressing at 20 psi and 105 °C for 2 minutes. The laminated sheets were then conditioned at 20 °C and 60% relative humidity for at least three hours. The specific bonding shear strength of the laminates was then measured using an Instron tensile tester.

8.2.3 Characterization

X-ray diffraction (XRD) was carried out using an X'Pert Pro Alpha-1 diffractometer with an incident beam monochrometer allowing only the $K\alpha_1$ component of Cu radiation. XRD spectra were analyzed using JADE 7 software from Materials Data. Crystallinity was estimated using Equation 20.

Figure 71 shows the typical XRD spectra and corresponding backgrounds for the four polysaccharide materials studied.

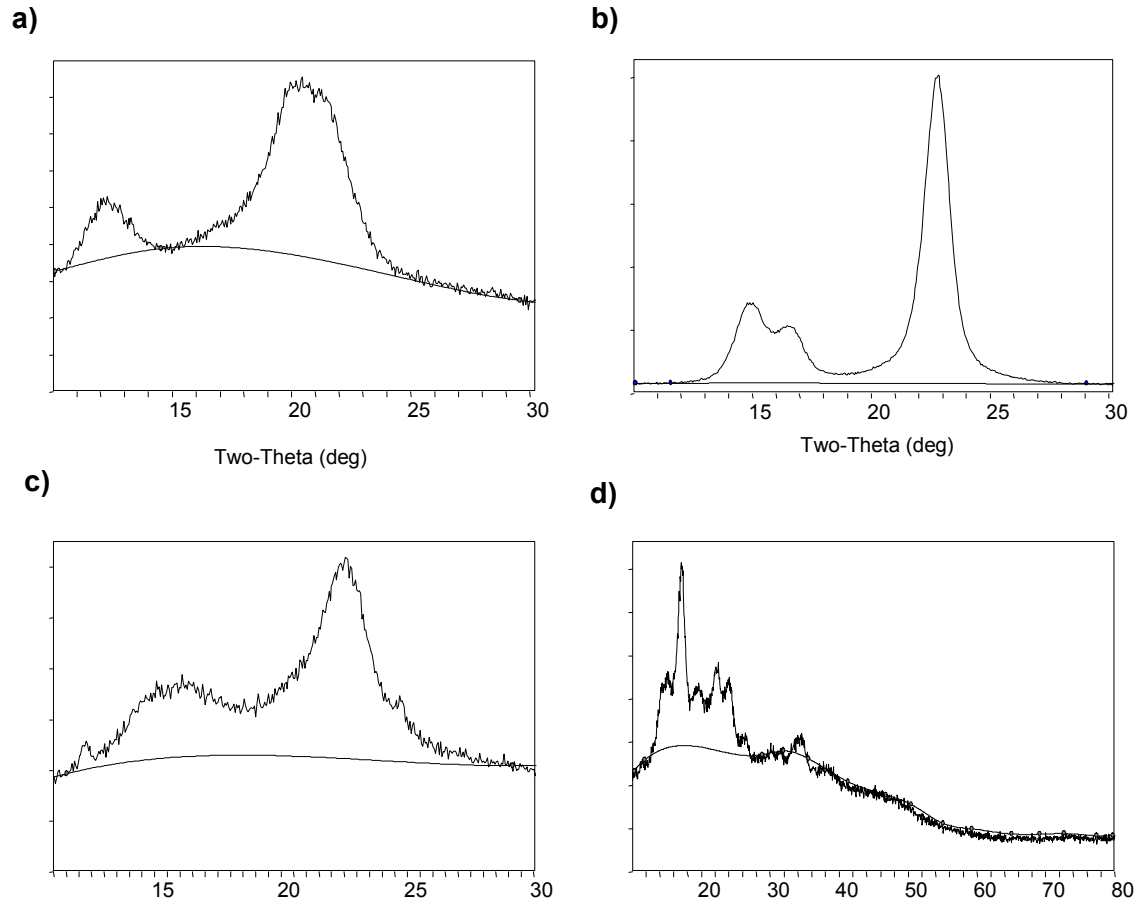

Figure 71: XRD spectrum and corresponding background estimate for the determination of crystallinity for (a) regenerated cellulose nanospheres, (b) cellulose whiskers, (c) wood fines, and (d) starch.

8.3 Results and Discussion

The previously synthesized inorganic-regenerated cellulose (RC) core-shell nanoparticles are shown in Figure 72 for TiO_2, $CaCO_3$, and silica cores. The detailed structure and formation mechanism of these particles were reported separately (161).

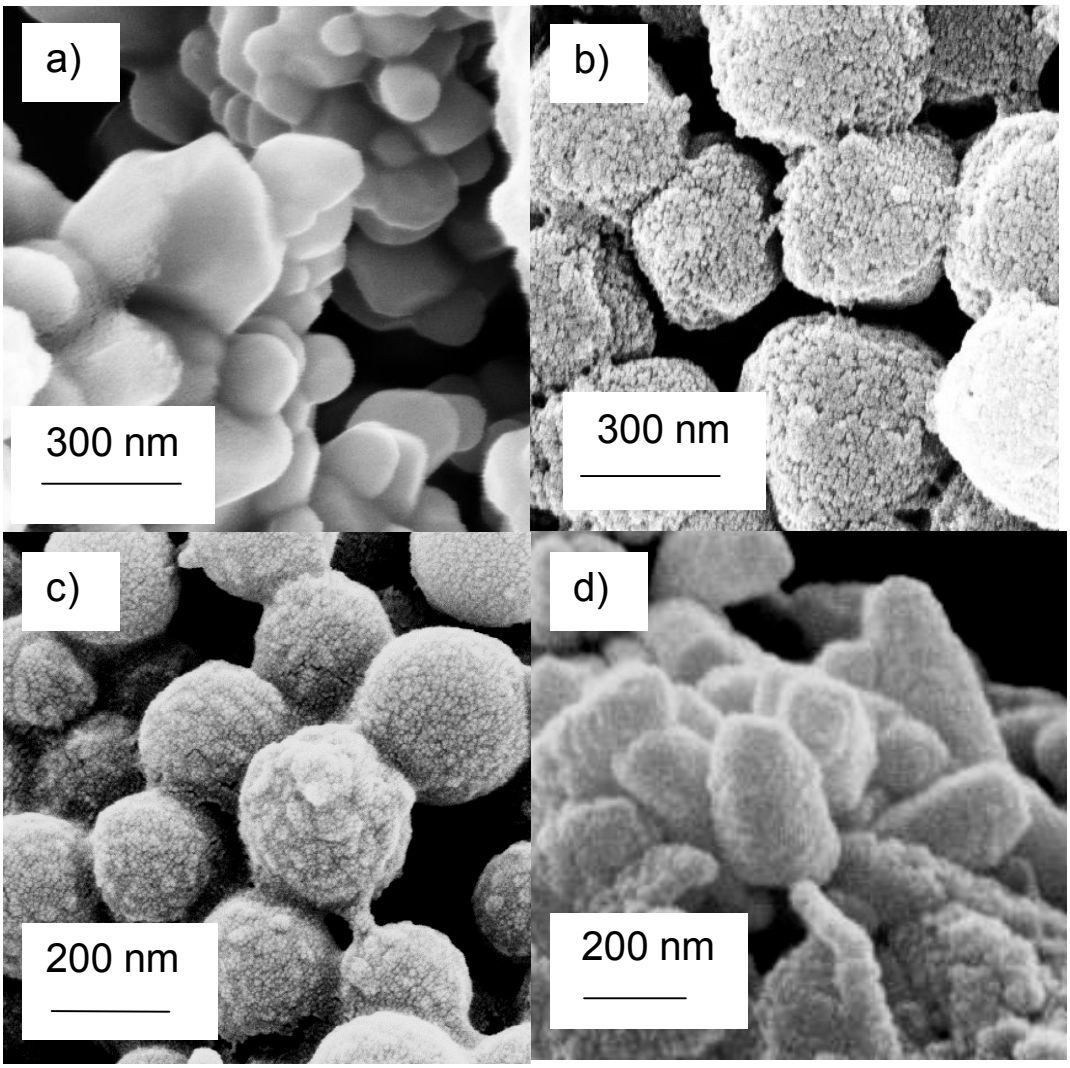

Figure 72: SEM images of (a) uncoated rutile particles, (b) Cellulose coated rutile, (c) Cellulose coated silica, and (d) Cellulose coated PCC.

The encapsulation mechanism was shown to be independent of inorganic core surface chemistry and shape. Generally speaking, when dissolved in NMMO solution containing

dispersed inorganic colloids, cellulose forms nano-sized aggregates in the hydrogel layer surrounding the inorganic particles. The dissolved aggregates form nano-sized, spherical precipitates upon contact with the hydrogel layer which completely encapsulate the inorganic particle surface. The thickness of the cellulose shell is approximately 30 nm. As shown in Figure 73, the spherical precipitates comprising the shell can be isolated as individual RC nanospheres. The detailed structure and formation mechanism of these particles were also reported previously (161).

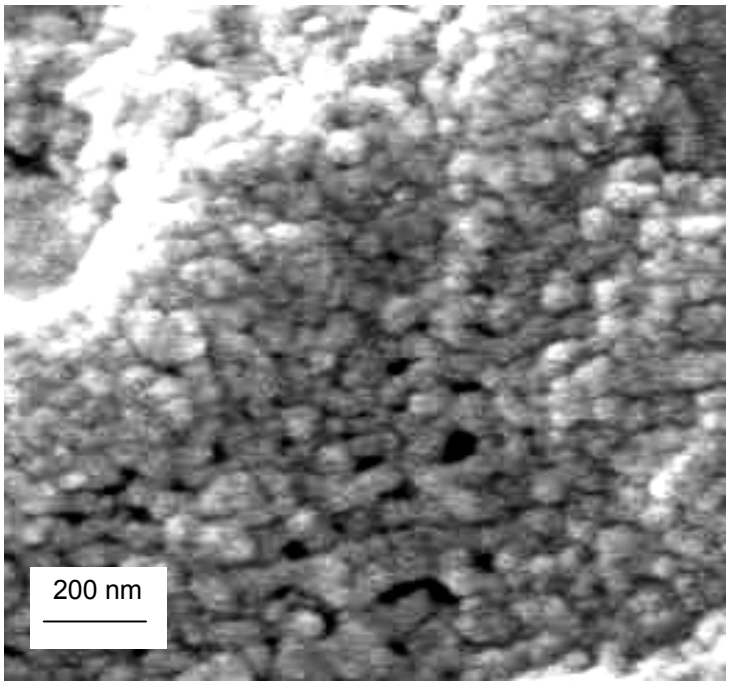

Figure 73: SEM image of individual regenerated cellulose nanospheres.

Generally, the particles are synthesized by adding water nonsolvent at a fixed rate to a dilute solution of cellulose dissolved in NMMO under stirring. The crystallinity, size, and shape of the solid RC nanospheres are influenced by the rate of addition of the nonsolvent during precipitation. The spherical particles shown in Figure 73 were

synthesized with a rate of 0.5 mL/min and have an average diameter of approximately 30 nm and a crystallinity of 25.0%.

The bondability of the inorganic-cellulose core-shell particles with wood fiber was studied by measuring the bonding strength between a wood fiber surface wet pressed against a surface composed of the individual RC spherical nanospheres shown in Figure 73. For comparison, the bonding strength between wood fiber and other polysaccharide materials including cellulose nanowhiskers, starch, and wood fiber itself were measured. These polysaccharides have either previously been utilized as the fiber-bonding component of inorganic composite fillers or could be used. Cellulose whiskers were chosen because of their intrigue and high performance in other types of nanocomposites (162, 163). Unlike unmodified inorganic fillers that do not form hydrogen bonds or other strong bonds with cellulose fiber, the free glucose hydroxyls of these polysaccharide materials can participate in hydrogen bonding with cellulose molecules on the fiber surface and supplement the number of hydrogen bonds that naturally occur in the bonded area between two fibers (9). While dissolved starch has traditionally been used in papermaking to increase paper strength, the starch molecules adsorb onto the surface of fillers in a nondeformable layer of molecular-level thickness. For the polysaccharide-inorganic composites reported previously, including our regenerated cellulose encapsulated particles, substantial amounts of swollen, deformable polysaccharide material is available for bonding, which leads to superior bondability. Zhao et al. found a nearly 20% increase in handsheet tensile strength for starch gel coated precipitated calcium carbonate filler over the conventional wet-end starch addition method (4). The

bond strength between wood fiber and the different polysaccharides materials as measured in this study are shown in Figure 74. The regenerated cellulose nanospheres form strong bonds with wood fibers, on the order of starch-fiber and fiber-fiber bonds, while cellulose whiskers have almost 5 times less bonding strength.

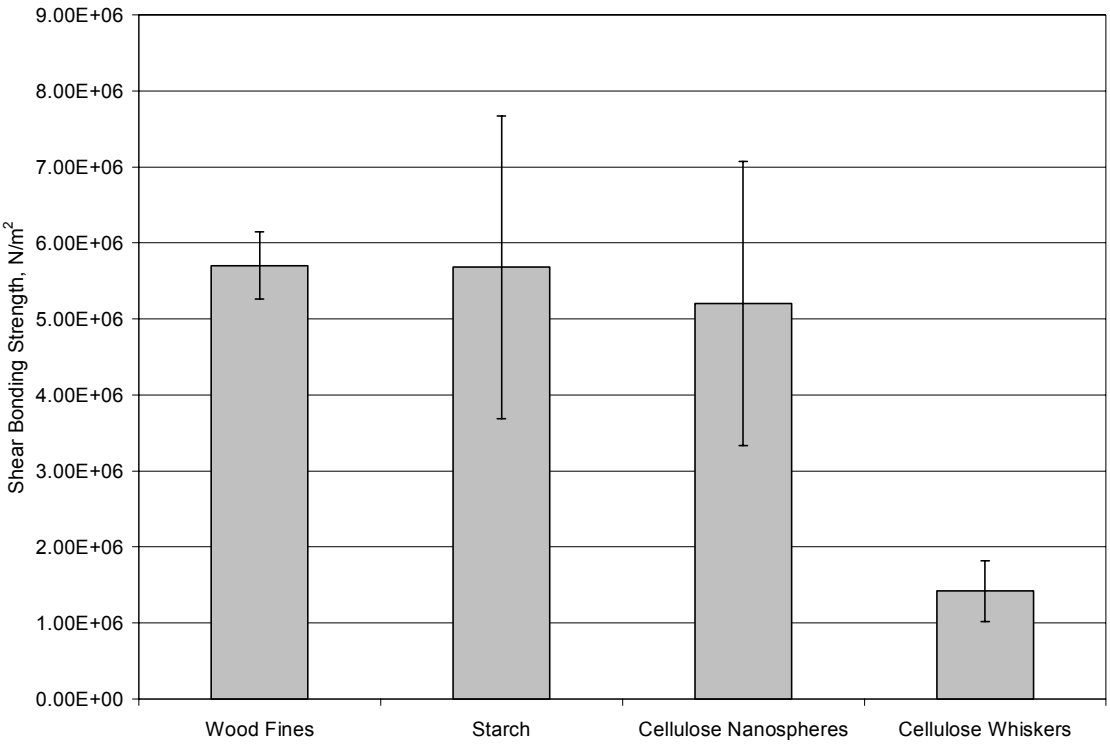

Figure 74: Shear bonding strength between wood fines and the polysaccharide materials under investigation.

Since all of the polysaccharide materials studied have similar functional groups, the hydrogen bonding ability is obviously impacted by another factor. It is expected that highly crystallized polysaccharides have less bonding ability with wood fibers in the paper sheet than amorphous polysaccharides because of a decrease in deformability. Only the amorphous regions of carbohydrate materials can swell in the presence of water. This swelling makes the materials more pliable to conform around fibers, which increases

bonding surface area and therefore bond strength. Table 12 shows that the cellulose whiskers have crystallinity five times higher than starch, the least crystalline and highest bonding material.

Table 12. Crystallinity of polysaccharide materials under investigation.

	Crystallinity, %
Potato starch	15
Cellulose nanospheres	25.0
Wood fines	31.5
Cellulose whiskers	77.6

Thus, the highly amorphous RC nanospheres, wood fines, and starch (with crystallinities of 25.0%, 31.5% and 15% respectively) should have much higher swellability than cellulosic nanowhiskers (with a crystallinity of 77.6%), and therefore bondability. Figure 75 shows that there is a direct relationship between polysaccharide crystallinity and bonding strength with fibers. As crystallinity increases, bonding strength decreases.

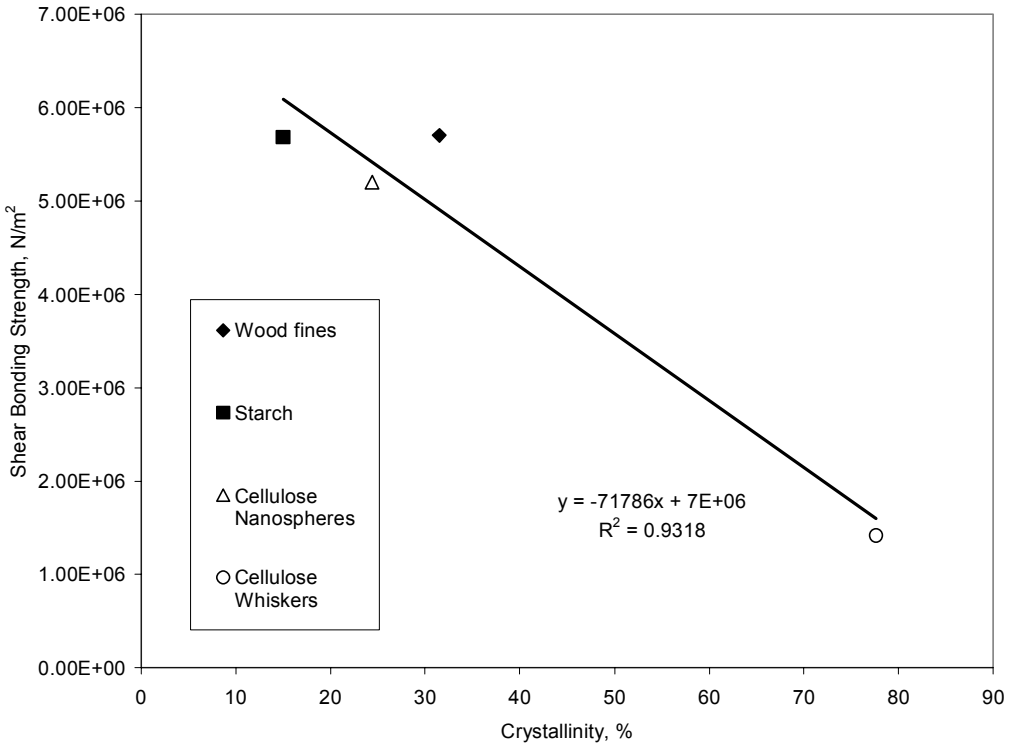

Figure 75: Dependence of fiber/polysaccharide bonding strength on the cystallinity of the polysaccharide material.

Notably, the wood fines have a higher bonding strength than anticipated by the trend line. This may be due to the presence of CPAM in the wood fines (CPAM was used to concentrate fines in the fines collection process). Studies have shown that treatment of both fiber plys with dry strength agent gives delamination strength improvement over single ply treatment (164). This work suggests that the most affective polysaccharide for paper strength enhancing inorganic composites is one with the least degree of crystallinity.

A principle reason for adding inorganic fillers to paper is to improve its optical properties such as opacity and brightness. The effect of the core-shell filler prepared in this study on the light scattering was also investigated. From established theory on light scattering by small particles, we know that our spherical, optimally sized (< 300 nm), individually encapsulated inorganic particles will scatter more light than other previously reported high-bonding inorganic-polysaccharide composites, which are all large (>> 1 μm) and anomaly shaped. Enhanced light scattering gives more opacity. Light scattering efficiencies, Q_{SCA}, for the regenerated cellulose coated and uncoated rutile and silica particles irradiated by light at 572 nm were determined using the well-known computer code BHCOAT developed by Huffman and Bohren (10). This code is based on Mie theory and provides solutions for the light scattering of a single isotropic, concentric sphere embedded in a homogeneous medium. Light scattering efficiency was determined for the above particles in air and in a pure cellulose matrix, as illustrated in Figure 76.

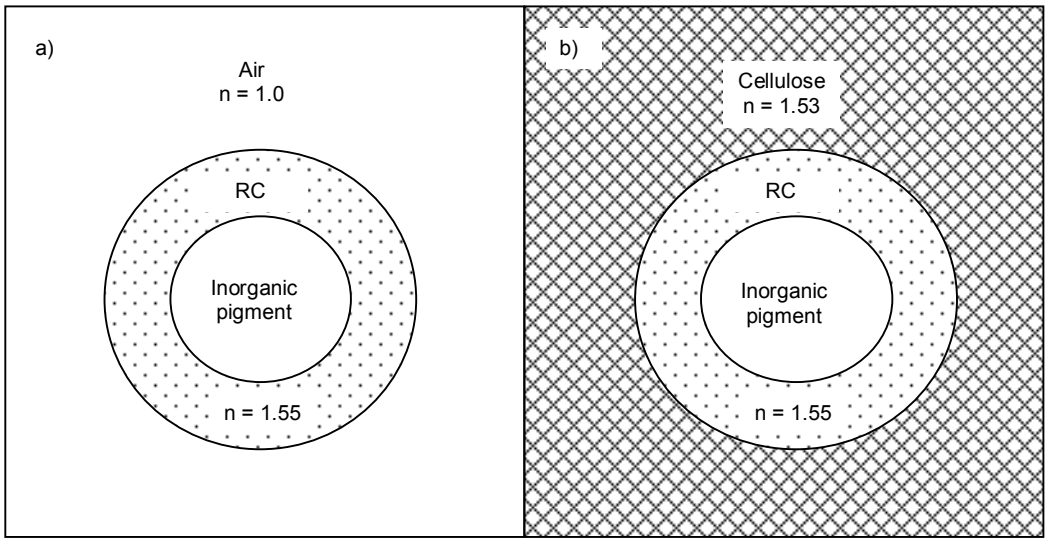

Figure 76: Illustration of the regenerated cellulose (RC) encapsulated inorganic pigments embedded in a) pure air and b) pure cellulose.

The particle size and refractive index data required as input to the program are listed in Table 13.

Table 13: Required input data for light scattering program, BHCOAT.

	Refractive index at 572 nm
Rutile	2.73
Precipitated Silica	1.45
Cellulose (fiber, Cellulose I phase)	1.53
Regenerated cellulose (Cellulose II phase)	1.55
	Core radius, nm
Rutile	128
Silica	136

The refractive index of rutile, n = 2.73, was determined using the average index approximation, which accounts for the difference in refractive index depending on the polarization state of the incident light (72, 73). All other refractive indices were obtained from literature and the particle sizes were obtained experimentally (165). As shown in Table 14, for pigments with low refractive index like silica, the RC coated pigments have higher scattering efficiency than the corresponding uncoated pigments, except when surrounded entirely by cellulose where the scattering efficiencies are the same. Therefore, these coated pigments can impart more opacity than corresponding uncoated particles when surrounded by air, a likely occurrence for porous, bulky sheets.

Table 14: Light Scattering Efficiency, Q_{SCA}, of uncoated and RC coated silica nanoparticles at λ=572 nm. Where $\Delta Q_{SCA} = Q_{SCA}^{coated} - Q_{SCA}^{uncoated}$

Surrounding Medium	**Silica Pigment**			**Rutile Pigment**		
	Uncoated	Coated	ΔQ_{SCA}	Uncoated	Coated	ΔQ_{SCA}
Air	0.60	1.33	+0.73	4.32	3.29	-1.03
Cellulose	0.0065	0.0035	-0.003	1.66	1.12	-0.54

Although the RC coated pigments (such as silica) have higher scattering efficiency than the corresponding uncoated pigments, also as shown in Table 14, the RC coated pigments have lower scattering efficiency than the corresponding uncoated pigments with a high refractive index like rutile.

8.4 Conclusion

The bondability with cellulosic substrates of discrete, uniformly coated inorganic-regenerated cellulose nanoparticles was investigated. The regenerated cellulose nanospheres comprising the composite's shell form bonds with wood fibers on the order of starch-fiber and fiber-fiber bonds. Bonding strength was shown to depend on the crystallinity, and therefore swellability and conformability, of the polysaccharide material, with starch (crystallinity = 15%) giving about five times greater bonding strength than cellulose whiskers (crystallinity = 77.6%). Finally, calculations of light scattering based on Mie theory indicate that the light scattering of cellulose encapsulated pigments of low index of refraction, like silica, will be equal to or greater than the scattering of the uncoated pigments, depending on the porous structure of the paper sheet.

CHAPTER 9

OVERALL CONCLUSIONS

This thesis showed that synthesis of novel, tailored titanium dioxide pigments with controllable nanoscale morphological features can significantly enhance the optical and strength properties of paper.

The light scattering efficiency of polycrystalline TiO_2 nanoparticles with varying crystal structure were evaluated by measuring the opacity of optically uniform cellulose nanowhisker films loaded with 1 vol.% pigment. Polycrystalline anatase pigments with crystal sizes of 17 nm provided 13% less opacity than the commercial rutile pigment, while polycrystalline pigments containing a one-to-one mixture of anatase and rutile crystals provided similar opacity as commercial rutile. Polycrystalline rutile pigments composed of *on average* two rutile crystals per particle in a linear arrangement with crystal sizes of 291 nm gave 6% more opacity than the commercial rutile pigment composed of *on average* 1.3 rutile crystals per particle with crystal sizes of 210 nm. Theoretical light scattering calculations using the T-Matrix Method confirm the higher efficiency of the synthesized polycrystalline rutile pigments over commercial rutile. It is believed that the greater than expected light scattering efficiency of the biphasic pigment results from reflection and refraction of light at the grain boundaries between crystals of different phase, which have different refractive indices.

The light scattering efficiency of core-shell and hollow polycrystalline TiO_2 nanoparticles with varying crystal structure were evaluated by measuring the opacity of optically uniform cellulose nanowhisker and bleached fiber films loaded with 3 wt.% pigment. The opacifying power of the rutile titania core-shell particles was found to be superior to the PEG filled hollow particles at equal *titania* loadings in the film. The light scattering efficiency of the polycrystalline silica cores was found to depend on calcination temperature and crystal structure. It is suggested that the increased opacifying power of the silica-titania core-shell particles over the same PEG filled titania shells results from light scattering taking place within the polycrystalline silica cores. Hollow rutile titania particles with a 1186 nm cavity size provide about 6% more opacity then commercial rutile, while hollow particles with 272 nm cavity provide about 3% less in a highly pressed bleached fiber matrix.

Titania core-shell and hollow nanoparticles with tunable shape were synthesized via layer-by-layer assembly and sol-gel nanocoating techniques using high aspect ratio cellulose whisker templates. It was found that the shape of the cellulose whisker template was not maintained during growth of the coating layer and that the aspect ratio of the synthesized titania particles can be tuned by varying the coating thickness and/or the aspect ratio of the template. The overall particle shape and cavity shape can be simultaneously tuned by choosing an appropriate template and coating thickness. Thus, synthesis of uniquely shaped titania nanoparticles through templating methods is not limited by the elementary geometries of currently available colloidal templates.

Regenerated cellulose nanoparticles were synthesized with varying morphology, crystalline phase, and crystallinity via a simple precipitation method from NMMO monohydrate solution under agitation. Depending on the rate of addition of non-solvent, the regenerated cellulose formed either spherical nanoparticles with diameters from 20 to 150 nm or wormlike microfibrillar ribbons. These nanosized cellulose aggregates formed a uniform cellulose shell on the surface of inorganic pigments via precipitation of dissolved cellulose from NMMO monohydrate solution in the PAA hydrogel layer surrounding the particles. Hollow cellulose nanoparticles were also prepared by dissolving the inorganic cores.

The bondability of the regenerated cellulose shell of the encapsulated inorganic pigments with a wood fiber substrate was investigated. The regenerated cellulose nanospheres comprising the composite's shell formed bonds with wood fibers whose strength was on the order of starch-fiber and fiber-fiber bonds. Bonding strength was shown to depend on the crystallinity of natural polymers, and therefore swellability and conformability, of the polysaccharide shell material, with starch (crystallinity = 15%) giving about five times greater bonding strength than cellulose whiskers (crystallinity = 77.6%). Calculations of light scattering based on Mie theory indicate that the light scattering of cellulose encapsulated pigments of low index of refraction, like silica, will be equal to or greater than the scattering of the uncoated pigments, depending on the porous structure of the paper sheet.

CHAPTER 10

FUTURE WORK

This dissertation spanned several different research areas including nanoparticle synthesis, fundamental light scattering theory, and carbohydrate chemistry. Therefore this work provides many opportunities for work from a scientific or practical applications perspective such as:

- Experimentally or theoretically determine the effect of the following variables on the light scattering efficiency of polycrystalline TiO_2 particles
  - Crystallite grain boundary surface area
  - Ratio of different phases
  - Crystallite geometry beyond linear arrangement
  - Hollow cavity size and shape
- Determine the light scattering efficiency of multi-phase, polycrystalline calcium carbonate particles whose crystals are also highly birefringent.
- Encapsulate inorganic pigments with amorphous hemicelluloses via precipitation from NMMO solution onto a PAA hydrogel layer surrounding the particles and study the bondabilty of the regenerated material with a cellulose substrate

REFERENCES

1. Koepenick, M., *Paper innovation ramps up with nano-chemistry*. Pulp & Paper Canada 102, (1), 17-21(2001).

2. Atalla, R.; Beecher, J.; Caron, R.; Catchmark, J.; Deng, Y.; Glasser, W.; Gray, D.; Haigler, C.; Jones, P.; Joyce, M.; Kohlman, J.; Koukoulas, A.; Lancaster, P.; Perine, L.; Rodriguez, A.; Ragauskas, A.; Wegner, T.; Zhu, J., *Nanotechnology for the Forest Products Industry Vision and Technology Roadmap*. TAPPI Press: Atlanta, GA, 2005.

3. Yan, Z.; Liu, Q.; Deng, Y.; Ragauskas, A., *Improvement of paper strength with starch modified clay*. Journal of Applied Polymer Science 97, 44-50(2005).

4. Zhao, Y.; Hu, Z.; Ragauskas, A.; Deng, Y., *Improvement of paper properties using starch-modified precipitated calcium carbonate filler*. TAPPI JOURNAL 4, (2), 3-7(2005).

5. Koppelman, M. H., Paper Filling. In *Pigmetns for Paper*, Hagemeyer, R. W., Ed. TAPPI Press: Atlanta, 1997.

6. Hagemeyer, R. W., Pigment-Coated Paper. In *Pigments for Paper*, Hagemeyer, R. W., Ed. TAPPI Press: Atlanta, 1997.

7. Bakshi, D.; Walrond, W. In *Paper and Pigment Trends*, The Pigment Course, Sandersville, GA, October 24-26, 2006; Imerys: Sandersville, GA, 2006.

8. Sennett, P., Kaolin Clays. In *Pigments for Paper*, Hagemeyer, R. W., Ed. TAPPI Press: Atlanta, 1997.

9. Scott, W. E., *Principles of Wet End Chemistry*. TAPPI Press: Atlanta, 1996.

10. Mathur, V. K. Multi-phase calcium silicate hydrates, methods for their preparation, and improved paper and pigment products produced therewith. International Patent Number WO 01/14274 A1, 2001.

11. Dupuis, D.; LaBarre, D.; Mur, G. Polymer/CaCO3 composite core/sheath particulates and hollow CaCO3. U.S. Patent No. 5,756,210, 1998.

12. Nakajima, T. Expanded hollow micro sphere composite beads and method for their production. U.S. Patent No. 6,225,361, 2001.

13. Hirai, T.; Hariguchi, S.; Komasawa, I.; Davey, R. J., *Biomimetic synthesis of calcium carbonate particles in pseudovesicular double emulsion*. Langmuir 13, (25), 6650-6653(1997).

14. Enomae, T.; Tsujino, K., *Application of spherical hollow calcium carbonate particles as filler and coating pigment*. Tappi Journal 3, (6), 31(2004).

15. Walsh, D.; Mann, S., *Fabrication of hollow-porous shells of calcium carbonate from self-organizing media*. Nature 377, (6547), 320-323(1995).

16. Qi, L. M.; Li, J.; Ma, J. M., *Biomimetic morphogenesis of calcium carbonate in mixed solutions of surfactants and double-hydrophilic block copolymers.* Advanced Materials 14, (4), 300(2002).

17. Colfen, H.; Antonietti, M., *Crystal design of calcium carbonate microparticles using double-hydrophilic block copolymers*. Langmuir 14, (3), 582-589(1998).

18. Patel, V. M.; Sheth, P.; Kurz, A.; Ossenbeck, M.; Shah, D. O.; Gower, L. B., *Synthesis of calcium carbonate coated emulsion droplets for drug detoxification*. ACS Symposium Series 878 (Concentrated Dispersions), 15-25(2004).

19. Hadiko, G.; Han, Y. S.; Fuji, M.; Takahashi, M., *Synthesis of hollow calcium carbonate particles by the bubble templating method*. Materials Letters 59, 2519-2522(2005).

20. Lin, H.; Cheng, Y.; Mou, C., *Hierarchial Order in Hollow Spheres of Mesoporous Silicates*. Chemistry of Materials 9, 3772(1998).

21. Caruso, R. A.; Susha, A.; Caruso, F., *Multilayered Titania, Silica, and Laponite Nanoparticle Coatings on Polystyrene Colloidal Templates and Resulting Inorganic Hollow Spheres*. Chemistry of Materials 13, 400(2001).

22. Bourlinos, A. B.; Karakassides, M. A.; Petridis, D., *Synthesis and characterization of hollow clay microspheres through a resin template approach*. Chem. Commun., 1518-1519(2001).

23. Hsu, W. P.; Yu, R.; Matijevic, E., *Paper Whiteners I. Titania Coated Silica*. Journal of Colloid and Interface Science 156, 56-65(1993).

24. Ninness, B. J.; Bousfield, D. W.; Tripp, C. P., *Formation of a thin TiO2 layer on the surfaces of silica and kaolin pigments through atomic layer deposition*. Colliods and Surfaces A: Physicochem. Eng. Aspects 214, 195-204(2003).

25. Caruso, F.; Shi, X.; Caruso, R. A.; Susha, A., *Hollow titania spheres from layered precursor deposition on sacrificial colloidal core particles*. Adv. Mater. 13, (10), 740-744(2001).

26. Caruso, R. A.; Antonietti, M., *Sol-gel nanocoating: an approach to the preparation of structured materials*. CHem. Mater. 13, 3272-3282(2001).

27. Collins, A. M.; Spickermann, C.; Mann, S., *Synthesis of titania hollow microspheres using non-aqueous emulsions*. J. Mater. Chem. 13, 1112-1114(2003).

28. Eiden, S.; Maret, G., *Preparation and Characterization of Hollow Spheres of Rutile*. Journal of Colloid and Interface Science 250, 281-284(2002).

29. Gu, S.; Kondo, T.; Mine, E.; Nagao, D.; Kobayashi, Y.; Konno, M., *Fabrication of sub-micrometer-sized jingle bell-shaped hollow spheres from multilayered core-shell particles*. Journal of Colloid and Interface Science 279, 281-283(2004).

30. Guo, C.-W.; Cao, Y.; Xie, S.-H.; Dai, W.-L.; Fan, K.-N., *Fabrication of mesoporous core-shell structured titania microspheres with hollow interiors*. Chemical Communications, 700-701(2003).

31. Hu, J.; Guo, Y.; Liang, H.; Wan, L.; Bai, C.; Wang, Y., J. Phys. Chem. B 108, 9734-9738(2004).

32. Imhof, A., *Preparation and characterization of titania-coated polstyrene spheres and hollow titania shells*. Langmuir 17, 3579-3585(2001).

33. Jokanovic, V.; Jokanovic, B.; Nedeljkovic, J.; Milosevic, O., *Modeling of nanostructured TiO2 spheres obtained by ultrasonic spray pyrolysis*
Colliods and Surfaces A: Physicochem. Eng. Aspects 249, 111-113(2004).

34. Nakashima, T.; Kimizuka, N., *Interfacial synthesis of hollow TiO2 microspheres in ionic liquids*. J. Am. Chem. Soc. 125, 6386-6387(2003).

35. Ren, T.-Z.; Yuan, Z.-Y.; Su, B.-L., *Surfactant-assisted preparation of hollow microspheres of mesoporous TiO2*. Chem. Phy. Letters 374, 170-175(2003).

36. Shiho, H.; Kawahashi, N., *Titanium compounds as coatings on polystyrene latices and as hollow spheres*. Colloid Polym Sci
278, 270-274(2000).

37. Strohm, H.; Lobmann, P., *Porous TiO2 hollow spheres by liquid phase deposition on polystyrene latex-stabilised Pickering emulsions*. Journal of Materials Chemistry 14, 2667-2673(2004).

38. Wang, D.; Song, C.; Lin, Y.; Hu, Z., *Preparation and characterization of TiO2 hollow spheres*. Materials Letters 60, 77-80(2006).

39. Xia, Y.; Mokaya, R., *Hollow spheres of crystalline porous metal oxides: A generalized synthesis route via nanocasting with mesoporous carbon hollow shells*. Journal of Materials Chemistry 15, 3126-3131(2005).

40. Yang, H. G.; Zeng, H. C., *Preparation of Hollow Anatase TiO2 Nanospheres via Ostwald Ripening*. journal of physical chemistry B 108, 3492-3495(2004).

41. Yang, Z.; Niu, Z.; Lu, Y.; Hu, Z.; Han, C. C., *Templated synthesis of inorganic hollow spheres with a tunable cavity size onto core-shell gel particles*. Angew. Chem. Int. Ed. 42, 1943-1945(2003).

42. Yin, J.; Chen, H.; Li, Z.; Qian, X.; Yin, J., *Preparation of PS/TiO2 core-shell microspheres and TiO2 hollow shells*. J. Mater. Sci. 38, 4911-4916(2003).

43. Zhang, Y. X.; Li, G. H.; Wu, Y. C.; Xie, T., *Sol-gel synthesis of titania hollow spheres*. Mat. Res. Bulletin 40, 1993-1999(2005).

44. Zhang, Y.; Li, G.; Wu, Y.; Luo, Y.; Zhang, L., *The formation of mesoporous TiO2 spheres via a facile chemical method*. J. Phys. Chem. B 109, 5478-5481(2005).

45. Ma, D.; Schadler, L. S.; Siegel, R. W.; Hong, J.-I., *Preparation and structure investigation of nanoparticle-assembled titanium dioxide microtubes*. Appl. Phys. Lett. 83, (9), 1839-1841(2003).

46. Kobayashi, S.; Hanabusa, K.; Hamasaki, N.; Kimura, M.; Shirai, H., *Preparation of TiO2 hollow-fibers using supramolecular assemblies*. CHem. Mater. 12, 1523-1525(2000).

47. Lu, H.; Zhang, L.; Xing, W.; Wang, H.; Xu, N., *Preparation of TiO2 hollow fibers using poly(vinylidene fluoride) hollow fiber microfiltration membrane as template*. Mat. Chem. Phys. 94, 322-327(2005).

48. Peng, T.; Hasegawa, A.; Qiu, J.; Hirao, K., *Fabrication of titania tubules with high surface area and well-developed mesostructural walls by surfactant-mediated templating method*. CHem. Mater. 15, 2011-2016(2003).

49. Zhu, H. Y.; Lan, Y.; Gao, X. P.; Ringer, S. P.; Zheng, Z. F.; Song, D. Y.; Zhao, J. C., *Phase transition between nanostructures of titanate and titanium dioxides via simple wet-chemical reactions*. J. Am. Chem. Soc. 127, 6730-6736(2005).

50. Tian, Z. R.; Voigt, J. A.; Liu, J.; McKenzie, B.; Xu, H., *Large oriented arrays and continuous films of TiO2-based nanotubes*. J. Am. Chem. Soc. 125, 12384-12385(2003).

51. Zhang, M.; Bando, Y.; Wada, K., *Sol-gel template preparation of TiO2 nanotubes and nanorods*. J. Mater. Sci. Lett. 20, 167-170(2001).

52. Imai, H.; Takei, Y.; Shimizu, K.; Matsuda, M.; Hirashima, H., *Direct preparation of anatase TiO2 nanotubes in porous alumina membranes*. J. Mater. Chem. 9, 2971-2972(1999).

53. Kasuga, T.; Hiramatsu, M.; Hoson, A.; Sekino, T.; Niihara, K., *Formation of titanium oxide nanotubes*. Langmuir 14, 3160-3163(1998).

54. Liu, S. M.; Gan, L. M.; Liu, L. H.; Zhang, W. D.; Zeng, H. C., *Synthesis of single-crystalline TiO2 Nanotubes*. CHem. Mater. 14, 1391-1397(2002).

55. Lee, S.-w.; Sigmund, W. M., *Formation of anatase TiO2 nanoparticles on carbon nanotubes*. Chemical Communications, 780-781(2003).

56. Mayya, K. S.; Gittins, D. I.; Dibaj, A. M.; Caruso, F., *Nanotubes prepared by templating sacrificial nickel nanorods*. Nano Letters 1, (12), 727-730(2001).

57. Fujikawa, S.; Kunitake, T., *Surface fabrication of hollow nanoarchitectures of ultrathin titania layers from assembled latex particles and tobacco mosaic viruses as templates*. Langmuir 19, 6545-6552(2003).

58. Caruso, R. A.; Susha, A.; Caruso, F., *Multilayered titania, silica, and laponite nanoparticle coatings on polystyrene colloidal templates and resulting inorganic hollow spheres*. CHem. Mater. 13, 400-409(2001).

59. Caruso, F., *Hollow inorganic capsules via colloid-templated layer-by-layer electrostatic assembly*. Top Curr Chem 227, 145-468(2003).

60. Buxbaum, G., *Industrial Inorganic Pigments*. VCH: Weinheim, 1993.

61. Kwoka, R. A., Titanium Dioxide. In *Pigments for Paper*, Hagemeyer, R. W., Ed. TAPPI Press: Atlanta, 1997.

62. Solomon, D. H.; Hawthorne, D. G., *Chemistry of Pigments and Fillers*. Wiley-Interscience: New York, 1983.

63. Johnson, R. W. In *Rating Performance of TiO2 Pigments in Coated Paper Applications*, 2005 TAPPI Coating Conference and Exhibit Roundtable, Toronto, ON, Canada, 2005; Toronto, ON, Canada, 2005.

64. Bohren, C. F.; Huffman, D. R., *Absorption and Scattering of Light by Small Particles*. Wiley-VCH: Weinheim, 2004.

65. Thiele, E. S. Scattering of Electromagnetic Radiation by Complex Microstructures in the Resonant Regime. University of Pennsylvania, 1998.

66. Balfour, J. G., *Opacity and titanium dioxide pigments*. Journal of the Oil and Colour Chemistry Association 6, 225-230,245(1990).

67. Logan, T. W. In *Using Titanium Dioxide as a Filler Pigment*, Dyes, Fillers & Pigments Short Course, Chicago, IL, 1995; TAPPI Press: Chicago, IL, 1995.

68. Cutrone, L., *Influence of fine-particle size extenders on the optical properties of latex paints*. Journal of Coatings Technology 58, (736), 83-88(1986).

69. Bruehlman, R. J.; Thomas, L. W.; Gonick, E., *Effect of Particle Size and Pigment Volume Concentration on Hiding Power of Titanium Dioxide*. Official Digest February, 252-267(1961).

70. Ross, W. D., *Theoretical Light-Scattering Power of TiO2 Microvoids*. Ind. Eng., Prod. Res. Develop. 13, (1), 45-49(1974).

71. Ross, W. D., *Theoretical Computation of Light Scattering Power: Comparison between TiO2 and Air Bubbles*. Journal of Paint Technology 43, (563), 50-66(1971).

72. Ribarsky, M. W., *Handbook of Optical Constants*. Academic Press: New York, 1985.

73. Palmer, B. R.; Stamatakis, P.; Bohren, C. F.; Salzman, G. C., *A Multiple-Scattering Model for Opacifying Particles in Polymer Films*. Journal of Coatings Technology 61, (779), 41-47(1989).

74. Fields, D. P.; Buchacek, R. J.; Dickinson, J. G., *Maximum TiO2 hiding power- the challenge*. (1993).

75. Fitzwater, S.; III, J. W. H., *Dependent Scattering Theory: A New Approach to Predicting Scattering in Paints*. Journal of Coatings Technology 57, (721), 39-47(1985).

76. Biermann, C. J., *Handbook of Pulping and Papermaking*. 2nd ed.; Academic Press: San Diego, 1996.

77. Leskela, M. Simulation of Particle Packing for Modelling the Light Scattering Characteristics of Paper. Helsinki University of Technology, Espoo, 1997.

78. Mishchenko, M. I.; Videen, G.; Babenko, V. A.; Khlebtsov, N. G.; Wriedt, T., *T-matrix theory of electromagnetic scattering by particles and its applications: a comprehensive reference database*. Journal of Quantitative Spectroscopy & Radiative Transfer 88, 357-406(2004).

79. Mishchenko, M. I., *Maxwell's equations, radiative transfer, and coherent backscattering: a general perspective*. Journal of Quantitative Spectroscopy & Radiative Transfer 101, 540-555(2006).

80. Thiele, E. S.; French, R. H., *Computation of Light Scattering by Anisotropic Spheres of Rutile Titania*. Advanced Materials 10, (15), 1271-1276(1998).

81. Mackowski, D. W.; Mishchenko, M. I., *Calculation of the T matrix and the scattering matrix for ensembles of spheres*. J. Opt. Soc. Am. A 13, (11), 2266-2278(1996).

82. Balfour, J. G., Titanium Dioxide Pigments. In *Technological Applications of Dispersions*, McKay, R. B., Ed. Marcel Dekker: 1994; Vol. 52.

83. Fields, D. P.; Buchacek, R. J.; Dickinson, J. G., *Maximum TiO2 hiding power- the challenge*. JOCCA 2, 87-93(1993).

84. Liu, L.; Mishchenko, M. I., *Effects of aggregation on scattering and radiative properties of soot aerosols*. Journal of Geophysical Research 110, 1-10(2005).

85. Quinten, M., *Optical Effects Associated with Aggregates of Clusters*. Journal of Cluster Science 10, (2), 319-357(1999).

86. McNeil, L. E.; Hanuska, A. R.; French, R. H., *Orientation dependence in near-field scattering from TiO2 particles*. Applied Optics 40, (22), 3726-3736(2001).

87. Auger, J.; Barrera, R. G.; Stout, B., *Scattering efficiency of clusters composed by aggregated spheres*. Journal of Quantitative Spectroscopy & Radiative Transfer 79-80, 521-531(2003).

88. Auger, J.; Stout, B.; Martinez, V., *Scattering efficiency of aggregated clusters of spheres: dependence on configuration and composition*. J. Opt. Soc. Am. A 22, (12), 2700-2708(2005).

89. Usami, A., *Rigorous solutions of light scattering of neighboring TiO2 particles in nanocrystalline films*. Solar Energy Materials & Solar Cells 59, 163-166(1999).

90. Atherton, W. C.; Manasso, J. A.; Sennett, P., Structured Pigments. In *Pigments for Paper*, Hagemeyer, R. W., Ed. Tappi Press: Atlanta, 1997.

91. Hemenway, C. P.; Latimer, J. J.; Young, J. E., *Hollow-sphere polymer pigment in paper coating*. Tappi Journal 68, (5), 102-105(1985).

92. Brown, J. T. In *The Relationship Between Hollow Sphere Pigment Geometry and Optical Performance of Finished Paper Coatings*, Coating Conference, Montreal, Quebec, 1991; TAPPI Press: Montreal, Quebec, 1991.

93. Brown, J. T.; Kotoye, F. O., Synthetic Plastic Pigments. In *Pigments for Paper*, Hagemeyer, R. W., Ed. Tappi Press: Atlanta, 1997.

94. Hsu, W. P.; Yu, R.; Matijevic, E., *Paper Whiteners I. Titania Coated Silica*. J. Colloid Interface Sci. 156, 56-65(1993).

95. Johnson, R. W.; Thiele, E. S.; French, R. H., *Light-scattering efficiency of white pigments: an analysis of model core-shell pigments vs. optimized rutile TiO_2*. Tappi Journal 80, (11), 233-239(1997).

96. Neimo, L. In *Internal sizing of priniting paper*, PAPEX-85 International Conference and Exhibition Leatherhead, England, 1985; PIRA: Leatherhead, England, 1985.

97. Page, D. H., *A theory for the tensile strength of paper*. Tappi 52, (4), 674-681(1969).

98. Linder, A.; Bergman, R.; Bodin, A.; Gatenholm, P., *Mechanism of assembly of xlan onto cellulose surfaces*. Langmuir 19, 5072-5077(2003).

99. Xu, Y.; Pelton, R., *A new look at how fines influence the strength of filled papers*. Journal of Pulp and Paper Science 31, (3), 147-152(2005).

100. Aho, O.; Silenius, P.; Pitkanen, M.; Hietanen, S. Filler and a process for the production thereof. 2444011, 2002.

101. Kuboshima, K., High Perform. Paper Soc. (Jpn) 21, 31(1982).

102. Gill, R. A. 2,037,525, 1995.

103. Drummond, D. K.; Wernett, P. WO 00/59965, 2000.

104. Yoon, S.; Deng, Y., *Caly-starch composites and their application in papermaking*. Journal of Applied Polymer Science 100, 1032-1038(2006).

105. Yoon, S.; Deng, Y., *Starch-fatty complex modified filler for papermaking*. TAPPI JOURNAL 5, (9), 1-7(2006).

106. Klemm, D.; Heublein, B.; Fink, H.-P.; Bohn, A., *Cellulose: Fascinating Biopolymer and Sustainable Raw Material*. Angewandte Chemie 44, 3358-3393(2005).

107. Zhao, H.; Kwak, J. H.; Wang, Y.; Franz, J. A.; White, J. M.; Holladay, J. E., *Interactions Between Cellulose and N-methylmorpholine-N-oxide*. Carbohydrate Polymers 67, 97-103(2007).

108. Rosenau, T.; Hofinger, A.; Potthast, A.; Kosma, P., *On the conformation of the cellulose solvent N-methylmorpholine-N-oxide (NMMO) in solution*. Polymer 44, 6153-6158(2003).

109. Roder, T.; Morgenstern, B., *The Influence of Activation on the Solution State of Cellulose Dissolved in N-methylmorpholine-N-oxide-monohydrate*. Polymer Communication 40, 4143-4147(1999).

110. Schultz, L.; Burchard, W.; Donges, R., *Cellulose Derivatives, Modifications, Characterization, and Nanostructures*. 1998; Vol. 688.

111. Schulz, L.; Seger, B.; Burchard, W., *Structures of Cellulose in Solution*. Macromolecular Chemistry and Physics 201, 2008-2022(2001).

112. Fink, H. P.; Weigel, P.; Purz, H. J.; Ganster, J., *Structure Formation of Regenerated Cellulose Materials from NMMO-Solutions*. Progress in Polymer Science 26, 1473-1524(2001).

113. Giesche, H., *Synthesis of monodispersed silica powders II. Controlled growth reaction and continuous production process*. J. Eur. Cer. Soc. 14, (3), 205-214(1994).

114. Barder, T. J.; DuBois, P. D. Process for forming highly uniform silica spheres. US Patent No. 4,983,369, 1991.

115. Hanprasopwattana, A.; Srinivasan, S.; Sault, A. G.; Datye, A. K., *Titania coatings on monodisperse silica spheres (characterization using 2-propanol dehydration and TEM)*. Langmuir 12, 3173-3179(1996).

116. Liu, R.; Dong, P.; Chen, S.-L., *Monodisperse SiO2/TiO2 core-shell colloidal spheres: synthesis and ordered self-assembling*. Chemistry Letters 34, (4), 548-549(2005).

117. Pecharsky, V. K.; Zavalij, P. Y., *Fundamentals of Powder Diffraction and Structural Characterization of Materials*. Kluwer Academic Publishers: Boston, 2003.

118. Liu, X.; Qiu, G.; Li, X., *Shape-controlled synthesis and properties of uniform spinel cobalt oxide nanocubes*. Nanotechnology 16, 3035-3040(2005).

119. Lieber, C. M., *One-dimensional nanostructures: chemistry, physics, and applications*. Solid State Commun. 107, (11), 607-616(1998).

120. Lu, Y.; Yin, Y.; Xia, Y., *Three-dimensional photonic crystals with non-spherical colloids as building blocks*. Adv. Mater. 13, (6), 415-420(2001).

121. Hoffman, M. R.; Martin, S. T.; Choi, W.; Bahnemann, D. W., *Environmental applications of semiconductor photocatalysis*. Chemical Reviews 95, 69-96(1995).

122. Heller, A., *Chemistry and applications of photocatalytic oxidation of thin organic films*. Acc. Chem. Res. 28, 503-508(1995).

123. Legrini, O.; Oliveros, E.; Braun, A. M., *Photochemical processes for water treatment*. Chemical Reviews 93, 671-698(1993).

124. Zhang, D.; Qi, L., *Synthesis of mesoporous titania networks consisting of anatase nanowires by templating of bacterial cellulose membranes*. Chemical Communications, 2735-2737(2005).

125. Liu, L.; Dong, P.; Liu, R.; Zhou, Q.; Wang, X.; Yi, G.; Cheng, B., *Preparation and self-assembly of uniform TiO2/SiO2 composite submicrospheres*. J. Colloid Interface Sci. 288, 1-5(2005).

126. Jun, Y.-w.; Casula, M. F.; Sim, J.-H.; Kim, S. Y.; Cheon, J.; Alivisatos, A. P., *Surfactant-assisted elimination of a high energy facet as a means of controlling the shapes of TiO2 nanocrystals*. J. Am. Chem. Soc. 125, 15981-15985(2003).

127. Kanie, K.; Sugimoto, T., *Shape control of anatase TiO2 nanoparticles by amino acids in a gel-sol system*. Chem. Commun., 1584-1585(2004).

128. Lu, Y.; Yin, Y.; Xia, Y., *Preparation and characterization of micrometer-sized "egg shells"*. Adv. Mater. 13, (4), 271-274(2001).

129. Caruso, R. A., *Nanocasting and nanocoating*. Top Curr Chem 226, 91-118(2003).

130. Caruso, F., *Hollow inorganic capsules via colloid-templated layer-by-layer electrostatic assembly*. Top Curr Chem 227, 145-168(2003).

131. Shiho, H.; Kawahashi, N., *Titanium compounds as coatings on polystyrene latices and as hollow spheres*. Colloid Polym. Sci. 278, 270-274(2000).

132. Edgar, C.; Gray, D., Macromolecules 35, 7400(2002).

133. Wise, D. L.; Klibanov, A. M.; Langer, R.; Mikos, A. G.; Peppas, N. A.; Trntolo, D. J.; Wnek, G. E.; Yaszemski, M. J., *Handbook of Pharmaceutical Controlled Release Technology*. Marcel Dekker: New York, 2000.

134. Mundargi, R.; Srirangarajan, S.; Agnihotri, S. A.; Patil, S.; Ravindra, S.; Setty, B.; Aminabhavi, T., *Development and evaluation of novel biodegrdaable microspheres based on poly(D,L-lactide-co-glycolide) and poly(E-caprolacetone) for controlled delivery of doxyxycline in the treatment of human periodontal pocket: In vitro and in vivo studies*. J. Controlled Release 119, (1), 59-68(2007).

135. Mundargi, R.; Srirangarajan, S.; Agnihotri, S. A.; Patil, S.; Ravindra, S.; Setty, S.; Aminabhav, T., Drug Delivery Reviews 55, (3), 329(2003).

136. Pyun, J., *Nanocomposite materials from functional polymers and magnetic colloids*. Polym. Reviews 47, (2), 231-263(2007).

137. Johnston, A.; Cortes, C.; Angelators, A.; Caruso, F., *Layer-by-layer engineered capsules and their applications*. Current Opinion in Colloid INterf. Sci. 11, (4), 203-209(2006).

138. De, S.; Pritchett, M.; Mazumder, M.; Yurteri, C.; Egorov, O., *Electrostatic microencapsulation technique for producing composite particles* Particulate Sci. Technol. 20, (3), 169-185(2002).

139. Guzry, D.; McClements, J., Adv. Colloid Interf. Sci. 128-130, 227(2006).

140. Luff, J., Food Sci. Technol. 21, (1), 30(2007).

141. Challener, C., Polym. Paint Colour J. 195, (4495), 14(2005).

142. Ryu, J.; Lee, E.; Lim, Y.; Lee, M., *Carbohydrate-coated supramolecular structures: Transformation of nanofibers into spherical micelles triggered by guest encapsulation*. J. Am. Chem. Soc. 129, (15), 4808-4814(2007).

143. Ding, L.; Hao, C.; Xue, Y.; Ju, H., *A bio-inspired support of gold nanoparticles-chitosan nanocomposites gel for immobilization and electrochemical study of K562 leukemia cells*. Biomacromolecules 8, (4), 13411346(2007).

144. Feili, D.; Schuettler, M.; Doerge, T.; Kammer, S.; Stieglitz, T., *Encapsulation of organic field effect transistors for flexible biomedical microimplants*. Sensors Actuators, A: Phys. 120, (1), 101-109(2005).

145. Tong, Z.; Deng, Y., *Synthesis of water-based polystyrene-nanoclay composite suspension via miniemulsion polymerization*. Ind. Eng. Chem. Res. 45, (8), 2641-2645(2006).

146. Sun, Q.; Deng, Y.; Wang, Z., *Synthesis and characterization of polystyrene-encapsulated laponite composites via miniemulsion polymerization*. Macrom. Mater. Eng. 289, 288-295(2004).

147. Nelson, K. L.; Deng, Y., *The shape dependence of core-shell and hollow titania nanoparticles on coating thickness during layer-by-layer and sol-gel synthesis*. Nanotechnology 17, (13), 3219-3225(2006).

148. Sun, Q.; Deng, Y., *Encapsulation of polystyrene latex with temperature-responsive poly(N-isopropylacrylamide) via a self-assembling approach and the adsorption behaviors therein*. Langmuir 21, 5812-5816(2005).

149. Soppimath, K.; Liu, L.; Seow, W.; Lin, S.; Powell, R.; Chan, P.; Yang, Y., *Multifunctional core/shell nanoparticles self-assembled from pH-induced thermosensitive polymers for targeted intracellular anticancer drug delivery*. And. Funct. Mater. 17, (3), 355-362(2007).

150. Rao, M. S.; Dave, B., *Use of environmentally-responsive smart glasses in controlled release: Diffusion of molecules under applied stimuli*. J. Sol-Gel Sci. Tech. 40, (2), 241-251(2006).

151. Zhang, J.; Huang, S.; Zhuo, R., *A novel sol-gel strategy to prepare temperature-sensitive hydrogel for encapsulation of protein*. Colloid Polym Sci 284, (2), 209-213(2005).

152. Fink, H. P.; Weigl, P.; Purz, H. J.; Ganster, J., *Structure formation of regenerated cellulose materials from NMMO-solutions*. Prog. Polym. Sci. 26, 1473-1524(2001).
153. Woodings, C. R., *The development of advanced cellulosic fibers*. International Journal of Biological Macromolecules 17, (6), 305-309(1995).

154. Laity, P. R.; Glover, P. M.; Hay, J. N., *Composition and phase changes observed by magnetic resonance imaging during non-solvent induced coagulation of cellulose*. Polymer 43, 5827-5837(2002).

155. Bang, Y. H.; Lee, S.; Park, J. B.; Cho, H. H., *Effect of Coagulation Conditions on Fine Structure of Regenerated Cellulosic Films Made from Cellulose/N-Methylmorpholine-N-Oxide/H2O Systems*. Journal of Applied Polymer Science 73, 2681-2690(1999).

156. Ducos, F.; Biganski, O.; Schuster, K. C.; Navard, P., *Influence of the Lyocell Fibers Structure on their Fibrillation*. Cellulose Chemistry and Technology 40, (5), 299-311(2006).

157. Schuster, K. C.; Aldred, P.; Villa, M.; Baron, M.; Loidl, R.; Biganski, O.; Patlazhan, S.; Navard, P.; Ruf, H.; Jericha, E., *Characterising the Emerging Lyocell Fibers Structures by Ultra Small Angle Neutron Scattering (USANS)*. Lenzinger Berichte 82, 107-117(2003).

158. Schulz, L.; Burchard, W.; Donges, R., *Cellulose Derivatives, Modifications, Characterization, and Nanostructures*. 1998; Vol. 688.

159. Nelson, K.; Deng, Y., *The shape dependence of core-shell and hollow titania nanoparticles on coating thickness during layer-by-layer and sol-gel synthesis*. Nanotechnology 17, (13), 3219-3225(2006).

160. Yoon, S.; Deng, Y., *Experimental and modeling study of the strength properties of clay-starch composite filled papers*. Industrial and Engineering Chemistry Research, (2007).

161. Nelson, K. L.; Deng, Y., *Submitted to* Biomacromolecules, (2007).

162. Pu, Y.; Zhang, J.; Elder, T.; Deng, Y.; Gatenholm, P.; Ragauskas, A. J., *Investigation into Nanocellulosics versus Acacia Reinforced Acrylic Films*. Composites Part B: Engineering 38, (3), 360-366(2006).

163. Favier, V.; Canova, G. R.; Cavaille, J. Y.; Chanzy, H.; Dufreshne, A.; Gauthier, C., Polym. Adv. Technol. 6, (5), 351-355(1995).

164. Xu, Y.; Chen, X.; Pelton, R., *On how polymers strengthen filled papers*. Tappi 4, 8-12(2005).

165. Woolley, J. T., Plant Physiol. 55, 172(1975).

VITA

Kimberly Nelson was born in Mobile, AL and grew up in the Charleston, SC area where she attended Ashley Hall. She obtained her undergraduate degree in Mathematics and Chemistry in 1999 from Agnes School College in Decatur, Georgia. She then received her master's degree in 2001 in Pulp and Paper Science and Engineering from the Institute of Paper Science and Technology located in Atlanta, Georgia. Following two years as a Process Engineer in the Pulp Mill at MeadWestvaco's North Charleston facility, Kim returned to school to obtain her PhD in Chemical and Biomolecular Engineering at Georgia Institute of Technology. Upon completion of her degree in August 2007, Kim joined Trinity Consultants in Atlanta, Georgia as an industrial Environmental Consultant. Kim recently purchased a home in the Kirkwood neighborhood of Atlanta and enjoys painting, literature, art history, meditation, furniture restoration, and investing.